

THE ASTROPHYSICAL JOURNAL SUPPLEMENT SERIES, 33: 515-562, 1977 April
 © 1977. The American Astronomical Society. All rights reserved. Printed in U.S.A.

RADIATION DYNAMICS, ENVELOPE EJECTION, AND SUPERNOVA LIGHT CURVES*

SYDNEY W. FALK

W. K. Kellogg Radiation Laboratory, California Institute of Technology

AND

W. DAVID ARNETT

Department of Astronomy, University of Illinois, Urbana

Received 1976 May 26

ABSTRACT

Supernova light curves are interpreted within a shock wave model for envelope ejection. The hydrodynamical and radiative transport physics and the calculational method are summarized. The light curves are examined for numerical models (presented in tables) for two classes of presupernova configuration. The effects of outer-envelope and highly extended ($R_0 \approx 10^{15}$ cm) presupernova structures on the luminosity peak epoch are emphasized. Implications for explosion energetics, presupernova mass loss, Rayleigh-Taylor instabilities in the ejecta, and exposure of underlying regions are discussed.

Subject headings: hydrodynamics — shock waves — stars: supernovae

I. INTRODUCTION

The identification of the Crab Nebula with the supernova that occurred during 1054 in the constellation Taurus implies that at least some supernovae result from the explosion of a star. Analysis of the motions of the nebula (Woltjer 1972; Trimble 1968) support this view. The discovery of PSR 0532 near the projected origin of the nebular expansion shows that a neutron star was formed in the process.

This paper represents a step toward answering the following questions: What would an exploding star look like? How does the exploding star evolve to become an observed supernova remnant? How are the light curve and gross spectral characteristics produced? In this analysis emphasis is placed on delineating the underlying physical processes by working forward from first principles rather than backward from observations. Consequently, we do not attempt detailed fits to particular observational data by parameter variation at the present time (see, however, Arnett and Falk 1976). As our understanding of the underlying phenomena progresses, more efficient computational procedures can be developed for such a study.

In this paper we do not consider the effects of (1) heating by radioactive nuclei, (2) energy input by a pulsar, or (3) optical reverberation. Any or all of these processes could be important, but we wish to discover which features of the supernova can be explained without them, and which may require these or some other additional complications.

Galactic supernova remnants are closely concen-

trated in the plane and are extreme Population I objects, as are pulsars. In spiral galaxies, observed supernovae tend to occur near spiral arms and H II associations—that is, near regions rich in young, massive stars. For these and various theoretical reasons, the progenitors of at least many supernovae are thought to be massive stars.

Massive stars may suffer considerable mass loss prior to the supernova explosion. Supergiants are observed to have high rates of mass loss. Many theoretical reasons have been proposed for supergiants undergoing extensive mass loss. The resulting circumstellar matter can have a profound influence on the nature and evolution of the visual aspects of the explosive event.

Construction of a quantitative theoretical model of the explosion of a massive star, possibly surrounded by circumstellar matter, requires the use of numerical hydrodynamic techniques coupled with radiative transfer. Three stages may occur. At least initially, the material in the star will be optically thick, and the usual equilibrium radiative diffusion approximation is appropriate. In the circumstellar material, and as stellar expansion occurs, the radiation and matter decouple and optical depths become small, requiring a (transfer) transport approach to the radiative processes. Because velocities as high as $v \approx 10^4$ km s⁻¹ are inferred from some supernova spectra, it is desirable to properly include time dependence and special relativistic effects in the radiative transfer. Finally, much of the material becomes transparent to continuum radiation, and a “nebular” stage occurs in which emission-line radiation becomes important. We have devised computational techniques which allow a reasonably accurate and efficient treatment of the first two stages. These calculations provide a physically

* Supported in part by the National Science Foundation [GP-32051, University of Texas], [PHY76-02724, AST 75-01398 A01, California Institute of Technology], and [MPS 74-20755, University of Illinois].

self-consistent framework within which the third ("nebular") stage may be attacked, and justify some of the theoretical simplifications used in earlier work.

Grasberg, Imshennik, and Nadyozhin (1971) review and summarize their extensive work on this problem. They examined the effect of a shock wave on a stellar envelope by numerical solution of the coupled equations for hydrodynamics and (equilibrium) radiative diffusion; this picture gave, in a natural way, P Cygni line profiles, gradual reddening, and a slow decrease in line velocity with increasing transparency. They found that a diffusion wave ("heat tongue") developed for extremely extended and diffuse structures. The importance of the recombination wave in governing the effective temperature was emphasized. Upon comparison with the scarce observational data, they concluded that a very extensive atmosphere ($\sim 10^4 R_\odot$) was required in at least some cases. While the qualitative agreement was good, the quantitative agreement on the evolution of some important properties was not (see their Fig. 14, for example).

Colgate and White (1966) made the important point that compact models were not effective sources of radiation; adiabatic cooling converted internal energy into kinetic energy. Colgate and McKee (1969) did some hydrodynamic calculations of compact models, using Truran's suggestion that the decay of ^{56}Ni might be the needed energy source.

A weakness in the work of Grasberg, Imshennik, and Nadyozhin was their initial envelope structure; their extended models were not in thermal or hydrostatic equilibrium. In order to see how initial structure might affect observables, Falk and Arnett (1973, hereafter FA); used a fairly accurate representation of a Paczyński envelope, both bare and surrounded by a circumstellar shell. The latter was not in hydrostatic equilibrium and was therefore assumed to be in some sort of dynamic state. A pronounced thermal instability occurred in the circumstellar shell, giving rise to two density phases and the possibility of Rayleigh-Taylor instability. The results were consistent with those of Grasberg, Imshennik, and Nadyozhin (1971) and, using the same scanty data, it was again concluded that circumstellar shells were indicated. Such comparison with observation is not trivial. Within the framework of the equilibrium radiative diffusion approximation, details of atmospheric structure are lost. In particular, just those regions which determine line profiles are treated crudely. On the other hand, the observational data can be strongly influenced by line effects. Another problem is that the data usually refer to a limited wavelength range. Thus to go from actual reduced data to the inferred quantities (effective temperature, fluid velocity, bolometric luminosity, etc.) needed to test the theory requires some theoretical modeling also. The situation improved when Kirshner and Kwan (1974) published empirical transformations for SN 1969I (Type II) by which the *UBV* photometry of Ciatti, Rosino, and Bertola (1971) could be converted to effective temperature. Arnett and Falk (1976) compared this newly derived information with the earlier calculations (FA); predictions of the "bare"

envelope case were in detailed quantitative agreement with the changing effective temperature over the entire time it was well defined. The behavior of the photospheric radius and of the fluid velocity of matter at the photosphere was reasonably well reproduced. The agreement is striking when one realizes that no parameters were adjusted to obtain the fit, and suggests that this picture is the correct one for at least the best observed supernova of Type II.

Lasher (1975) has extended this approach to the production of the luminosity "peak" in Type I supernovae (the tail presumably is due to a different process). His models are very similar to some of those of Grasberg, Imshennik, and Nadyozhin (1971) or to the "bare" model of Falk and Arnett (1973), except that (1) the mass is smaller and (2) the helium abundance is high. He also pointed out that Doppler shifts due to differential velocity could significantly enhance the bound-bound opacity; this would be important at lower temperature (see Karp *et al.* 1976).

Recently (while this paper was in draft form) Chevalier (1976) gave a nice discussion of models similar to the "bare" envelope model of FA. He considered slightly smaller mass. He analyzed his numerical results in terms of the similarity solution for a blast wave with $\gamma = 4/3$ (radiation dominated gas), and discussed some effects of different structures. He found a new effect having to do with the hydrodynamics of the core; upon including very dense central zones (presumably matter just outside the collapsing core?), he found that a reflected shock slowed their expansion, keeping them hot and the luminosity larger at late times. He discussed in detail the agreement of his calculations with observations (especially 1969I referred to above), but unfortunately did not actually plot a comparison or give enough detail for the reader to do so accurately. It seems likely that the result would be similar to that of Arnett and Falk (1976).

All of the calculations discussed above made use of the equilibrium diffusion approximation to radiative transfer. We have constructed a more general scheme which allows the matter and radiation to decouple, but still reproduces this limiting case. In this paper we analyze, in the context of supernovae, some of the appropriate hydrodynamic and radiative transfer physics and summarize our calculational methods (see also Imshennik and Morozov 1969). We apply the nonequilibrium techniques to an extended configuration (model C) to explore the effects. We review our previous bare model (model A), which has proved successful in reproducing the features of SN 1969I, and explore the sensitivity of the early (peak) behavior to outer envelope structure (models D, E, and F). In all these cases the calculated results are tabulated in detail to allow quantitative comparison with observationally derived data.

We do not attempt to explicitly include line contributions to the treatment of (the continuum) radiative transfer. It is not our intention, and it is well beyond the scope of this paper, to examine the detailed spectral character of the models we present. We seek primarily an explanation for the character of Type II

supernovae, but we wish to emphasize that many or all of the physical processes discussed here will apply equally well to Type I objects. For this reason, we present the calculations in as general a sense as possible, with as little emphasis on the distinctness of the two classes as is warranted.

- The remainder of the paper is organized as follows:
- II. Stages of the Supernova Event: Definition of Terms, Overview of Explosion Scenario
 - III. Physics and Formulation of the Calculational Method
 - a) Fluid Equations with Radiation Diffusion
 - b) Time-Dependent Radiative Transport
 - c) Calculational Method
 - IV. Application to Supernova Light Curves
 - a) General Features
 - b) Compact Model (Model A): Behavior of the Photosphere; Effective Temperatures; Diffusive Energy Release; Expansion and Photospheric Recession; Material Postshock Conditions; Final Luminosity Turndown
 - c) Extended Models: Model B; Models D, E, and F
 - d) Details of the Light Peak (Model C): Shock Propagation; Fluid Instabilities; Light Peak; Material Kinetics
 - e) Discussion: Shell Parameters and Mass Loss; Energetics; Character of the Light Curves; Velocities; Turbulent Velocities; Photospheric Recession; Exposure of Mantle and Core
 - f) Summary and Conclusions
 - Appendix A. Difference Equations
 - Appendix B. Centering Considerations, Time Steps, and Accuracy
 - Appendix C. Computational Treatment of Density Inversions
 - Appendix D. Color Magnitudes

II. STAGES OF THE SUPERNOVA EVENT

The evolution of a supernova before explosion is just the evolution of the presupernova star; the precise nature of this presupernova evolution is important because it sets the stage and provides the mechanism for the explosion. A general trend in advanced stages of stellar evolution (at least for single stars) is the formation of a red-giant structure. As mentioned above, there may be a fairly extensive circumstellar shell (this material would not in general be in hydrostatic equilibrium). Figure 1 is a sketch illustrating some (possible) qualitative features of a presupernova star. For conciseness in subsequent discussion in this paper we define the following terms:

1. *Shell*.—The circumstellar shell, previously ejected from the star by mass loss, containing perhaps $0.01 M_{\odot}$ or so within a radius $r \approx 10^{15}$ cm. Probably not in hydrostatic equilibrium.

2. *Envelope*.—The outer parts of the star, extending into the helium-burning shell. Probably quite extended (out to $r \approx 10^{13}$ cm or so) and at least close to hydrostatic equilibrium prior to the explosion. Rich in

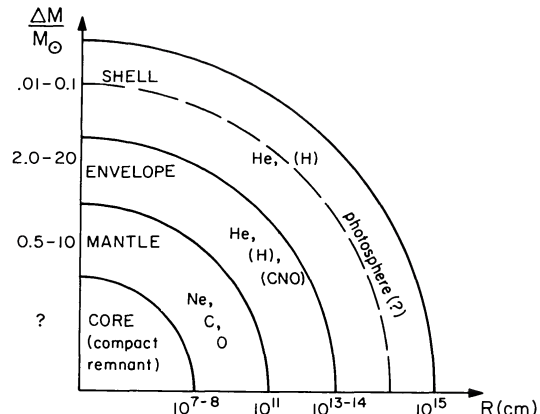


FIG. 1.—Schematic presupernova structure. Follows the description in § II of the text. Estimates for the outer radii R of each region and the probable mass increment involved, $\Delta M/M_{\odot}$, are shown on the horizontal and vertical axes, respectively. The values quoted are approximate, and are intended only to suggest relative scales. The “shell” region may or may not exist for a given supernova. Dominant chemical compositions are indicated. In the outer two layers, envelope and shell, hydrogen may or may not be present, depending especially upon the SN type. The envelope (and possibly the shell) may also have CNO cycle elements represented in significant quantities. The mantle region will be largely made up of products from later burning stages, including predominantly Ne, C, O, and perhaps others as well.

helium and, if mass loss has not been too extensive, hydrogen.

3. *Mantle*.—Material interior to the helium-burning shell which will be ejected from the star by the explosion. Composition is that of “metals,” i.e., $Z > 2$; might extend out to $r \approx 10^{11}$ cm or so. Mass probably ranges from $M/M_{\odot} \approx 0.05$ to 10 (rarely). This is the nucleosynthesis material; to get the observed heavy element yield we need only $\sim 0.7 M_{\odot}$ per supernova *on the average*.

4. *Core*.—The innermost parts of the star which collapse to form a neutron star (if such is produced). At the time of explosion this region probably extends to $r \approx 10^7$ to 10^8 cm and may contain $M/M_{\odot} \approx 0$ to 2.4. If the mass is much larger, then a black hole will result (and perhaps no explosion!).

The precise nature of these regions must depend on the model chosen for the event. In some theories some of these regions may not be present.

a) Explosive Release of Energy

In this context “explosive” means that the energy that powers the supernova ($E \approx 10^{50}$ to 10^{51} ergs) is communicated to the stellar material on a time scale short compared with the dynamical time of the presupernova object. A measure of the dynamical time is the time required for a sound wave to travel from the core to the “surface.” The “surface” can be taken as the depth to which an external observer could see (optical depth $\tau \approx 1$) and might lie at the outer edge of the envelope ($r \approx 10^{13}$ cm) or in the shell (up to $r \approx 10^{15}$ cm). For a cautious estimate we note that in

the envelope $T \gtrsim 5 \times 10^3$ K, so $v(\text{sound}) \approx (\mathcal{R}T)^{1/2} \approx 6 \times 10^5$ cm s $^{-1}$, and therefore

$$t(\text{dynamical}) \approx 1.6 \times 10^7 \text{ s},$$

which is about six months.

Almost all theories advanced so far place the explosion in the core and/or the mantle.

b) Shock Propagation through the Envelope

For "explosive" release of energy, the expansion is supersonic in the envelope. Insofar as electromagnetic radiation is concerned, the external observer will not know the explosion has occurred in the interior until the resulting shock wave reaches the "surface" ($\tau \approx 1$). Neutrino-antineutrino radiation may diffuse out faster, as might gravitational radiation. For a shock velocity of 5×10^3 km s $^{-1}$ it would take a time to traverse the envelope ($r \approx 10^{13}$ cm)

$$t(\text{shock}) \approx 6 \text{ hr.}$$

c) Emergence of the Shock at the Envelope-Shell Interface

There will be a sharp decrease in density in passing from the envelope to the shell. This will affect the nature of the shock propagation and the relative importance of gas compression and radiative stress in accelerating the matter. If the shell is optically thick, this stage will not be directly visible.

d) Acceleration of the Shell

Because of the low density of material in the shell, photon mean-free paths are much larger than in the envelope. The photon diffusion speed, $v \approx \lambda c/3r$, can exceed the postshock sound speed, and a photon-propagated shock can develop. The high luminosity can directly transfer momentum to the low-mass shell, accelerating it to large velocities. Even if the shell is neglected, the steep density gradient in the outer part of the envelope causes that material to behave in this manner.

e) Emergence of the Shock at the Photosphere

The first electromagnetic display of the supernova will coincide with the emergence of the shock at the photosphere. If there is no shell, this stage is to be identified with stage (c) above. Although the shock transports energy and momentum to the photosphere, it is by no means obvious that mantle material will become visible so quickly. At this stage one probably observes only shell (or envelope) material.

If the shell is important, this stage can correspond to maximum light. If the shell is negligible, this stage may contribute a brief high-luminosity precursor of radiation which is harder than visual.

f) Expansion and Transparency of the Shell

As the shocked matter expands and attenuates, the photon mean-free path increases. Although the radial

coordinate for a given bit of *matter* increases, the position of the photosphere depends also on the changing opacity. For a while the radius of the photosphere could increase, but eventually an external observer will see deeper and deeper into the material.

If the shell is important this stage will correspond to immediate postmaximum light. Observational inferences from this stage will refer to the properties of the *shell*, not the envelope. Mass estimates and compositional inferences based on this stage can be grossly misleading if assumed to apply to the envelope and mantle as well.

g) Expansion and Transparency of the Envelope

When the shell is transparent, the envelope is uncovered. The envelope can contain considerable mass and may suffer considerable adiabatic cooling prior to this stage. If the mantle-envelope interface is Rayleigh-Taylor unstable, blobs of matter enriched in elements beyond helium may become visible.

If the shell is unimportant, this stage could correspond to near-maximum light.

h) Expansion and Transparency of the Mantle

When the envelope is transparent, the mantle is revealed. The products of nucleosynthesis will become visible. For most supernovae the results will not be as spectacular as many have assumed, since the *average* supernova should make about $0.7 M_{\odot}$ of ^{12}C and ^{16}O and $0.1 M_{\odot}$ of iron-group nuclei. A much higher average yield is inconsistent with observed Population I abundances. If the mantle velocities are not large, this stage may be slow in developing.

i) Uncovering of the Core

When the mantle becomes transparent, any compact remnant formed by the core will become visible. It is not clear whether any supernova has been followed long enough for such a stage to be observed. Needless to say, such observations would be of considerable interest to theoreticians.

After this last stage (i) the evolution merges with that of supernova remnants (see Woltjer 1972). Further discussion of these stages is given in § IV, and reasons for this set of choices will become more apparent.

III. PHYSICS AND FORMULATION OF THE CALCULATIONAL METHOD

a) Fluid Equations with Radiative Diffusion

A natural coordinate frame for radiation transport calculations is the rest frame of the emitting or absorbing fluid, in part because of the simple form of the mass absorption coefficients in this frame. In the case of an inertial system, this frame is trivially related to the center-of-mass frame by a Galilean transformation, but in a dynamic situation these frames cannot in general be made coincident at all times by such a transformation. One then resorts for computational ease to a system of Lagrangian mass coordinates.

The equation of continuity for the fluid guarantees mass conservation, and the mass variable $m(r, t)$ in the case of spherical symmetry is defined to be

$$m(r', t) = \int_0^{r'} 4\pi r^2 \rho(r, t) dr, \quad (1)$$

where $\rho(r, t)$ is the mass density at radius r at time t . The equation of fluid momentum conservation is written in Lagrangian form as

$$\frac{dv}{dt} = -4\pi r^2 \frac{\partial P}{\partial m} - \frac{Gm}{r^2}, \quad (2)$$

where v is the bulk flow velocity of the matter and P is the total (isotropic) pressure.

The second-order moment equation, obtained by multiplying equation (2) by v , may be put into the form

$$\begin{aligned} \frac{d}{dt} \left(\frac{v^2}{2} + E_g + E_r + S - \mathcal{E} - \frac{Gm}{r} \right) \Big|_m \\ = -\frac{\partial}{\partial m} (4\pi r^2 v P + L), \end{aligned} \quad (3)$$

where E_g and E_r are the internal gas and radiation energies per unit mass, respectively, and S and \mathcal{E} represent sinks and sources of energy, respectively (e.g., ionization or neutrino losses, nuclear energy generation, etc.). The luminosity L is in general a composite of the photon flux, and convective and conductive energy transport. For the purposes of most hydrodynamic calculations, however, the form

$$\frac{dE}{dt} + P \frac{d}{dt} \left(\frac{1}{\rho} \right) + \frac{\partial L}{\partial m} = \frac{d}{dt} (\mathcal{E} - S) \quad (4)$$

is most useful (here E represents the total specific energy, radiation plus gas), and may be applied in conjunction with equation (2) to specify the time evolution of a given system. The total (mechanical plus radiative plus potential) energy equation (3) may then be utilized as an independent check on the accuracy of the calculational method. This technique is discussed more fully elsewhere, for example by Christy (1964) and Arnett (1966a).

In the absence of local energy sources or sinks, and in regions where the optical depth

$$\tau_r^\nu \equiv \int_r^R \kappa^\nu(r') \rho(r') dr' \gg 1$$

for all frequencies, where κ^ν is the material opacity ($\text{cm}^2 \text{g}^{-1}$) and R is the surface radius of the object, the matter and radiation are strongly coupled: the photon mean-free path λ^ν is small with respect to characteristic fluid distances, and the photon luminosity is given by the diffusion approximation to be

$$L_\nu(r) = 4\pi r^2 F(r) = -(4\pi r^2)^2 \frac{ac}{3\bar{\kappa}} \frac{\partial}{\partial m} (T^4), \quad (5)$$

where F is the photon flux ($\text{ergs cm}^{-2} \text{s}^{-1}$), a is the

Stephan constant, c is the speed of light, and $\bar{\kappa}$ is the Rosseland mean opacity (see Mihalas 1970, pp. 38–40). This approximation requires $T_g = T_r = T$, which implies that the radiation field may be characterized by the Planck function $B(T)$, where

$$\int_0^\infty B^\nu(T) d\nu = \frac{ac}{4\pi} T^4. \quad (6)$$

In order that a single such temperature be well-defined for both the matter and radiation, the condition of local radiative equilibrium (LRE) must obtain, i.e.,

$$\int_0^\infty c \kappa_a^\nu \left[U^\nu - \frac{4\pi}{c} B^\nu(T) \right] d\nu = 0, \quad (7)$$

where U^ν is the monochromatic volume radiation energy density, $\rho E_r^\nu = U^\nu$. The “equilibrium diffusion approximation” also assumes that, to good approximation, $1/c(\partial F^\nu/\partial t) \ll c(\partial U^\nu/\partial r)$. This approach applies in the “plane-parallel limit” at large optical depths, when $\lambda \ll (d \ln T/dr)$. Here it is also reasonable to assume near isotropy of the radiation field. For a more complete discussion of photon transport in this limit, refer to Clayton (1968), Cox and Giuli (1968), Frank-Kamenetskii (1962), or Sampson (1965), for example.

It is also necessary to specify a suitable equation of state for the fluid; that of an ideal gas plus radiation is often reasonable, and was adopted for the calculations discussed below. In addition, for purposes of these calculations, conduction and convection have been ignored, and the energy equation has been solved assuming that energy losses due to ionization are negligible. The radiation pressure gradient is given by

$$-A \frac{\partial P_r}{\partial m} = \frac{1}{c} \int_0^\infty \kappa_T^\nu F^\nu d\nu, \quad (8)$$

where $\kappa_T^\nu = \kappa_a^\nu + \kappa_s^\nu$ is the sum of the monochromatic absorption and scattering opacities. In the diffusion limit, the radiation pressure is equal to one-third the volume energy density of the radiation field, assuming isotropy. The total pressure gradient in equation (2) is then a function of temperature, and the energy equation (4) may be written as a function of temperature, density, and opacity only.

The remaining details in the radiation diffusion-hydrodynamic problem are the boundary conditions. Those at $r = 0$ are simple:

$$\begin{aligned} m(0, t) &= 0, \\ L(0, t) &= 0. \end{aligned} \quad (9)$$

Correspondingly simple conditions are appropriate at $r = R$ when interior regions ($\tau \gg 1$) are of primary interest:

$$\begin{aligned} m(R, t) &= M, \\ P(R, t) &= 0, \\ T(R, t) &= 0. \end{aligned} \quad (10)$$

As the optical depth becomes of order unity, it is appropriate to specify the outer boundary luminosity by the relation

$$L(R) = 4\pi R^2 \sigma T_e^4 = 2\pi R^2 \sigma T^4 \quad (\tau = 2/3) \quad (11)$$

by analogy with the Eddington (boundary) approximation (see, e.g., Rose 1973). In this case, the value of $T(\tau = 2/3)$ is determined by a linear interpolation (or extrapolation, as is appropriate) of the temperature gradient in the outer finite-difference zone(s). If greater attention is to be paid to regions of small optical depth, some modification of this form may be in order; the reader is referred to Mihalas (1970) for a complete discussion of the exact solution in the case of a static atmosphere.

b) Time-Dependent Radiative Transport

It is necessary to abandon the diffusion approximations in regions of low optical depth, in order to properly treat the physics of photon transport when matter and radiation decouple, and to obtain explicit frequency-dependent information from theoretical supernova models. For this purpose, the radiation moment equations of Castor (1972) in the fluid frame are adopted in the form

$$\begin{aligned} \frac{1}{c} \frac{\partial J^\nu}{\partial t} + \rho \frac{\partial}{\partial m} (AH^\nu) - \frac{v}{cr} (3f^\nu - 1) \\ - \frac{1}{c} (1 + f^\nu) \frac{\partial \ln \rho}{\partial t} J^\nu + k^\nu J^\nu = j^\nu \end{aligned} \quad (12)$$

and

$$\begin{aligned} \frac{1}{c} \frac{\partial H^\nu}{\partial t} + A\rho \frac{\partial}{\partial m} (f^\nu J^\nu) \\ + \frac{3f^\nu - 1}{r} J^\nu + k^\nu H^\nu = 0, \end{aligned} \quad (13)$$

where $A \equiv 4\pi r^2$, $f^\nu = K^\nu/J^\nu$ is the "Eddington factor" describing the angular distribution of the radiation field, and J^ν , H^ν , and K^ν are the usual radiation moments (see Castor 1972, or Mihalas 1970, for example), and where k^ν is the monochromatic extinction coefficient, $k^\nu = \kappa^\nu \rho$, and j^ν is the local monochromatic source function ($\text{ergs cm}^{-3} \text{s}^{-1}$).

In the calculations discussed below, the Eddington factor has been taken to have the value $f^\nu = 1/3$ everywhere. It is in general a depth-dependent function because of the presence of a boundary with no incident flux (at $r = R$), and because in spherical geometry the $\tau = 1$ surface subtends a solid angle of less than 2π steradians at a point on the surface $r = R$; this latter condition is responsible for the outward peaking of the radiation field (limit $J = H = K$) pointed out by Chapman (1966). Dilution effects are also important in a spherical system. The spatial character of f^ν cannot in general be specified by any *a priori* relation, but must be determined by an angle-dependent solution of the equation of transfer. These problems have been

discussed elsewhere for a static geometry, notably by Hummer and Rybicki (1970), and Böhm (1973) and references therein. It is worthwhile to note that the radiation field in fact may show large departures from isotropy in the spherical case, even as the optical depth approaches its (finite) limiting value at $r = 0$ (Schmid-Burgk 1973). It is only in the "plane-parallel limit" ($\lambda \ll r$, $\lambda \ll d \ln T/dr$) that the assumption of near isotropy may be taken to be rigorously valid. Thus the Eddington approximation ($f = 1/3$) is in fact an extension of this limit to all radii and optical depths; the moment equations (12) and (13) do, however, explicitly treat the effects of dilution in this limit.

The source function in general reflects contributions due to both emission ζ^ν and scattering,

$$j^\nu = \int k_a^\nu \zeta_u^\nu (T_g, \rho, J^\nu) d\mu + \int k_s^\nu I_u^\nu d\mu. \quad (14)$$

If the absorption and emission processes are isotropic, and in the case of isotropic, conservative (i.e., $\nu \rightarrow \nu' = \nu$) scattering, the quantity $(kJ^\nu - j^\nu)$ will not depend upon the scattering contributions:

$$\begin{aligned} k^\nu J^\nu - j^\nu &= k_a^\nu J^\nu - k_a^\nu \zeta^\nu (T_g) \\ &= k_a^\nu \{J^\nu - B^\nu(T_g)[1 - \exp(-hv/kT_g)]\}, \end{aligned} \quad (15)$$

where for the last equality the matter is assumed to be in local thermodynamic equilibrium (LTE) so that emission is characterized by the Planck function, corrected for induced emission. Under these assumptions, the form of the radiation energy equation (12) is simplified and does not depend explicitly upon scattering contributions.

Following arguments given by Castor (1972), terms of order v/c have been kept only in the zeroth-order moment equation (12), while terms of this order in the first-order moment equation (13) have been neglected. In both equations the derivative $(d \ln \rho/dt)$ is of order v/r , so that v/c terms in Castor's first-order moment equation (34) are of order $(v/cr)H$, small compared with the dominant term kH , as long as the photon mean-free path is smaller than the characteristic radius of the object. If the corresponding terms are neglected in equation (12), the resulting equation will not adequately describe the limiting cases of optical thickness (diffusion limit) and optical thinness (radiation and matter decoupled, wave limit). Because of the presence of strong shock phenomena in the supernova light curve models discussed below, it was desirable to retain the flux time-derivative term in the radiation momentum equation (13).

It is computationally desirable to neglect the frequency derivative terms in both moment equations. This is equivalent to using the frequency-integrated form of these relations, with a subsequent partition into energy groups (frequency bins), subject to the constraint that the bin sizes be large in comparison with Doppler shifts between neighboring finite-difference spatial zones with nonzero relative velocities.

It should be noted that effects of a velocity field have been included explicitly and covariantly in Castor's treatment. His equations are solved in the fluid frame for each such spatial zone, and do not refer to a center-of-mass system. This choice of coordinate frame allows the absorption and scattering coefficients to be defined in a straightforward manner, since the energy and momentum transport phenomena are viewed in the rest frame of the emitters, absorbers, and scatterers. Coherent, isotropic scattering has been assumed. Doppler effects between the various spatial zones are treated as corrections within the framework of the particular iterative scheme employed.

The outer boundary condition must now be considered. The Eddington approximation takes the form

$$H^v = \frac{1}{3} J^v (\tau + \frac{2}{3})^{-1} \quad (16)$$

for the static equation of transfer. This form depends upon the assumption that the net flux is constant through a spatial increment inside $r = R$. It neglects time-dependent effects, however, and effects due to radiation anisotropy and spherical dilution, and further assumes a static fluid. However, any attempts to apply corrections for the latter effects contradict the assumption that $f^v = \frac{1}{3}$ everywhere. Thus the application of a plane-parallel boundary form similar to that suggested by Auer (1967) is appropriate for these initial calculations.

Since in this case the emergent flux is not *a priori* specified, as it is in the case of a static atmosphere problem, it is necessary to "close off" the moment equations at the outer boundary by specifying the value of the spatial derivative term in equation (13). To this end, a second-order Taylor expansion in J^v is made about $m = M(r = R)$:

$$J^v(M - \delta m, t)$$

$$\approx J^v(M, t) - \delta m \frac{\partial J^v}{\partial m} \Big|_{t, M} + \frac{(\delta m)^2}{2} \frac{\partial^2 J^v}{\partial m^2} \Big|_{t, M}. \quad (17)$$

In principle, first- and second-order time derivative terms ought to be included in equation (17), but in practice the choice of centering in time dictated that they be neglected. The spatial terms are most important because of the time-step constraints imposed (see Appendix C); Auer (1967) reports that accuracy near the outer boundary can be improved significantly by the inclusion of the second-order term. It is worth pointing out that an expansion of the form (17) in $(r^2 J^v)$ rather than J^v is necessary only in the limit $J^v = H^v = K^v$.

The value of $J^v(M, t)$ in equation (17) may be given in terms of the boundary flux by a relation of the form

$$J^v(M) = \chi^v H^v(M). \quad (18)$$

The value of χ^v appropriate to the Eddington approximation is $\chi = 2$, which is close to the exact value for the gray case in static atmosphere $\chi = \sqrt{3}$ (see Mihalas 1970, p. 62). The value $\chi = 1$ corresponds to the limit $J = H = K$. As in the case of specifying $f^v(m)$, the

value of χ^v must in general be determined by an explicit angle-dependent calculation.

The matter specific energy E_g is coupled to the radiation field by a relation of the form

$$\begin{aligned} \frac{d}{dt} E_g(T_g, \rho, \mu) + P_g(T_g, \rho, \mu) \frac{d}{dt} \left(\frac{1}{\rho} \right) \\ = 4\pi \int_0^\infty \kappa_a^v [J^v - B^v(T_g)] dv, \quad (19) \end{aligned}$$

where LTE has been assumed for the matter, and μ is a parameter which reflects compositional effects. (For the case of the supernova models discussed below, $M \leq 10 M_\odot$ implies a total ionization energy of $E_i \lesssim 2 \times 10^{47}$ ergs for pure hydrogen, small in comparison with the shock energies implied, of order 10^{50-51} ergs.) By defining the quantity

$$\zeta^v(T_g) \equiv \pi \int_{v(t)}^{v(t) + dv(t)} B^v(T_g) dv / \sigma T_g^4, \quad (20)$$

where $\sigma = ac/4$ is the Stephan-Boltzmann constant, it is possible to write equation (19) in the form

$$\begin{aligned} \frac{d}{dt} E_g + P_g \frac{d}{dt} \left(\frac{1}{\rho} \right) + 4\sigma T_g^4 \int_0^\infty \kappa_a^v \zeta^v(T_g) dv \\ = 4\pi \int_0^\infty \kappa_a^v J^v dv, \quad (21) \end{aligned}$$

which, with an equation of state and the specification of an opacity $\kappa^v(T_g, \rho, \mu)$, determines the gas temperature T_g in terms of the total energy absorbed from the radiation field.

c) Calculational Method

The accuracy of the diffusion approximation at large values of optical depth renders it acceptable as a method for model computations in those optically thick regions, while at lower values of τ a more exact treatment is desired. To this end, the equilibrium diffusion scheme (EDS) is applied to those regions which lie interior to an arbitrarily chosen depth, denoted τ_{NF} , which defines a boundary radius r_{NF} , by considering the monochromatic optical depth scale for which the maximum radial depth ($R - r_{NF}$) occurs at $\tau_{NF} = \tau^v(r_{NF})$:

$$\tau_{NF} \equiv \min_n [\tau^v(r_{NF})] = \min_v \left[- \int_R^{\tau_{NF}} \kappa^v \rho dr \right]. \quad (22)$$

This scheme is based on equations (4) and (5), written in terms of the temperature variable. The equations are linearized in first-order corrections to an extrapolated temperature, and solved iteratively for each timestep by application of the standard tridiagonal method of solution (Richtmyer and Morton 1967) for these equations written in fully backward-differenced form. This choice represents an implicit solution of the spatial variation of T with nearest-neighbor spatial

zone coupling; it is effectively a simultaneous solution of N algebraic equations (N is the number of EDS spatial zones) in N unknowns (corrections for each zone). Exterior to this point, the solution will be obtained by solving the full time-dependent radiative transfer scheme embodied in equations (12), (13), and (21), and called here the time-dependent Eddington approximation (TDEA), since $f^v = 1/3$ everywhere is assumed.

The method of solution of the radiation equations (12) and (13) in this region will also be via a tridiagonal formulation of backward-differenced equations, linear in the variable J^v . Such a solution is required for each frequency bin specified. The resulting values of J^v allow a determination of the zone matter temperature by a Newton-Raphson iterative solution of equation (21).

The two schemes must be "coupled" at the interface boundary (the zone boundary corresponding to the choice of τ_{NF}). This is effected by choosing the approximate matter-radiation temperature $T_{NF+1/2}$ just outside this boundary (i.e., in the interior TDEA zone) by a relation of the form

$$T_{NF+1/2}^4 = \sum_v \frac{4\pi J^v}{c a} = \sum_v \frac{\pi}{\sigma} J^v. \quad (23)$$

The EDS solution is then obtained for the inner region, and a specification of the net flux at the boundary τ_{NF} is then made by application of equation (5). The TDEA solutions for the J^v are obtained for the exterior region, and new material temperatures in these zones determined. A new value for T_{NF} is found, and the process repeated until the desired convergence tolerance is obtained. In the calculations discussed below, both T and J^v were required to converge to one part in 10^4 . The new values of temperature thus determined are used, in conjunction with past values, to extrapolate zone temperatures to new times, and the entire procedure is repeated for the new time step after determining new values of R , v , and ρ for each zone.

The hydrodynamic behavior in both EDS and TDEA regions is determined by an explicit (forward-differenced) application of equations (2) and (3). The presence of shocks is accounted for by introducing a pseudo-viscous pressure term into the fluid momentum equation (2) and also into the total EDS energy transport equation (4) and the TDEA matter-energy equation (21). The details of the hydrodynamic and energy transport solution schemes are presented in Appendix A. The choice of time-step size is limited by various physical time scales, notably the current zone conditions, and by numerical considerations of accuracy and stability. These criteria are outlined briefly in Appendix B.

The execution time for obtaining solutions in this manner increases roughly as the number of frequency bins used in the TDEA region. Since the solution time of an individual tridiagonal matrix will depend on the number of zones to which it is applied, it is seen that it is desirable to choose the EDS-TDEA interface depth to be as small as accuracy considerations will

allow. The diffusion equation may be expected to show significant inaccuracies at optical depths of order unity, and from a consideration of this behavior, outlined in Appendix B, the range $3 \leq \tau_{NF} \leq 5$ has been determined to be minimally acceptable for calculations of supernova light curves. The interface boundary for a fixed choice of τ_{NF} is periodically relocated in the mass coordinate due to the changes of fluid scale and opacity which result from the dynamic motions and time variations in the energy parameters (see Appendix A).

IV. APPLICATION TO SUPERNOVA LIGHT CURVES

a) General Features

The basic elements of the shock wave model for explaining the light curves of supernovae of Type II have been discussed elsewhere (Grasberg, Imshennik, and Nadyozhin 1971; FA; Falk 1974). Important points will be reiterated here for completeness. The propagation of a strong shock wave outward through a stellar envelope of some assumed initial density structure is followed numerically. Extended, low-density red supergiant-like envelopes are favorable choices for the presupernova object. The shock wave deposits mechanical and thermal energy into successive layers of the envelope until it reaches either the envelope surface, or encounters an extended tenuous shell of gaseous material.

The luminosity signatures, the light curves, from these two cases differ markedly, depending essentially upon the presence or absence of such a shell. It appears from the studies of FA that the presence of such tenuous material, extending to a radius $R_0 \approx 10^{15}$ cm and characterized by density of order $\rho \lesssim 10^{-12}$ g cm $^{-3}$, can produce a luminosity peak with width greater than about 10 days. It seems that at least one Type II supernova (1969I in NGC 1058; see Arnett and Falk 1976) does not exhibit such broadened peak behavior; its behavior is consistent with the absence of an extended circumstellar shell. Upon reexamining the SN II data available to us, it does not appear that a case may be made for *any* Type II event having had the broad initial peak associated with Type I supernovae. Because of the diversity in SN II light curve morphology, it is not clear, however, whether the absence of such peaks is a general characteristic of these objects. Since the observational situation is so uncertain, we will consider both possibilities.

A low-density shell diffusively spreads in time what would otherwise be a short-duration pulse of high luminosity ($L_{bol} \gtrsim 10^{44-45}$ ergs s $^{-1}$, typically over periods of several hours to a day or more) occurring as the shock wave encounters the envelope (no shell) photospheric surface. The characteristic photon diffusion time for a region of size ΔR in radiative equilibrium is approximately $t_d \approx (\Delta R)^2/\lambda c = \bar{\kappa}\rho(\Delta R)^2/c \approx \tau\Delta R/c$, where $\lambda = (\bar{\kappa}\rho)^{-1}$ is the photon mean-free path, $\bar{\kappa}$ is the mean extinction opacity of the matter, and τ is the optical depth of the region. Observed peak widths of order $t_p \approx 20$ days imply shell optical depths of order $\tau_s \approx t_d c / \Delta R \approx 100$ for electron scattering

opacities characteristic of peak-epoch temperatures, $T \approx 2 \times 10^4$ K, solar-like compositions, and the shell parameters of FA ($\rho \approx 10^{-12}$ g cm $^{-3}$, $\Delta R \approx 10^{15}$ cm). The subsequent quasi-exponential postpeak decline is interpreted by FA to be the diffusive release of trapped energy by the rapidly expanding envelope ($v \approx 4-6 \times 10^3$ km s $^{-1}$).

Table 1 lists the initial configuration parameters for the models presented here. Models A and B are similar to those reported in FA; model A1 is similar to model A, except that a small density gradient was included with finer spatial zoning over the exterior $2 M_\odot$ or so. Model C was used to elucidate details of the light peak in extended massive shell models. Models D, E, and F consist of an unscaled envelope patterned on an unpublished red-giant envelope after Paczyński; they form a sequence of envelope + no shell (D), envelope + gradient (E), and envelope + gradient + shell (F). The density-mass profiles of these models are shown in Figure 2. For comparison, the Paczyński envelope ($7 M_\odot$) and giant envelopes due to R. Ulrich and J. Scalo are also shown. It can be seen that the shapes of the model envelopes employed adequately resemble the profiles of actual envelope integrations. The variation in absolute density position reflects a somewhat arbitrary choice of radial scaling in some model cases. This scaling is partially justified by noticing the same type of effect in the two $5 M_\odot$ Ulrich-Scalo envelopes, where the radial extent is affected by the absolute magnitude of the star. A difference of 1.25 magnitudes accounts for over a factor of 10 difference in mean density, corresponding to a factor of almost 3 in extension. The assumed radius scaling therefore reflects an assumed brightness choice for the presupernova object.

b) Compact Model

We differentiate between two classes of presupernova configuration; by "compact model" we denote a

superiant envelope without any assumed circumstellar shell. Such envelopes may, of course, be quite extended, possibly having radii of several times 10^{14} cm.

The calculated light curve for the compact model A ($R_0 \approx 1.6 \times 10^{14}$ cm) is depicted in Figure 3. Also shown is the approximate B-band light curve which corresponds to blackbody emission, using the formulae given and discussed in Appendix D. Notice the conspicuous absence of any well-defined initial light peak of 10–20 day duration in the color curves. There is the suggestion of small scale shape in these curves, which may or may not be accurate since the effects of lines and other departures from blackbody radiance have not been explicitly treated.

i) Behavior of the Photosphere

Since the role of the photospheric surface is important in describing the light-curve morphology, a brief description of its behavior in models of this type is in order. At the onset of light maximum, which is characterized by a rapid rise of some 8–10 decades in luminosity over a period of a day or so, the effective photosphere lies some small distance interior to the model outer radius, and surface temperatures imply opacities which lie below the level of the bound-free and free-free "peak" at about 10^4 K (see Fig. 4). As the gas is heated by the passage of the shock front, the temperature rises dramatically, ionization increases, and "ascent of the opacity peak" begins. The photosphere moves outward in mass (and radius) and the photospheric mean velocity exceeds that of the surrounding matter, $v_{ph} > v_m$. As the temperature continues its rise toward a maximum of order 4×10^4 K, the descent of the opacity peak on the high-temperature side occurs, with an accompanying increase in transparency; the photosphere recedes in mass, though by this time material velocities are large, and there is a net rapid increase in radius. During this stage

TABLE 1
MODEL PARAMETERS*

Model	$\frac{M}{M_\odot}$	$(\frac{R_0}{10^{14} \text{ cm}})$	ρ_{in}	ρ_{out}	$(\frac{E_0}{10^{50} \text{ ergs}})$	$\frac{M_s}{M_\odot}$	$ \Omega_0 $	N_z	Remarks
A.....	10.	1.59	1.6 (-8)	4.5 (-10)	9.37	...	1.4 (47)	24	$\rho \propto r^{-2}$
A1.....	10.	1.59	1.6 (-8)	2.0 (-11)	9.37	$\lesssim 0.4$	9.4 (46)	43	+ gradient zoning
B.....	5.24	9.25	1.5 (-10)	4.0 (-13)	3.52	1.5	5.5 (45)	24	$\rho \propto r^{-2}$ (envelope), $\rho \propto r^{-5}$ (shell)
C.....	7.91	10.	2.4 (-9)	1.1 (-13)	16.7	1.5	8.2 (46)	49	Scaled Paczyński envelope + shell
D.....	7.0	0.713	1.06 (-6)	1.17 (-9)	9.98	...	1.03 (47)	23	Unscaled Paczyński envelope
E.....	8.12	4.04	1.06 (-6)	3.25 (-12)	9.98	1.12	1.06 (47)	33	+ gradient zone
F.....	8.70	5.44	1.06 (-6)	2.82 (-13)	9.98	1.69	1.05 (47)	36	+ shell zone
F1.....	8.70	5.44	1.06 (-6)	2.82 (-13)	9.98	1.69	1.05 (47)	36	$\kappa = \kappa_{es} = \text{constant}$

* Initial configurations for the various models presented. Densities given in g cm $^{-3}$; ρ_{in} and ρ_{out} correspond to the envelope interior and exterior finite-difference zone densities, respectively. R_0 is the exterior envelope radius at $t = 0$, in units of 10^{14} cm. E_0 is the shock (kinetic) energy at $t = 0$, in units of 10^{50} ergs, and Ω_0 is the gravitational binding energy (in ergs) of the $t = 0$ finite-difference zoning. M_s is the approximate mass of the zones which can be considered to be additional to the "usual" giant envelope, i.e., the circumstellar shell defined in § II of the text. N_z is the number of finite difference zones used in a given model. Numbers in parentheses refer to powers of 10.

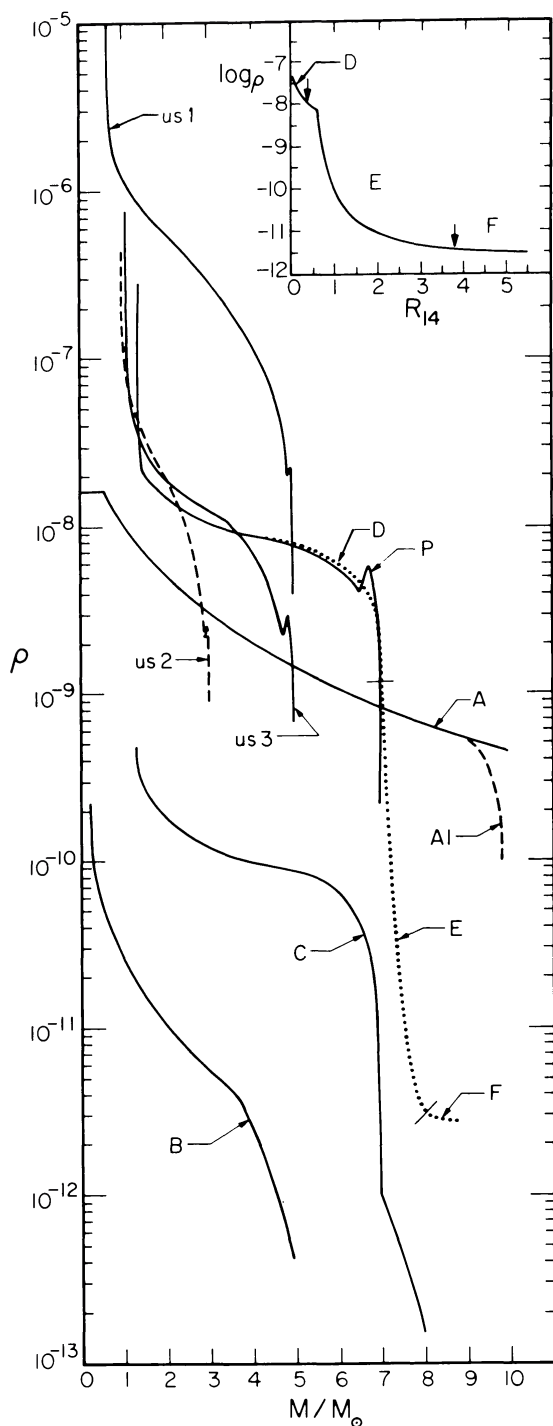


FIG. 2.—Density structure of presupernova giant envelopes. The density profiles of sample envelope integrations due to Paczyński (P) [1971; $7 M_{\odot}$, $M_{bol} = -7.05$, $R_0 = 7.6(13)$] and Ulrich and Scalo [1975; US1: $5 M_{\odot}$, $M_{bol} = -5.5$, $R_0 = 2.7(13)$; US2: $3 M_{\odot}$, $M_{bol} = -6.0$, $R_0 = 4.9(13)$; US3: $5 M_{\odot}$, $M_{bol} = -6.75$, $R_0 = 6.4(13)$] are shown as functions of mass coordinate. Structure curves for the various models are also shown. Model A ($10 M_{\odot}$, $\rho \propto r^{-2}$, $R_0 = 1.6 \times 10^{14}$) represents a “compact” structure. Model B ($5 M_{\odot}$, $R_0 = 9.6 \times 10^{14}$) consists of two distinct regions; for the interior $\rho \propto r^{-2}$, while outside this region $\rho \propto r^{-6}$; this is an “extended” structure (see text). Model C is essentially a scaled (in mass and radius)

$v_m \geq v_{ph}$. As the ionization is completed, and the dominant opacity is due to electron scattering which has a constant value over the higher temperatures attained, $v_m = v_{ph} \approx v(R)$, and for all practical purposes $T_m(R_{ph}) \approx T_e$. As expansion continues and radiative and adiabatic losses result in cooling of the material, the opacity peak (if the density is high enough for one to be present) is first ascended, decreasing transparency and resulting in photospheric advance in mass (usually slight, since expansion effects may dominate the opacity increase), with $v_m \lesssim v_{ph}$. The subsequent descent on the low-temperature side results in increasing transparency, recession in mass of the photosphere, and $v_m > v_{ph}$. In rapidly expanding models, especially the compact types defined below, transparency increase due to expansion alone is always dominant over opacity-peak effects, and even during the electron scattering epoch in the outer layers, $v_m > v_{ph}$ and net recession in mass of the photosphere occurs. However, the major effect of the low-temperature descent from the opacity peak is a rapid increase in transparency in the affected region, as κ drops to well below the electron scattering value. Photospheric recession in mass coordinates is relatively rapid. These results are obtained using a gray opacity; they may be modified when nongray effects are included.

ii) Effective Temperatures

The temperature behavior for model A is shown in Figure 5. The curve labeled T_m is the material temperature in the outer finite-difference zone. At early times, $R_{ph} \sim R$, and this outer mass zone is dominated by material interior to R_{ph} . During this time, $T_m(R_{ph}) \approx T_e$, so the curve labeled T_e gives the appropriate value of the material temperature in the photospheric neighborhood, while the T_m curve shows the zone central temperature. By the time $t_6 \approx 4.4$, however, the photospheric surface lies interior to the midpoint of this zone, and a reasonable determination of $T_m(R_{ph})$ can be made. The transition in the T_m curve at this time reflects this change of character for the curve. Notice that material temperatures at the photosphere are in general higher than the effective temperature during this phase. This may be important if the observed constancy of T_e at late times is to be understood (Kirshner and Kwan 1974).

In the framework of continuum light-curve models the interpretation of the constant value of T_e observed is that an increasing amount of flux is carried in the

version of the Paczyński envelope, having $10 M_{\odot}$ including an approximately $1 M_{\odot}$ “shell”; $R_0 = 1 \times 10^{15}$ cm. The dotted curve labeled D, E, F delineates the structure sequence for these three models. Model D is essentially the Paczyński model ($7 M_{\odot}$); models E and F have successive additions of a $1 M_{\odot}$ gradient and a $0.7 M_{\odot}$ shell. Model A1 (dashed curve) represents a rezoning of the outer $2 M_{\odot}$ of model A, and includes a more realistic gradient region and fine mass zoning. The insert shows typical spatial proportions of these structures, illustrating the extension of the gradient and shell regions in model sequence DEF. The vertical arrows represent the exterior radii of models D and E, respectively.

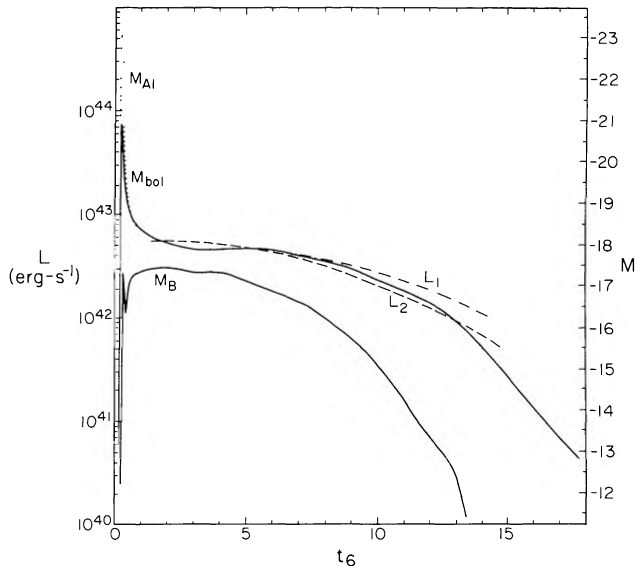


FIG. 3.—Light curve for the compact models A and A1. Total luminosity M_{bol} is shown as a function of time. The bolometric curve for model A contains three distinct phases: (1) peak pulse at $t_6 = t/10^6 \text{ s} \lesssim 0.4$ of duration $\Delta t_6 \approx 0.2$ (decline can be identified with adiabatic $|y| = 4/3$ cooling in the initial rapid expansion); (2) postpeak plateau (cooling and recombination epoch), extending to the declining portion of the curve at $t_6 \approx 10-12$; and (3) final turndown at $t_6 = 13$ as recombination is essentially complete in the envelope. The curve M_B depicts the derived B-band luminosity for a blackbody radiating at the model's effective temperature $T_e(t)$ (cf. Appendix D). The dotted and dashed reference curves represent the function $\exp(-R_0 t/k - vt^2/2k)$ described in the text, for two (arbitrary) choices of $t = 0$. Notice the absence of any conspicuous 10–20 day “peak” in the visual band curve. The curve M_{A1} is the bolometric curve for model A1, calculated only through peak epoch. Its subsequent development is expected to parallel that of model A.

dominant lines, whose emission is characterized by temperatures higher than the continuum value of T_e . The continuum effective temperature actually decreases steadily, but the recession of the photosphere occurs in such a way that the material temperature sampled is only slowly decreasing, falling in the range $T_m \approx 5000-7000 \text{ K}$. Values of T_e obtained by observation for the Type II supernova SN 1969l in NGC 1058 (Arnett and Falk 1976) are also plotted in Figure 5. The agreement with the T_e curve of model A is surprisingly good.

iii) Diffusive Energy Release

The calculated light curve shows at this time a gradual flattening, following a slight increase in the luminosity. The acceleration of the outlying material is essentially completed; expansion is rapid, nearly homologous, and the radiating surface grows more rapidly than photospheric recession in mass can shrink it. As the matter continues to cool and the photosphere moves steadily inward in mass, it samples matter moving at increasingly lower velocities. The increasing transparency of the material dominates the growth of the photospheric surface and the light curve

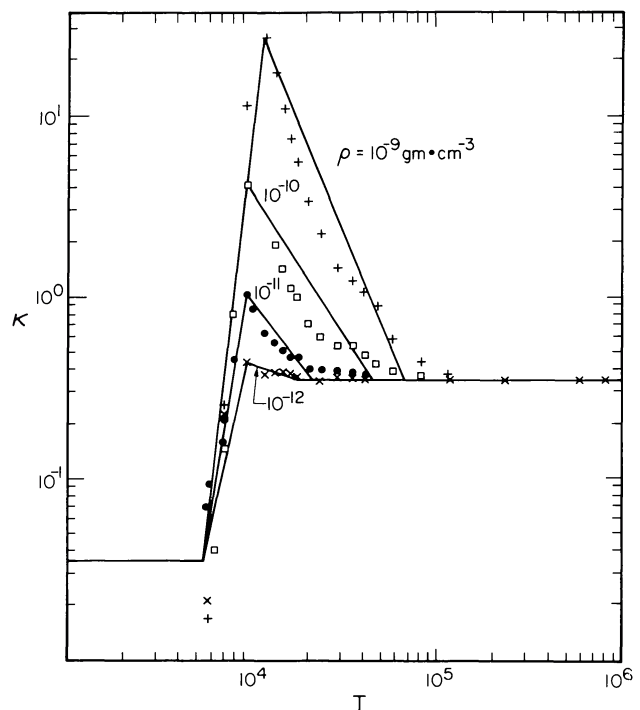


FIG. 4.—Temperature dependence of the opacity. The variation of total opacity κ (in $\text{cm}^2 \text{ g}^{-1}$; Cox and Stewart 1965, Cameron Mixture I) with temperature is shown for typical gas densities. The solid lines represent the chosen fits to the detailed opacities; actual values are plotted as separate points for each density value. The choice of the artificial ledge $\kappa = 0.1 \kappa_{\text{es}}$ for $T \lesssim 6000 \text{ K}$ is arbitrary and was made for calculational convenience (see text for discussion of this point). The value $\kappa = \kappa_{\text{es}}$ obtains for high values of the gas temperature. For the purposes of these calculations, ionization and recombination effects are not explicitly treated, so that these effects enter the transfer calculations only through the corresponding opacity variation with temperature.

flattens out and begins to show a gradual decline. The photon diffusion time for the envelope as a whole is the dominant time scale. Acceleration of all but the interior matter is virtually complete, and the expansion is characterized by constant velocities; the envelope is coasting. The initial decline now is quasi-exponential, with a decay constant $t_d \approx 10.7 \times 10^6 \text{ s}$. A diffusive solution in this case suggests that

$$L(t) \propto \exp(-t/t_d),$$

with the diffusion time characteristically given by

$$t_d \approx \frac{\kappa \rho \Delta R^2}{c} \approx \frac{3M\kappa}{4\pi c} \frac{1}{R},$$

where M is the envelope mass (more properly, the mass interior to R_{ph}) and the envelope extent is $\Delta R \approx R$. For constant expansion velocity, then,

$$R \approx R_0 + vt,$$

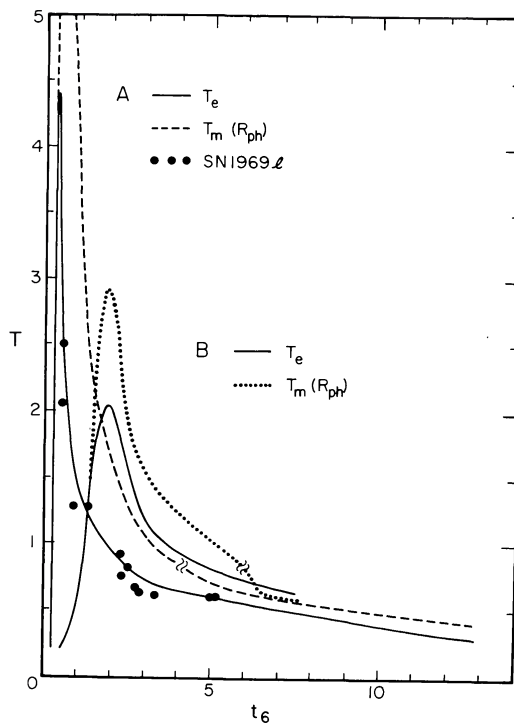


FIG. 5.—Effective temperatures for models A and B shown by the solid lines. The time is given in units $t_6 = t/10^6$ s. The solid circles represent derived values of T_e for supernova 1969I in NGC 1058 (Kirshner and Kwan 1974); the choice of time fit was made so that the observed peak and calculated peak times for model A were coincident. The agreement is remarkable. The dashed and dotted curves represent material temperature in the outer spatial zone (before the breaks) and at the photospheric surface (after the breaks) for models A and B, respectively. The late time flatness of these curves agrees qualitatively with inferred supernova behavior; the shallow decline in effective temperature is within typical observational error. Temperature unit is 10^3 K.

and the net result is that the luminosity may be expected to decline according to

$$\begin{aligned} L(t) &\approx L_0 \exp \left[- \int_0^t \frac{R(t) dt}{k} \right] \\ &\approx L_0 \exp \left(-\frac{R_0 t}{k} \right) \exp \left(-\frac{vt^2}{2k} \right), \quad (24) \end{aligned}$$

where $k \equiv 3\kappa M/4\pi c$ is approximately constant at early times. A reference curve (dashed) for the case $R_0 \approx 2 \times 10^{14}$ and $v = 5000$ km s $^{-1}$ is plotted with the bolometric light curve for model A. The zero time point for this curve is taken (arbitrarily) to be $t_6 = 2.0$, which corresponds in time to the flattening of the velocity curve [$v(R)$] in Figure 6. The excellent “fit” illustrates the diffusive nature of the energy release at this epoch. Such close agreement cannot be interpreted to mean that this phase of the expansion is quite so simple, however. In particular, the velocity of the photosphere decreases continuously, and it is the diffusive release of photons from regions interior to R_{ph} which governs the luminosity decline. The close mimicry of the light curve by the reference curve must

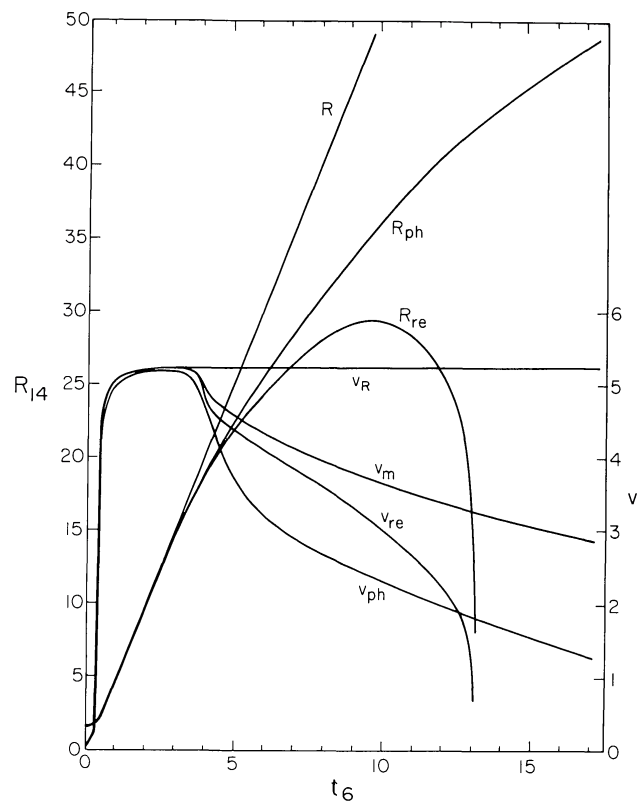


FIG. 6.—The time evolution of various radii and velocities for model A. The curves labeled R , R_{ph} and R_{re} are outer radius, radius of $\tau = 2/3$ surface, and radius of recombination wave ($\kappa = 0.1 \kappa_{es} = \kappa_{min}$), respectively. The apparent discrepancy between R_{ph} and R_{re} is a result of the presence of the artificial level of κ at low temperatures (see text). Radii are given in units $R_{14} = R/10^{14}$ cm, velocities in 10^3 km s $^{-1}$. The curve v_R is the value of the outer mass boundary velocity. The rapid acceleration to nearly final values is characteristic of the compact models. As recombination sets in the outer zones, $R_{ph} < R$ and, similarly, the photospheric mean velocity v_{ph} decreases first sharply and then more gradually from the value v_R . The curves labeled v_m and v_{re} show mass velocities at R_{ph} and R_{re} , respectively. In general, $v_m > v_{ph}$ for the recombination epoch.

be considered to be partly a result of a fortunate choice of “zero time” point. The duration of this decline phase clearly depends upon the envelope mass (specifically, the mass interior to R_{ph}), and, because expansion effects are beginning to result in a rapidly increasing transparency, the light curve declines somewhat more rapidly than the dash-dotted reference curve, which represents $L(t)$ derived from an initial radius $R_0 \approx 5 \times 10^{14}$ and velocity $v \approx 5200$ km s $^{-1}$, corresponding to a choice of zero time at the flat part of the postpeak plateau at $t_6 \approx 4.5$. Slowly expanding, massive envelopes could be expected to remain quasi-exponential for periods longer than, say, 100 days or more before showing any significant change in luminosity decline, *without the presence of any continuous energy input in the central regions*.

Expansion and cooling continue and the envelope becomes increasingly transparent with decreasing density and growing recombination. The characteristic

diffusion time scale at a given instant is of order $t_d \approx k/R$, and the mean value of t_d during this phase is given by

$$\begin{aligned}\langle t_d \rangle &= \frac{1}{t_2 - t_1} \int_{t_1}^{t_2} \frac{k}{R(t)} dt \\ &= \frac{1}{\Delta t} \int \frac{k dt}{R_0 + vt} = \frac{k}{v \Delta t} \ln \left(\frac{R_0 + vt_2}{R_0 + vt_1} \right),\end{aligned}\quad (25)$$

where $k \equiv (3M\bar{\kappa}/4\pi c)$ has been assumed constant. Actually, as recombination proceeds inward, the effective mass in k decreases continuously. If the approximation is made that such decrease is linear over $\langle t_d \rangle$, then the mass is effectively given by $0.5 M$, and $k \approx \frac{3}{8}(\bar{\kappa}M/\pi c)$. Using values typical of model A, $\bar{\kappa} = \kappa_{es}$ and considering the interval $2.6 \leq t_6 \leq 12.0$ suggests a mean value $\langle t_d \rangle \approx 1.0 \times 10^7$ s = 115 days, in reasonable agreement with the calculated light curve. The constant decrease in the effective diffusion time is to turn the curve concave downward (especially for $t_6 \geq 9.0$).

iv) Expansion and Growth of Transparency

Velocity curves $v(t)$ for the photospheric surface, as well as material velocities at the outer radius, $v_R(t)$, and at the photosphere, $v_m(t)$, are shown in Figure 6 with plots of $R(t)$ and $R_{ph}(t)$. The complicated early time behavior of R_{ph} and v_{ph} is not resolved in this model, due partly to the coarseness of the finite-difference zoning and the rapid heating of the exterior layers. The behavior of the photosphere at later times does show a distinct stage when $v_m \approx v_{ph} \leq v_R$, with all approximately constant in time. This interval is a measure of the time postpeak which is required for the onset of recombination in the outer layers, and is consistent in model A with the interpretation of an initially adiabatic cooling of the outer material layers ($\gamma = 4/3$), followed by the diffusive release of energy from interior layers as they relax into their subsequently uniform expansion configuration. [The shape of the $\rho(m)$ curve for $t_6 \approx 0.566$ in Fig. 9 illustrates the preadjustment configuration, with compression evident around $m \approx 4-5 M_\odot$, which disappears essentially by $t_6 \approx 3.0$.] The resulting density profile is then preserved by the virtually homologous character of the velocity profile by this time (cf. Fig. 6). The slight rise in the light curve follows as the diffusive release of energy from the envelope as a whole begins to dominate the energy transport. As expansion continues, recombination sets in, and R_{ph} begins to differ noticeably from R . As recombination continues v_{ph} decreases sharply as the photosphere recedes in mass and finally begins to flatten as the more slowly expanding interior matter is sampled. The material velocity at the photosphere mirrors this behavior, except that v_m is substantially greater than v_{ph} for $t_6 \geq 4$. The choice of $\kappa(T \leq 6000 \text{ K}) = 0.1 \kappa_{es} = \text{constant}$ (see Fig. 4) was made essentially for computational reasons in initial diffusion-approximation calculations. The Rosseland mean opacities used here do not adequately include the effects of Doppler smearing of line opacities into

finite (nonzero) frequency intervals by the large velocity gradient, an effect pointed out by Lasher (1975). Thus the opacity "shelf" may qualitatively mock up even the temperature regime above that for which molecules (and dust) may exist. This lower limit for $\bar{\kappa}$ then implies the result that *the recession of the photosphere is slower than the inward advance of recombination through the envelope*. A finite and non-negligible optical depth will remain between the position of the recombination wave and R , and will decrease only by virtue of the decreasing density of the expanding material. Table 2 lists mass coordinate values for the $\tau = 1$ surface and the recombination "front" as functions of time. This is not as serious as it may on first sight appear to be, since it only becomes a large effect whenever $R_{recomb} \ll R$, even if molecular and/or broadened line contributions to κ are negligible. In particular, the qualitative features of the later light curves are still valid, and the initial phases suffer negligibly from this assumption. If the strength of emission features at later times can be taken as an indication that ionization is in fact not negligible at later times, then electron scattering contributions to the opacity will tend to keep it elevated, even at low temperatures ($T \leq 6000 \text{ K}$), whether or not molecules and/or dust can form at the low densities and values of T implied by the expanding matter. The results of Kirshner and Kwan (1975) in fact suggest that moderately high levels of ionization persist even at late times. They argue, for example, for electron densities of order $n_e \approx 2 \times 10^9$ and $1 \times 10^8 \text{ cm}^{-3}$ for postpeak times of order 40 days and 300 days, respectively, in the case of SN 1969I in NGC 1058. Typical model densities corresponding to the earlier time are $\rho \approx 10^{-13} \text{ g cm}^{-3}$ in the outermost regions, suggesting that $n_H \approx 10^{11}$ or so in the region of the photosphere. Therefore it seems not inappropriate to assume that electron scattering contributions to opacity are in reasonable qualitative agreement with the assumption of a low-temperature opacity "shelf." Since, however, the level of this shelf will in general decrease with increasing recombination in successive layers, the assumption of such a shelf at the level $\kappa = 0.1 \kappa_{es}$ may underestimate the transparency of the envelope exterior to the inward-propagating recombination wave. Consequently, the behavior of the photosphere may be to depart from that of the external mass at earlier times than indicated by the curve, $R_{ph}(t)$. The peak epoch and early post-peak behavior of R_{ph} will be the same in any case, but subsequent recession of the photosphere in mass may be more rapid than predicted here. The limiting form of this recession can be seen from the curve in Figure 6 which shows the position of the recombination wave as a function of time (actually, the position of material whose mean opacity would first fall below the value of $\kappa = 0.1 \kappa_{es}$ for $T \leq 10^4 \text{ K}$). The increase of transparency in this case is much more rapid, suggesting that by times of order 10^7 s the core and/or mantle regions of the supernova should be visible, with little or no envelope continuum obscuration. The qualitative form of this curve is the same as that of $R_{ph}(t)$ in the case of the

TABLE 2
RECESSION OF THE PHOTOSPHERE IN MODEL A*

t	$M_{\tau=1}/M_{\odot}$	M_{re}/M_{\odot}	t	$M_{\tau=1}/M_{\odot}$	M_{re}/M_{\odot}
2.07 (2).....	10.050	...	8.58.....	7.80	0.8
2.09 (5).....	10.050	...	9.08.....	7.54	7.5
3.41.....	10.055	...	9.59.....	7.33	7.1
1.01 (6).....	10.050	10.05	1.01 (7).....	7.12	6.7
2.03.....	10.04	10.04	1.06.....	6.93	5.9
2.51.....	9.98	9.6	1.11.....	6.70	5.4
3.07.....	10.02	9.2	1.16.....	6.51	4.6
3.54.....	10.01	8.8	1.21.....	6.28	3.8
4.01.....	9.60	8.4	1.26.....	5.90	2.5
4.52.....	9.56	8.0	1.31.....	5.80	0.5
5.03.....	9.45	7.1	1.36.....	5.65	...
5.54.....	9.13	6.3	1.42.....	5.45	...
6.05.....	9.07	5.5	1.49.....	5.03	...
6.56.....	8.75	4.2	1.59.....	4.61	...
7.06.....	8.55	3.4	1.68.....	4.19	...
7.57.....	8.72	2.5	1.78.....	3.81	...
8.07.....	8.01	1.13			

* $M_{\tau=1}$ is the mass coordinate of the $\tau = 1$ surface (photosphere) given for various times. M_{re} is the approximate mass coordinate position of the interior front of the "recombination wave" for $t_6 \leq 9.08$; past this time, M_{re} is the mass coordinate of the outer edge of the recombination wave, i.e., for $M > M_{re}$, $\kappa = \kappa_{min} = 0.1 \kappa_{es}$. All values are subject to some uncertainty because of the coarseness of the finite-difference spatial mesh.

assumed opacity shelf; the latter curve will eventually flatten and turn downward as expansion decreases density and optical depth falls. In either case, the photospheric position will then refer to a mass coordinate in core or mantle material. That the position of R_{ph} at late times for this model is roughly constant, and is not yet decreasing, is partially a result of the interior difference zoning assumed. This zoning makes no attempt to include originally high-density ($\rho \gtrsim 1 \text{ g cm}^{-3}$) mantle and core material explicitly. Consequently the interior zone is properly neither a typical envelope zone nor a core-mantle zone, and its behavior cannot be regarded as significant outside the context of the model as a unit. The photospheric "position" in this zone at late times ($t_6 \gtrsim 12$) is therefore only suggestive of the transparent state of the envelope by these times. In particular, by $t_6 \approx 13$ recombination is complete in terms of the continuum opacities.

v) Material Post-Shock Conditions

Models of this type expand virtually homologously and involve no density inversions in the outer material layers. Figure 7 shows the distribution of fluid material velocities plotted against mass for model A, and although the upper curve represents the velocity field at a late time ($t_6 \approx 9.06$), the form of the velocity structure has changed only slightly since the emergence of the shock and the postpeak luminosity decline. A period of relatively rapid readjustment follows the emergence of the shock wave at the stellar surface. It is interesting to notice that the shock disturbance has not completed its energy deposition at peak light, although this is subject to some uncertainty, since the choice of evolution time step may have missed the true luminosity peak by some time $\Delta t_6 \lesssim 0.05$ for this model. Table 3 gives approximate mass coordinate

positions for the pseudoviscous shock "front" for model A at selected times. The emergence of the shock is complete by $t_6 = 0.403$, and the corresponding curve in Figure 7 shows the whiplike effect of shock unloading into essentially a zero-pressure medium. The velocity structure is now virtually determined in form, though significant radiative work ($P_r/P_{tot} \gtrsim 0.99$ behind shock) is expended in the next 4×10^5 to 8×10^5 s in achieving the "terminal," nearly homologous structure by $t_6 \approx 2.0$. The effects of radiation pressure are decreasingly important in the outer regions during the expansion phase, but interior

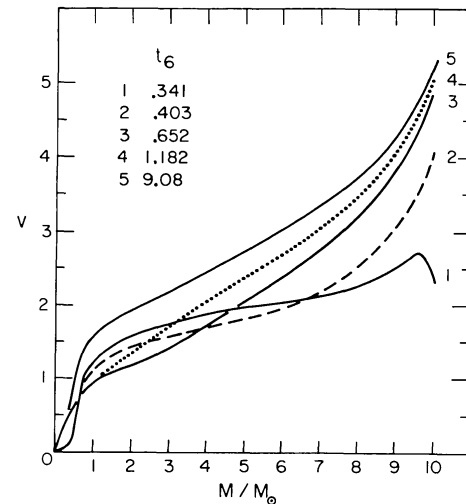


FIG. 7.—The mass-coordinate velocity profiles of model A at various times reflect the development of a nearly homologous expansion characteristic of compact models. The upturn in the outer mass layers is a result of shock acceleration in the density gradient in those regions. The velocities v are given in units of 10^3 km s^{-1} ; times are given in units $t_6 \equiv t/10^6 \text{ s}$.

TABLE 3
SHOCK POSITION IN COMPACT MODEL A AT VARIOUS TIMES*

t	M_{sh}/M_\odot	v_{ms}	$R_{sh}/10^{14} \text{ cm}$	t	M_{sh}/M_\odot	v_{ms}	$R_{sh}/10^{14} \text{ cm}$
2.39	$\lesssim 0.84$	13.8	~ 0.29	1.57	6.90	2.97	1.15
3.91 (3)	1.67	9.03	0.41	1.85	7.54	2.78	1.24
1.94 (4)	2.51	6.15	0.53	2.09	7.96	2.72	1.30
3.27	2.93	5.15	0.59	2.39	8.78	2.54	1.40
4.52	3.35	4.77	0.65	2.69	9.22	2.47	1.48
5.91	3.77	4.22	0.72	2.83	~ 9.57	2.40	~ 1.52
7.68	4.61	3.87	0.82	3.07	~ 9.85	2.36	~ 1.58
9.38	5.03	3.40	0.89	3.29	$\sim 10.$	2.51	~ 1.62
1.14 (5)	5.87	3.33	1.00	3.41	~ 10.05	2.71	~ 1.65
1.37	6.28	3.17	1.06	4.03	No shock	$v_{\max} = 4.07$	$R = 1.86$

* M_{sh} refers to the Lagrangian mass coordinate of the shock front; the pseudoviscous shock is not sharply defined, especially at the two early times. R_{sh} is the approximate Eulerian radius of the shock front, and v_{ms} is the postshock material velocity immediately behind the compression region, in units of 10^8 km s^{-1} . Positions quoted for the last three or four times are especially rough, because of the difficulty of fixing the position of the pseudoviscous shock as it unloads into a zero-pressure medium. All coordinate values are approximate because of the coarseness of the finite-difference mass zoning.

material experiences larger, less diluted flux levels for longer times. Acceleration of mass in these regions continues and results in a moderate flattening of the velocity profile.

The evolution of material temperatures in this model is shown in Figure 8 as curves of T_m versus mass coordinate at selected times. The family of postshock curves ($t_6 \geq 1.007$) reflects a roughly constant, shallow slope, declining in magnitude approximately uniformly in time. The steeper slope (in mass coordinate) in the outer layers does not adequately reflect the greater spatial extension of these regions; the spatial gradient of T_m appears much flatter through these zones and is commensurate with the approximately constant slope obtained in the interior mass. A crude opacity history for the various mass points is also shown: zones with opacities higher or lower than the electron scattering value are qualitatively indicated by vertical dividing lines. The approximate mass coordinate of the photosphere is indicated by an arrow above each curve. Recombination as a sink or source of energy has been neglected. This is clearly justified during the luminosity prepeak and peak epochs when the shock-deposited energy enormously exceeds that invested in ionization, but as the temperature drops below $T \approx 10^4 \text{ K}$ this neglect may be suspect. However, the total energy density of the low-density material interior to the photosphere is dominated by radiative contributions, and recombination is at best an ineffective heating source. The material external to the photosphere was also treated calculationally by the equilibrium diffusion approximation in this model, and for the low material densities encountered, the energy density in this region is radiation dominated, with $\beta' \equiv E_{\text{rad}}/E_{\text{tot}} \gtrsim 0.98$. The conclusion must be that, because of the low densities ($\rho \lesssim 10^{-12}$) (see Fig. 9) which characterize the recombination epoch, recombination heating is inefficient as a mechanism for maintaining approximately

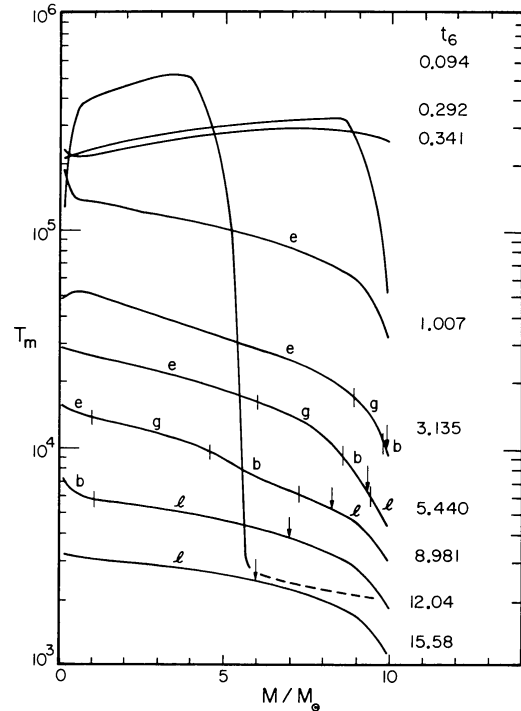


FIG. 8.—Mass-coordinate temperature profiles at various times for model A show the thermal progression of the shock wave ($t_6 = 0.094$ and 0.292) and postpeak cooling to an approximately constant (and apparently flattening) profile by $t_6 \approx 12$. The arrows represent the location of the photospheric surface. Vertical line segments break the curves into opacity regions as approximate functions of temperature. Sections labeled *e* represent regions with predominantly electron scattering opacity κ_{es} . Regions with opacities $\kappa > \kappa_{es}$ (recombination epoch) are denoted *g*, while those regions with $0.1 \kappa_{es} < \kappa < \kappa_{es}$ are denoted *b*. Portions of the curves labeled *l* correspond to regions with $\kappa = \kappa_{\min} = 0.1 \kappa_{es}$. The relatively large value of κ_{\min} leads to a finite optical depth between the recombination wave and the photosphere. The gradual temperature gradient is even more marked in plots of $T_m(r)$.

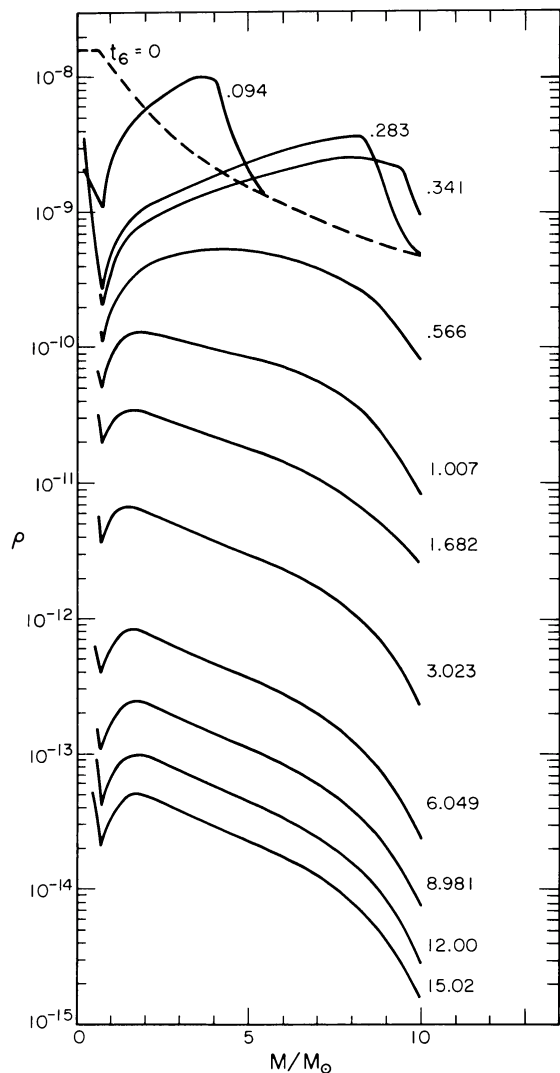
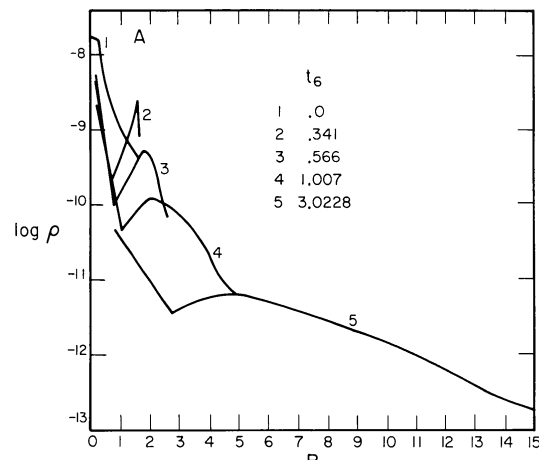


FIG. 9a (left).—Mass coordinate density profiles at selected times for model A show the progress of the pseudoviscous shock compression ($t_6 \leq 0.283$), shock unloading ($t_6 \approx 0.341$), and postshock adjustment ($t_6 \leq 1.007$). The nearly constant profile shape for the later times is a result of nearly homologous expansion and so is a characteristic of compact models. Density is given in g cm^{-3} .

FIG. 9b (right).—Spatial coordinate density profiles at selected times for model A show the qualitative features of shock propagation and postshock adjustment, including the rapid spreading of the shell-like structure of the ejecta at $t_6 \lesssim 0.566$. Compact models apparently produce dispersion of any shell-like configuration by early in the postpeak epoch, a result of homologous expansion character. Radius coordinate is given in units of $R_{14} = R/10^{14} \text{ cm}$; the density is given in units of g cm^{-3} .



constant material temperatures over protracted times. The observed behavior of T_e must be in part affected by the presence of growing radiation transport via strong lines.

Figures 9a and 9b show the mass coordinate and spatial profiles of material densities for model A. The persistence of an approximately constant $\rho(m)$ profile shape in the postshock epoch is readily apparent from Figure 9a, and results essentially from the homologous nature of the material expansion. Notwithstanding this shape constancy, ejecta of this type tend toward a configuration which does not resemble a well-defined spherical shell. On the contrary, any such initial

“shell-like” structure (not to be confused with the presupernova circumstellar shell defined in § II) is a result of an overall shock compression of the entire envelope, which subsequently tends to spread out rapidly. In the case of model A specifically, the “shell-like” configuration at $t_6 \approx 0.566$ with “thickness” $\sim 1 \times 10^{14} \text{ cm}$ has a “thickness” of some 10^{15} cm ($\sim R!$) by $t_6 \approx 3.0$ (cf. Fig. 9b).

vi) Final Luminosity Turndown

As the interior reaches of the envelope recombine and the opacity there declines sharply at low tempera-

ture, the light curve shows a distinct turndown ($t_6 \approx 13.0$). Previously, the photon leakage rate from these optically thickest interior regions was controlled by whatever material remained with $\kappa \geq \kappa_{es}$. As the opacity declines from this value, the local leakage rate increases marginally ($L \propto \kappa^{-1}$), and causes a barely perceptible flattening of the concave light curve ($t_6 \geq 12.0$) just prior to the final turndown. The initial stage, at least, of this final decline is also quasi-exponential, and is characterized on the whole by a new value of the "constant" opacity. In this calculation, $\kappa = \text{constant} = 0.1 \kappa_{es}$ for low temperatures suggests that the initial e -folding time for this epoch should be of order one-tenth that value at $t_6 \approx 6.0$, and this is indeed the case. The situation by this time is more complex

than this simple view suggests, but it serves to illustrate the basic behavior leading to the particular morphology of the light curve. The material temperature which characterizes the recession of the photosphere and the final turndown of the light curve depends critically upon the composition choice for a given model. In these calculations, a Population I composition has been assumed. Table 4 summarizes the evolution of various quantities for model A.

c) Extended Models

We mean by "extended model" that the presupernova configuration includes a supergiant envelope and an overlying circumstellar shell as defined in § II.

TABLE 4
MODEL A EVOLUTION*

<i>t</i>	<i>R</i>	<i>R_{ph}</i>	<i>v_{ph}</i>	<i>v_m</i>	<i>v_R</i>	<i>T_e</i>	<i>T_m</i>	<i>L_t</i>	<i>K</i>	<i>L_{bol}</i>
0.0	1.588	1.588	<0	2.2 (−1)	2.2 (−1)	0.208	0.50	2.1 (−10)	0.385	3.56 (38)
0.267	1.588	1.588	...	3.65 (1)	3.64 (1)	0.769	4.0	1.2 (−7)	0.384	6.28 (40)
0.283	1.588	1.588	0.20	9.25 (1)	9.23 (1)	1.281	5.8	1.37 (−6)	0.384	4.85 (41)
0.288	1.589	1.589	0.18	4.70 (2)	4.69 (2)	2.401	10.3	4.16 (−5)	0.384	6.00 (42)
0.303	1.592	1.591	0.18	1.30 (3)	1.30 (3)	3.485	14.9	3.20 (−4)	0.390	2.72 (4)
0.320	1.608	1.608	0.81	2.35	2.35	4.409	18.6	1.40 (−3)	0.407	7.29 (43)
0.340	1.646	1.646	1.90	2.35	2.35	3.683	14.6	6.58 (−3)	0.477	4.53 (43)
0.403	1.859	1.859	3.98	4.07	4.07	2.681	9.8	8.71 (−3)	0.541	1.75 (43)
0.478	2.183	2.183	4.32	4.54	4.55	2.219	7.5	0.0100	0.598	1.16 (43)
0.565	2.594	2.594	4.72	4.75	4.75	1.960	6.1	0.0110	0.640	9.53 (42)
0.652	3.012	3.011	4.79	4.86	4.86	1.438	3.5	0.0140	0.746	6.94 (42)
1.007	4.777	4.774	4.97	5.04	5.05	1.291	2.94	0.0151	0.769	6.43 (42)
1.189	5.701	5.697	5.07	5.09	5.09	1.082	2.1	0.0178	0.828	5.76 (42)
1.578	7.692	7.682	5.10	5.13	5.14	0.820	1.32	0.0227	0.869	4.78 (42)
2.453	12.214	12.174	5.13	5.17	5.19	0.689	0.99	0.0265	0.894	4.24 (42)
3.252	16.364	16.276	5.13	5.18	5.21	0.667	0.90	0.0304	0.908	4.99 (42)
4.013	20.331	18.826	3.35	4.82	5.21	0.644	0.85	0.0320	0.913	4.87 (42)
4.321	21.941	19.908	3.51	4.72	5.22	0.609	0.73	0.0341	0.917	4.57 (42)
4.727	24.058	21.600	4.17	4.68	5.22	0.585	0.69	0.0365	0.922	4.56 (42)
5.235	26.708	23.412	3.57	4.57	5.22	0.559	0.67	0.0394	0.926	4.36 (42)
5.845	29.889	24.989	2.59	4.36	5.22	0.534	0.64	0.0417	0.929	4.16 (42)
6.352	32.536	26.779	3.53	4.29	5.22	0.499	0.61	0.0455	0.932	3.76 (42)
7.264	37.289	29.246	2.71	4.09	5.22	0.466	0.58	0.0486	0.934	3.33 (42)
8.074	41.516	31.538	2.83	3.97	5.22	0.430	0.54	0.0516	0.935	2.81 (42)
8.981	46.246	33.907	2.61	3.83	5.22	0.415	0.53	0.0528	0.936	2.58 (42)
9.385	48.355	34.917	2.50	3.77	5.22	0.389	0.48	0.0533	0.937	2.18 (42)
10.090	52.034	36.570	2.34	3.67	5.22	0.371	0.45	0.0546	0.937	1.92 (42)
10.595	54.666	37.726	2.29	3.61	5.22	0.353	0.45	0.0555	0.937	1.67 (42)
11.097	57.292	38.778	2.10	3.54	5.22	0.336	0.43	0.0563	0.937	1.45 (42)
11.600	59.914	39.849	2.13	3.46	5.22	0.317	0.41	0.0572	0.938	1.21 (42)
12.205	63.069	41.026	1.95	3.40	5.22	0.300	0.39	0.0579	0.938	9.93 (41)
12.807	66.723	42.170	1.90	3.32	5.22	0.279	0.35	0.0583	0.938	6.04 (41)
13.309	68.830	43.063	1.78	3.28	5.22	0.257	0.33	0.0587	0.938	4.37 (41)
13.812	71.453	43.915	1.69	3.21	5.22	0.235	0.30	0.0590	0.938	2.71 (41)
14.315	74.075	44.749	1.66	3.15	5.22	0.206	0.27	0.0592	0.938	1.32 (41)
15.019	77.750	45.816	1.52	3.08	5.22	0.170	0.22	0.0595	0.938	7.30 (40)
16.083	83.301	47.296	1.39	2.95	5.22	0.145	0.19	0.0595	0.938	4.24 (40)
16.988	88.023	48.449	1.27	2.88	5.22	0.125	0.16	0.0596	0.938	
17.853	92.538	49.438	1.15	2.79	5.22					

* The time evolution of several quantities of interest for the compact Model A. *R* and *R_{ph}* are the outer and photospheric radii in units of 10^{14} cm, respectively. The values *v_{ph}*, *v_m*, and *v_R* refer to the mean photospheric velocity, velocity of mass at the photospheric surface, and velocity of the outer Lagrangian mass point, respectively, in km s^{−1}, unless otherwise indicated. (As before, numbers in parentheses denote powers of 10.) The absence of monotone behavior in *v_{ph}* is a result of coarse finite-difference zoning. *T_e* and *T_m* are the effective temperature and material temperature at *R_{ph}* in units of 10^4 K. *L_t* and *K* are $\int_0^t L_{\text{bol}} dt$ and the total kinetic energy in the mass motions, normalized to the initial shock energy *E₀*. The quantity *L_{bol}* is the value of the bolometric (total) luminosity at the particular time *t*. All times given in units $t_6 \equiv t/10^6$ s.

The behavior of this class of models is very different from that discussed above for a typical "compact" presupernova structure (bare envelope). The importance of examining such models is suggested by the observation of Colgate and White (1966) that compact configurations suffered severe adiabatic losses and were therefore not efficient radiators of visual light. It is desirable, therefore, to study those configurations which do radiate more efficiently, in order to determine the applicability of such structures in explaining the light curves. Observational evidence also suggests that large radii ($r \approx 10^{15}$ cm; see Arp 1961b and Kirshner, Arp, and Dunlap 1976) are implied. While this evidence by no means impels us to the conclusion that presupernovae are this extended, we feel that the possibility cannot be entirely ruled out. Too, massive stars may be expected to suffer extensive mass loss, whether as single stars with strong winds or in a binary system (with circumbinary envelopes?); such flows may indeed result in extended low-mass shells surrounding the parent system. Finally, the study of extended low-density systems will provide insight into the physical character of the "nebular" stage of the expanding ejecta (cf. § I).

i) Model B

We turn our attention now to consideration of model B. Its bolometric and approximate "visual" light curves are shown in Figure 10. An immediately obvious difference from the light curve for model A is apparent: a well-defined and broad ($t_p \approx 9.4 \times 10^5$ s ≈ 10.4 d) light peak results from the presence of low-density material ($4 \times 10^{-12} \gtrsim \rho \gtrsim 4 \times 10^{-13}$ g cm $^{-3}$) which extends to a large radius, $R_{14} \equiv R/10^{14}$ cm ≈ 9.24 . A detailed description of the peak epoch for extended models is presented below, in the context of model C, so no attempt at completeness is made here.

An essential difference between model types A and B is the delay of the emergence of the shock wave at the stellar photosphere. The propagation of the pseudoviscous shock is summarized in Table 5, which gives its mass and radial coordinates and local postshock velocities for selected times. Low material densities allow radiation to diffuse ahead of the shock, producing a light peak with base width $\Delta t_p = 26.6$ days, which compares well with the photon diffusion time across the initial "shell" configuration, $t_{dp} \approx 27.7$ days. The radiation produces some heating in advance of the viscous shock. Such an effect is evident in the earliest curve of Figure 11, showing $T(m)$ at a time approximately 14 days before peak light. Subsequent radiative heating of the outlying material is slower than is the case for model A, but postpeak behavior of the $T(m)$ profile is similar to the evolution of the profile in model A. We reiterate the observation that the spatial gradient of T_m is indeed flatter in the outermost layers, although it does not appear so in the mass coordinate plot.

Radiative acceleration is not as efficient as shock acceleration was in the case of model A, and resulting velocities are lower, $v \approx 2200$ km s $^{-1}$. Figure 12 shows the development of the velocity profile for model B. The most noteworthy feature is the constancy of material velocities over a large fraction of the expanding envelope.

The immediate postpeak decline is approximately exponential and represents the initial cooling phase of the envelope, before expansion has greatly enlarged the radiating surface. During this phase,

$$L \propto \exp(-R_0 t/k) \propto \exp(-t/t_{d0}),$$

and $R_0 \gtrsim v\Delta t$. As expansion continues, the radiating surface grows rapidly, and the light curve begins to flatten and perhaps rise slightly. Cooling continues

TABLE 5
SHOCK POSITION IN EXTENDED MODEL B*

t_6	M_{sh}/M_\odot	v_{ms}	$R_{sh}/10^{14}$ cm	t_6	M_{sh}/M_\odot	v_{ms}	$R_{sh}/10^{14}$ cm
0.100.....	1.15	4.8	2.21	1.49.....	4.30	2.07	7.10
0.201.....	1.36	4.1	2.75	1.59.....	4.50	2.06	7.6
0.302.....	1.78	3.6	3.27	1.69.....	4.50	2.05	8.2
0.402.....	2.20	3.25	3.80	1.79.....	4.6	2.04	8.3
0.502.....	2.41	3.0	4.09	1.89.....	4.7	2.03	8.36
0.573.....	2.62	2.8	4.36	2.04.....	4.7	2.03	8.7
0.675.....	2.83	2.7	4.64	2.24.....	4.6	2.04	9.2
0.775.....	3.04	2.55	5.10	2.44.....	4.4	2.05	9.4
0.877.....	3.40	2.4	5.44	2.64.....	4.4	2.07	9.6
0.981.....	3.55	2.3	5.72	2.84.....	4.6	2.08	9.7
1.08.....	3.77	2.25	6.04	3.04.....	4.6	2.09	9.9
1.18.....	3.97	2.18	6.41	3.44.....	4.7	2.10	~ 10.7
1.29.....	4.08	2.10	6.65	3.95.....	4.8	2.11	~ 12.1
1.39.....	4.19	2.09	6.91				

* Quantities are defined as in Table 3; $t_6 \equiv t/10^6$ s = 1.89 corresponds to maximum light. As in the case of Model A, the position of the pseudoviscous shock "front" is somewhat uncertain. The apparent partial reflection of the shock at postpeak times is a result of the presence of low-density "shell" material for which typical photon diffusion times are short compared with local sound times; the resulting radiative acceleration of these layers is inefficient. The development of a density inversion leads to turbulent pressures, which in this model result computationally only in an extra pseudoviscous pressure. Hence the approximate mass coordinate of the "shock" seems to retreat and finally advance again for $t_6 \approx 2.8$. The quantity R_{sh} is very uncertain for $t_6 \gtrsim 2.2$ because of this partial reflection near the outer material boundary.

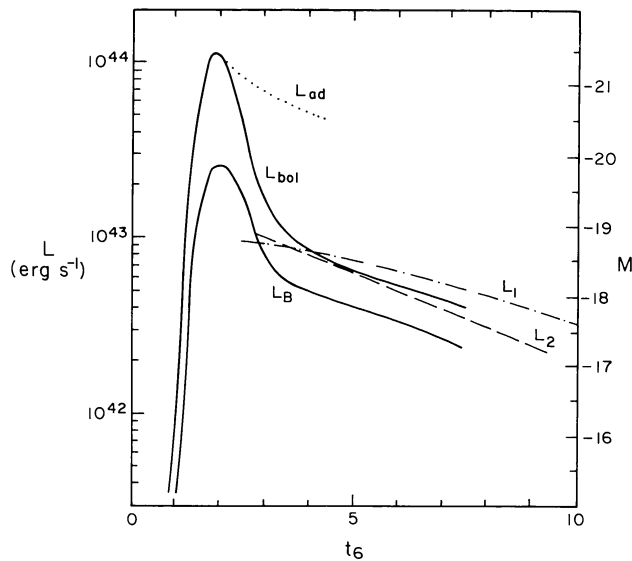


FIG. 10.—Light curves for the extended model B. The bolometric (total luminosity) curve L_{bol} (ergs s^{-1}) for model B is given by the heavy solid line. The other solid line L_B shows the approximate B -band luminosity curve for the model, derived for a blackbody at temperature $T_s(t)$ (cf. Appendix D). Notice first the presence of a broad ~ 15 day bolometric light peak which is mirrored in the B -curve by a similar ~ 15 day peak. These broad peaks are typical of extended models, and are *not* merely temperature effects. The similarity of visual and bolometric curve shapes is also characteristic. The immediate postpeak decline is predominantly a diffusion characteristic of the presupernova “shell” structure (cf. § II of text), and is not in general the result of adiabatic losses: the curve L_{ad} shows the approximate luminosity evolution for an adiabatically cooled gas, expanding at the moderate ($v \approx 2000 \text{ km s}^{-1}$) velocities of model B. The reference curves labeled L_1 and L_2 show functions $\exp(-R_{\text{ot}}/k - vt^2/2k)$ and $\exp(-t/t_{\text{do}})$ (see discussion in text) which bracket the postpeak decline. The quasi-exponential character of L_{bol} is at least partially a result of the relatively low expansion velocity in this model. The postpeak epoch is a cooling and recombination epoch, as in the case of model A, and the curves are expected to turn downward when $\kappa = \kappa_{\text{min}}$ throughout the envelope.

and recombination sets in by $t_6 \approx 6.6$, so the photospheric radius begins to differ from $R(t)$. Subsequent evolution, beyond that calculated here, will bring continued cooling and recombination, and in addition, the stage where expansion effects begin to dominate the diffusion character. The light curve may be expected, as was the case for model A, to show a downward concavity as t_d decreases continuously. During this phase of expansion, $vt > R_0$, and the term $\exp(-vt^2/2k)$ begins to dominate the luminosity decline. By this time the envelope has assumed a definite shell-like structure which can be discerned in the density profile plots of Figures 13a and 13b. Typical radii are shown for the curve at $t_6 = 6.37$. The density inversion is extremely pronounced, and will be discussed more fully below. A characteristic time scale for this region is $t_d \approx 2.5 \times 10^5 \text{ s} = 2.9$ days, too short for this region to have a noticeable effect upon the general character of the light curve. An estimate for the initial envelope diffusion time is $t_{\text{do}} \approx 4.3 \times 10^6 \text{ s} \approx 50$ days, considering only that mass

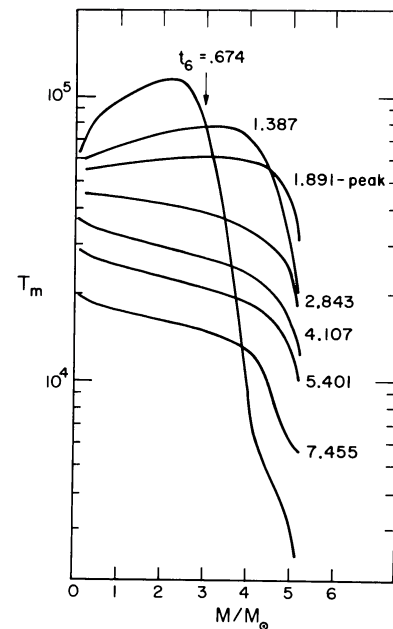


FIG. 11.—Mass coordinate temperature structure of model B at selected times, in many respects similar to the behavior noted for model A except that the outer mass layers (not as spatially extended) have a somewhat steeper temperature gradient. The nonhomologous nature of the expansion in this model precludes the preservation of a similar profile in the outer layers during the course of the expansion.

interior to the density inversion. A reference curve with this value of decay constant is shown in Figure 10, and agrees well with the early postpeak decline. Some flattening is evident by $t_6 \approx 7.0$, and the subsequent decline is expected to mirror that of model A, at least

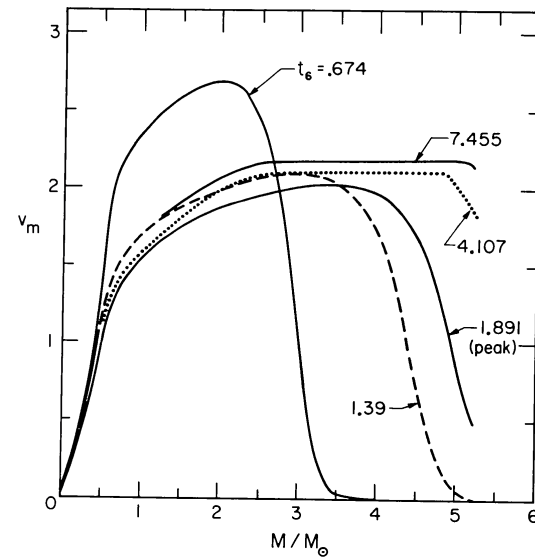


FIG. 12.—Mass coordinate velocity profiles at selected times for model B show two characteristics of extended models: (1) relatively slow acceleration of outer mass zones to only moderate velocities by the diluted radiation flux, and (2) the approximate constancy of material velocities v_m (in 10^3 km s^{-1}) as acceleration is completed (by $t_6 \approx 7.455$).

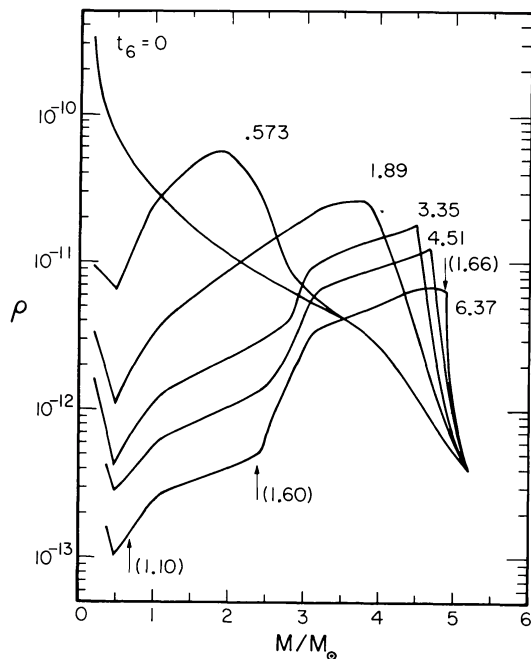
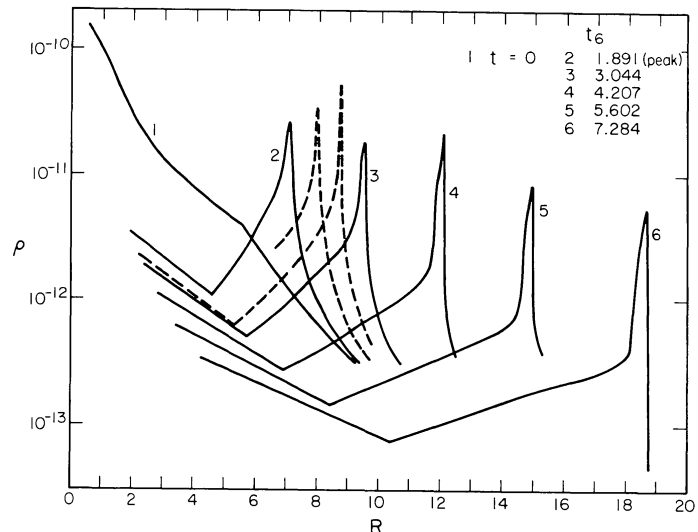


FIG. 13a (left).—Mass-coordinate density profiles at selected times for model B show the broad compressional character of the pseudoviscous shock at low densities. The appearance and development of a “shell-like” structure in the outer mass layers ($M/M_{\odot} \gtrsim 2.7$) is coincident with efficient photon leakage from this low-density region which prevents the buildup of sufficient mechanical gas pressure to spread the density inversion. The arrows and numbers in parentheses show radii (in $R_{15} \equiv R/10^{15}$ cm) at various points in the curve for $t_6 = 6.37$. The inversion is spatially confined relative to the overall extent of the expanding envelope, and covers only some 6×10^{13} cm.

FIG. 13b (right).—Spatial coordinate density profiles at various times for model B emphasize the development of the compressed density inversion. Persistence of this feature suggests that extended models are characterized by expansions of this type. The shell-like density inversion will in fact reach much higher values of $\Delta\rho/\rho$ than those shown, which were limited by the introduction of a second pseudoviscous pressure $\propto \Delta\rho/\rho$ (not as efficient as the method outlined in Appendix C). The dashed lines show similar profiles for the same preshock configuration where the calculation did not employ the second pseudoviscosity. The rapid growth of inversions of this magnitude greatly slows the calculation of the expansion. As in the case of model A, the region interior to the density spike spreads itself out, a result of an outwardly increasing velocity profile in this region. Velocities in the immediate density spike mass layers are approximately constant. Radii are given in units $R_{14} \equiv R/10^{14}$ cm.

in form. The second reference line shows the curve $L(t) = L_0 \exp(-R_0 t/R) \exp(-vt^2/2k)$; as for the case of model A, this somewhat overestimates early postpeak luminosities, but the general agreement with the calculated curve suggests that this simple diffusive interpretation well approximates the postpeak light curve before the completion of recombination, even for extended models like model B.

The slow increase of velocity in the outermost layers results from both low material densities ($\rho \leq 10^{-12} \text{ g cm}^{-3}$) and the dilution of the radiation flux by the large distance implied ($R \approx 10^{15}$ cm). Figure 14 shows the time history of the velocity and radius parameters. The initially large “pulse” of velocity attributed to the photosphere is a result of the sharp increase in opacity of the exterior mass as it is radiatively heated. Material motions are negligible in the vicinity of the photosphere at very early times, but throughout the immediate postpeak expansion, $v_m > v_{ph} > v(R)$, an artifact of the negative velocity gradient in the photospheric layers. As acceleration of these regions continues, $v_m \approx v(R)$ until noticeable recombination leads to photospheric recession in mass, already begun by $t_6 \approx 6.6$. As expansion progresses beyond the phase calculated, recombination continues,



and the behavior of v_{ph} may be expected to parallel that obtained for model A. A gradual flattening of the light curve (present by $t_6 = 7.0$) is present during the early recombination phase as R_{ph}^2 increases more rapidly than transparency increases. Following this will be quasi-exponential decline turning concave downward as t_d decreases continuously because of expansion and photospheric recession. The evolution of model B quantities is summarized by Table 6.

ii) Other Models

A sequence of peak epochs was calculated based on an initial configuration closely resembling an unpublished $7 M_{\odot}$ red-giant envelope integration by Paczyński. The bolometric light curves for these models are shown in Figures 15a and 15b. Recall that model D represents an initial envelope configuration without any density gradient zoning, while models E and F have successive additions of gradient and shell zoning (cf. Fig. 2). Model D closely parallels the behavior of model A—a spiked pulse of luminosity as the shock emerges at the photosphere ($R_0 \approx 7 \times 10^{13}$ cm), followed by a brief quasi-exponential decline phase which flattens as recombination sets in.

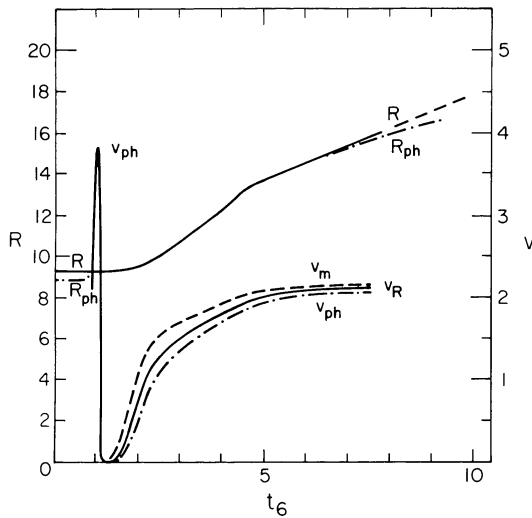


FIG. 14.—Evolution of material velocities and radii for model B. Curves marked R and R_{ph} show the radii (in units $R_{14} \equiv R/10^{14}$ cm) of the outer mass point and photospheric surface, respectively. At early times $R_{ph} < R$ in the low-density, highly extended circumstellar “shell” portion of the presupernova structure (cf. Fig. 2). Shock compression and the subsequent rapid heating of the outer layers cause the photospheric surface to expand in mass coordinate, and it is thereafter essentially coincident with the outer radius of the expanding envelope until recombination sets in at $t_6 \approx 6.5$. These curves have been extrapolated for $t_6 \gtrsim 7.5$ in order to show this effect more clearly; hence the broken curve for R at these late times. The curves labeled v_R , v_m , and v_{ph} show, respectively, velocities (in units of 10^9 km s $^{-1}$) for the outer mass point, material at the photospheric surface, and the derived average velocity of the photospheric surface itself. The curve v_{ph} has been drawn as a solid line for $t_6 \lesssim 1.2$ to emphasize the initially rapid outward motion of this fictitious surface (cf. discussion in text); after $t_6 \approx 1.2$ this curve is given by the dashed-dotted curve, and thereafter $v_{ph} < v_R$. Notice that material velocities at the photosphere are larger than v_R throughout the pre-recombination epoch. If the calculation were extended to later times, v_m would decrease to values $< v_R$ as the photosphere receded in mass coordinate. This decrease would, however, be gradual, owing to the near constancy of material velocities in the outer mass layers. The curve for v_{ph} would also be expected to show a gradual decrease ($v_{ph} < v_m$ always), as was the case for model A (cf. Fig. 6).

Model E has a $1.12 M_\odot$ “gradient” extending to $R_0 \approx 4 \times 10^{14}$ cm which serves to spread the luminosity spike of model D into a broader peak with base width $t_p \approx 10^6$ s ≈ 11.6 d. Model F has, in addition, a $0.57 M_\odot$ of nearly constant density $\rho \approx 3 \times 10^{-12}$ g cm $^{-3}$ and extending to a radius $R_0 = 5.4 \times 10^{14}$ cm; the resulting light peak for this model has a base width $t_p \approx 2.4 \times 10^6$ s ≈ 28 days. These peak widths compare favorably with the diffusion times across the gradient and/or shell regions, $t_{dp} \approx 1.5 \times 10^6$ s and $t_{ap} \approx 2.35 \times 10^6$ s, respectively. Figure 16 shows the time evolution of the various velocity and radius parameters for these models. Their behavior is similar to that of the previously discussed models; the more extended models show progressively lower expansion velocities as outlying regions rely upon acceleration by increasingly diluted radiation fluxes. Details of the development of these models are given in Tables 7, 8, and 9.

d) Details of the Light Peak

The use of a hydrodynamic-equilibrium diffusion calculation yields all the features discussed above, in fair quantitative agreement with the observations (Arnett and Falk 1976). The details of the peak epoch, however, are far more complicated, and in general good quantitative results depend upon utilizing a hydrodynamic photon-transport calculation. In what follows, such a calculation scheme, which was previously outlined, was employed. In order to present the general features of these models, a calculation (model C) which used three distinct energy (frequency) bins will be discussed: bin 1 contained all frequencies shortward of 4000 Å; bin 2 included $4000 \leq \lambda \leq 7000$ Å; and bin 3 consisted of all energies longward of 7000 Å. The calculation was “nongray” in that the Cox-Stewart Population I Rosseland mean opacities (Cameron Mixture I, Cox and Stewart 1965) were employed in conjunction with bin emissivities characterized by the “blackbody fractions” defined in Appendix A, equation (31). No attempt to employ opacity means over individual bins was made, however, so in this sense the calculation was formally a “gray” one. Absorptive opacities were obtained by extrapolating a temperature fit to the Cox-Stewart tables via a Kramers’s relation for free-free transitions (Clayton 1968, p. 216), in order to suppress a spurious electron scattering contribution at higher temperatures. This particular choice allows a straightforward comparison with the earlier results of FA, and is insensitive to any peculiar differences which would result from independently created opacity tables.

i) Shock Propagation

The model presented here was patterned after an unpublished Paczyński envelope integration for an extended red giant; the finite difference zoning is reflected in Figure 2. Six mass zones per decade in density were used in the steep gradient, which contained a mass of approximately $1.5 M_\odot$, including a shell mass of $M_s \approx 0.5 M_\odot$. Initial radius was 1×10^{15} cm with a total mass of $M = 7.91 M_\odot$ and a shell “surface” density $\rho \approx 1.1 \times 10^{-13}$ g cm $^{-3}$. The shock was introduced in the form of a moving mass plate at the center (cold piston), with velocity $v \approx 1.5 \times 10^4$ km s $^{-1}$ corresponding to an energy of 1.665×10^{51} ergs. Figure 17 shows density as a function of mass coordinate at selected times. As the shock (represented by a broad compressional wave) propagates outward, the wavefront becomes less pronounced. When it encounters the sharp density gradient ($t = 2.53$ days), it is at first nearly indistinguishable except as a compression relative to the $t = 0$ curve. The level of the curve as a whole drops with time, representing the expansion of the envelope. As the shock propagates down the gradient, a small density “kink” forms at $M/M_\odot \approx 6.9$; at $t = 6$ days, the inversion involves more mass ($\sim 0.2 M_\odot$) and has grown to a factor $\delta\rho/\rho \approx 1.1$, where $\delta\rho$ is the difference in density between the maximum in the inversion and the local minimum which precedes it in mass coordinate. By

TABLE 6
MODEL B EVOLUTION*

t_6	R	R_{ph}	v_{ph}	v_m	v_R	T_e	T_m	L_t	K	L_{bol}	RT
0.....	9.245	8.777	(3 K)	(3 K)	...	~1.00	5 (28)	..
0.675.....	1.4 (-2)	1.4 (-2)	2. (-2)	0.254	...	2.14 (-6)	0.410	2.3 (40)	6.9 (-6)
0.775.....	4.4 (-2)	4.2	5.7 (-2)	0.337	...	1.50 (-5)	0.410	7.1	1.2 (-5)
0.877.....	8.79	2.3 (3)	1.2 (-1)	0.423	...	4.84	0.399	1.86 (41)	1.6
0.981.....	9.17	3.8 (3)	8.4	0.510	...	1.28 (-4)	0.396	3.70	2.0
1.08.....	9.20	3.0 (2)	4.7 (0)	0.602	...	2.93	0.393	7.26	2.1
1.18.....	9.246	4.5 (0)	8.6	0.798	...	6.50	0.390	2.44 (42)	2.8
1.29.....	9.247	9.20	2.6 (1)	2.5 (1)	1.35	...	2.14 (-3)	0.390	8.6
1.39.....	9.252	9.205	4. (1)	6.0 (1)	1.58	...	6.13	0.390	2.03 (43)
1.49.....	9.261	9.214	9. (1)	1.27 (2)	1.2 (2)	1.78 < 2.5	0.0288	0.393	3.87
1.59.....	9.277	9.23	1.7 (2)	2.24	2.16	1.92 < 2.7	0.0499	0.402	6.17
1.69.....	9.305	9.26	2.9 (2)	3.55	3.44	2.01 < 2.9	0.0764	0.407	3.5
1.79.....	9.348	9.30	4.3	5.10	4.98	2.04	2.9	0.413	4.6
2.04.....	9.439	9.40	6.2	7.50	7.36	2.00	2.8	0.425	6.1
2.14.....	9.521	9.48	8.3	9.01	8.87	1.94	2.6	0.430	9.07 (43)
2.24.....	9.617	9.57	9.6	1.03 (3)	1.02 (3)	1.85	2.4	0.439	6.5
2.64.....	10.099	10.06	1.2 (3)	1.34	1.32	1.44	1.8	0.464	7.68
3.04.....	10.663	10.62	1.42	1.49	1.47	1.16	1.5	0.484	6.9
3.54.....	11.443	11.40	1.56	1.65	1.64	1.01	1.35	0.507	1.45
4.00.....	12.232	12.19	1.72	1.79	1.78	0.934	1.23	0.521	2.53
4.51.....	13.158	13.12	1.82	1.92	1.91	0.875	1.11	0.533	8.13
5.01.....	14.137	14.10	1.96	2.00	1.99	0.821	1.01	0.547	3.61
5.50.....	15.127	15.09	2.02	2.05	2.04	0.772	0.93	0.553	3.73
6.00.....	16.156	16.12	2.05	2.08	2.07	0.733	0.811	0.558	5.75
6.47.....	17.134	17.10	2.08	2.16	2.10	0.694	0.63	0.564	3.75
7.03.....	18.310	18.22	2.00	2.18	2.13	0.669	0.602	0.570	4.72
7.40.....	19.108	18.90	2.19	2.19	2.14	0.646	0.639	0.573	3.77
7.49.....	19.290	19.09	2.11	2.19	2.14	0.638	0.626	0.573	4.42
										4.31	3.78

* Quantities are the same as defined in Table 4 for Model A, with the exception of the last column, RT , which is the estimated total turbulent energy as a fraction of the initial total shock energy. Peak light occurred at $t_6 = t/10^6$ s = 1.89. T_m is not monotonic at late times because of photospheric recession in the (coarse) finite difference zoning.

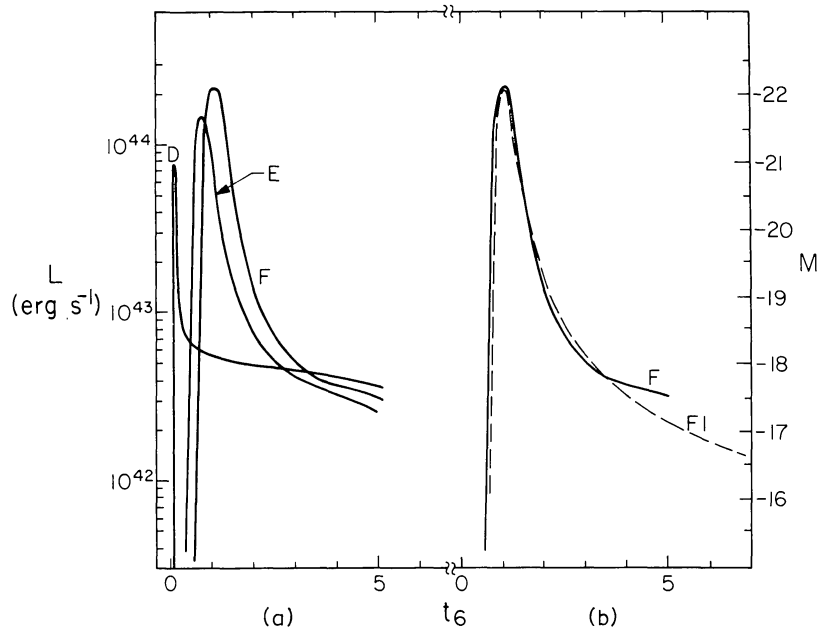


FIG. 15.—(a) Bolometric light curves for the model sequence D, E, and F. The luminosity is given in ergs s $^{-1}$. The curve for model D is similar to that obtained for the other compact model A, having a luminosity spike of duration $\Delta t_6 \lesssim 0.2$ and a subsequent flattening into a postpeak plateau. The introduction of density gradient zones ($\Delta M \approx 1 M_\odot$) in model E shows clearly that an extended gradient region diffusively spreads this pulse into a well-defined peak with width $\Delta t \lesssim 0.9$, acting as the idealized circumstellar shell defined in § II of the text. Addition of such a low-density shell ($\Delta M \approx 0.7 M_\odot$) as well to model F shows the increased radiation efficiency of this configuration, which produces a reasonable bolometric light peak of duration $\sim 1.4 \times 10^6$ s ≈ 16 days. The postpeak flattening in the “shell” models E and F is less marked than that of model D. (b) Bolometric light curves for the models F and F1, which were identical except that $\kappa = \kappa_{es} = \text{constant}$ was used for F1, clearly show the effect of recombination (via the opacity) in holding the postpeak light curve up at long times.

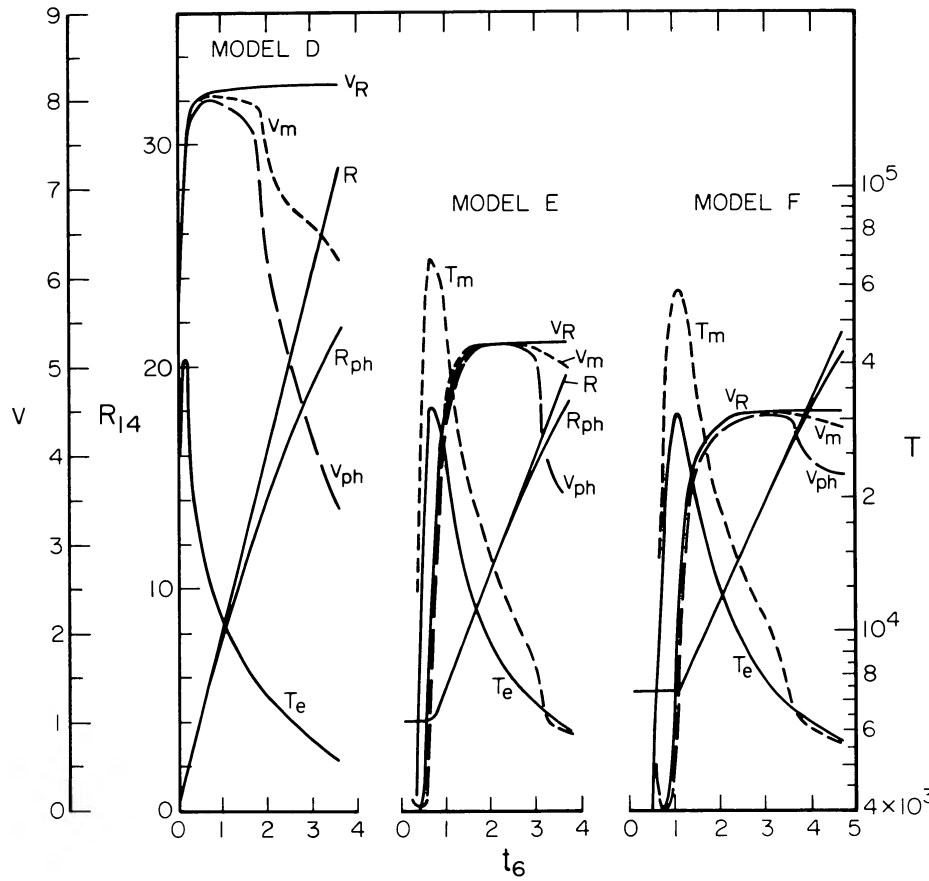


FIG. 16.—Evolution of velocities, radii, and effective temperatures for model sequence D, E, and F. Curves are labeled in notation consistent with that of Figs. 5, 6, and 14. As before, the velocity scale is in units of 10^3 km s^{-1} , radii are given in units $R_{14} \equiv R/10^{14} \text{ cm}$, and the temperature scale (at right) is in kelvins.

TABLE 7
MODEL D EVOLUTION*

t_6	R	R_{ph}	v_{ph}	v_m	v_R	T_e	T_m	L_t	K	L_{bol}
0.....	0.713	0.713				0.079		0	1.00	1.4 (36)
0.153.....	0.986	0.986	7.07 (3)	7.08 (3)	7.074 (3)	4.16	15.8	2.6 (-3)	0.597	2.07 (43)
0.262.....	1.811	1.810	7.56	7.76	7.755	2.43	6.8	3.73	0.745	8.08 (42)
0.372.....	2.677	2.675	7.86	7.92	7.918	1.93	4.5	4.47	0.807	7.09
0.473.....	3.482	3.478	7.95	7.99	7.993	1.67	3.4	5.09	0.842	6.72
0.577.....	4.312	4.303	7.93	8.04	8.038	1.48	2.7	5.71	0.866	6.42
0.682.....	5.159	5.143	8.00	8.06	8.067	1.34	2.2	6.33	0.884	6.12
0.786.....	6.003	5.978	8.03	8.06	8.088	1.23	1.9	6.91	0.897	5.87
0.891.....	6.847	6.810	7.92	8.06	8.103	1.14	1.7	7.48	0.907	5.66
0.995.....	7.692	7.639	7.97	8.03	8.115	1.07	1.5	8.01	0.915	5.43
1.203.....	9.381	9.288	7.93	8.03	8.132	0.951	1.2	9.06	0.928	5.12
1.405.....	11.026	10.879	7.88	8.02	8.144	0.866	1.1	9.99	0.936	4.88
1.708.....	13.493	13.220	7.73	7.98	8.158	0.788	0.90	0.0113 (0)	0.945	4.92
1.909.....	15.135	14.569	6.71	7.84	8.164	0.759	0.69	0.0123	0.950	5.02
2.110.....	16.782	15.068	2.48	7.21	8.166	0.705	0.69	0.0132	0.953	4.95
2.410.....	19.239	16.125	3.52	6.84	8.170	0.658	0.70	0.0146	0.957	4.95
2.796.....	22.390	18.346	5.75	6.69	8.175	0.603	0.58	0.0164	0.961	4.71
3.097.....	24.846	20.015	5.54	6.54	8.178	0.569	0.55	0.0176	0.963	4.60
3.362.....	37.009	21.081	4.02	6.38	8.181	0.537	0.54	0.0187	0.965	4.33
3.547.....	28.523	21.621	2.92	6.19	8.183	0.516	0.50	0.0195	0.966	4.12

* Quantitites are defined as in Table 4, with $t_6 \equiv t/10^6 \text{ s}$. Peak light occurs at $t_6 = 0.153$.

TABLE 8
MODEL E EVOLUTION*

t_6	R	R_{ph}	v_{ph}	v_m	v_R	T_e	T_m	L_t	K	L_{bol}	RT
0.....	4.044	3.985	0.404	0.53	0	1.0	3.1 (37)	0
0.316.....	4.044	4.035	1.58 (2)	0.404	0.53	3.8 (-7)	0.731	3.12 (40)	0
0.417.....	4.044	4.038	3.0 (1)	3.86 (0)	3.76 (0)	0.856	1.9	1.35 (-5)	0.772	6.25 (41)	1.10 (-4)
0.518.....	4.053	4.047	8.9	3.5 (2)	2.97 (2)	1.830	4.1	4.76 (-4)	0.789	1.31 (43)	1.84 (-4)
0.619.....	4.141	4.136	8.81 (2)	1.59 (3)	1.583 (3)	2.775	6.2	0.00424	0.798	7.24 (43)	1.63 (-4)
0.719.....	4.377	4.372	2.36 (3)	3.07	3.064	3.220	7.0	0.0155	0.810	1.47 (44)	2.21 (-4)
0.819.....	4.724	4.719	3.47	3.80	3.795	3.115	6.5	0.0308	0.824	1.50 (44)	2.90
0.920.....	5.134	5.128	4.05	4.31	4.303	2.73	5.5	0.0435	0.836	1.05 (44)	3.62
1.020.....	5.580	5.574	4.46	4.59	4.584	2.34	4.5	0.0519	0.845	6.62 (43)	4.47
1.121.....	6.051	6.044	4.65	4.75	4.740	2.202	3.7	0.0572	0.853	4.36 (43)	5.34
1.221.....	6.530	6.523	4.79	4.86	4.845	1.79	3.2	0.0608	0.860	3.09 (43)	6.21
1.321.....	7.021	7.013	4.90	5.05	4.947	1.60	2.8	0.0635	0.866	2.31 (43)	6.94
1.422.....	7.524	7.516	4.98	5.06	5.054	1.45	2.4	0.0655	0.870	1.80 (43)	7.61
1.522.....	8.035	8.026	5.10	5.15	5.160	1.33	2.1	0.0671	0.874	1.45 (43)	8.23
1.623.....	8.559	8.548	5.17	5.19	5.208	1.24	1.9	0.0684	0.878	1.23 (43)	8.81
1.723.....	9.085	9.071	5.23	5.21	5.223	1.16	1.8	0.0695	0.881	1.05 (43)	9.35
1.823.....	9.610	9.594	5.23	5.22	5.236	1.09	1.6	0.0705	0.883	9.22 (42)	9.76
2.025.....	10.666	10.645	5.23	5.24	5.253	0.972	1.4	0.0721	0.888	7.22 (42)	1.02 (-3)
2.272.....	11.965	11.936	5.23	5.25	5.268	0.861	1.2	0.0737	0.892	5.60 (42)	1.03
2.473.....	13.025	12.988	5.23	5.26	5.276	0.791	1.06	0.0747	0.895	4.73 (42)	1.06
2.674.....	14.088	14.043	5.25	5.26	5.282	0.734	0.96	0.0756	0.897	4.09 (42)	1.09
2.975.....	15.677	15.582	5.11	5.27	5.289	0.700	0.83	0.0768	0.900	4.21 (42)	1.14
3.175.....	16.736	16.418	4.18	5.18	5.290	0.672	0.65	0.0776	0.901	4.06 (42)	1.16
3.430.....	18.085	17.281	3.88	5.08	5.292	0.637	0.64	0.0786	0.903	3.84 (42)	1.17
3.603.....	19.005	17.952	3.88	5.03	5.293	0.613	0.62	0.0792	0.904	3.63 (42)	1.18
3.703.....	19.530	18.340	3.88	4.98	5.293	0.600	0.60	0.0796	0.904	3.53 (42)	1.18

* Quantities are defined as in Table 4, with $t_6 \equiv t/10^6$ s, and RT is defined as the total turbulent energy as a fraction of initial total shock energy. Peak light occurs at $t_6 = 0.819$.

TABLE 9
MODEL F EVOLUTION*

t_6	R	R_{ph}	v_{ph}	v_m	v_R	T_e	T_m	L_t	K	L_{bol}	RT
0.....	5.436	5.373	0.344	0.404	9.3 (-7)	0.776	2.95 (40)	...
0.435....	5.436	5.373	0.463	0.697	6.9 (-6)	0.790	9.63	3.90
0.535....	5.436	5.428	5.00 (2)	7.4 (-3)	7.41 (-3)	0.813	1.64	3.4 (-5)	0.796	9.20 (41)	4.01
0.636....	5.436	5.430	2.0 (1)	1.3 (-1)	1.27 (-1)	0.813	1.64	3.4 (-5)	0.796	9.20 (41)	4.01
0.736....	5.437	5.431	1.0 (1)	2.4 (1)	2.32 (1)	1.46	2.84	4.3 (-4)	0.797	9.47 (42)	4.69
0.837....	5.448	5.443	1.20 (2)	3.10 (2)	2.92 (3)	2.17	4.23	2.86 (-3)	0.796	4.71 (43)	5.64
0.937....	5.513	5.508	6.50	1.08 (3)	1.065 (3)	2.78	5.39	0.0113	0.793	1.30 (44)	6.69
1.037....	5.669	5.665	1.570 (3)	2.06	2.053	3.09	5.91	0.0284	0.793	2.10 (44)	7.64
1.137....	5.921	5.916	2.510	2.93	2.916	3.06	5.72	0.0503	0.797	2.18 (44)	8.55
1.324....	6.557	6.552	3.401	3.75	3.746	2.49	4.43	0.0817	0.808	1.17 (44)	9.52
1.525....	7.345	7.340	3.920	4.08	4.073	1.92	3.24	0.0973	0.819	5.17 (43)	1.16 (-3)
1.725....	8.175	8.170	4.150	4.21	4.200	1.55	2.49	0.1048	0.827	2.76 (43)	1.35
1.971....	9.220	9.216	4.252	4.30	4.294	1.27	1.95	0.1099	0.835	1.58 (43)	1.49
2.171....	10.095	10.090	4.370	4.43	4.426	1.12	1.68	0.1125	0.839	1.14 (43)	1.64
2.362....	10.940	10.933	4.414	4.45	4.448	1.02	1.49	0.1144	0.843	9.05 (42)	1.7
2.562....	11.832	11.823	4.450	4.47	4.465	0.929	1.32	0.1160	0.845	7.44 (42)	1.90
2.762....	12.728	12.718	4.475	4.48	4.478	0.860	1.19	0.1174	0.849	6.32 (42)	2.02
2.948....	13.561	13.548	4.462	4.48	4.487	0.806	1.08	0.1185	0.851	5.52 (42)	2.13
3.148....	14.460	14.444	4.480	4.49	4.494	0.753	0.979	0.1195	0.853	4.80 (42)	2.22
3.349....	15.361	15.339	4.453	4.49	4.500	0.724	0.877	0.1204	0.855	4.62 (42)	2.30
3.523....	16.145	16.107	4.414	4.49	4.502	0.694	0.671	0.1212	0.856	4.32 (42)	2.36
3.723....	17.047	16.931	4.120	4.48	4.504	0.670	0.621	0.1220	0.857	4.17 (42)	2.42
3.923....	17.949	17.720	3.945	4.44	4.506	0.645	0.615	0.1228	0.858	3.96 (42)	2.48
4.107....	18.779	18.446	3.946	4.42	4.507	0.622	0.607	0.1235	0.859	3.75 (42)	2.54
4.308....	19.681	19.195	3.726	4.38	4.508	0.600	0.594	0.1243	0.860	3.59 (42)	2.60
4.498....	20.540	19.936	3.900	4.37	4.509	0.580	0.570	0.1249	0.861	3.41 (42)	2.66
4.708....	21.485	20.741	3.833	4.34	4.510	0.560	0.562	0.1256	0.861	3.24 (42)	2.72

* Quantities are defined as in Table 4, with $t_6 \equiv t/10^6$ s, and RT is defined as the total turbulent energy as a fraction of initial total shock energy. Peak light occurs at $t_6 = 1.137$.

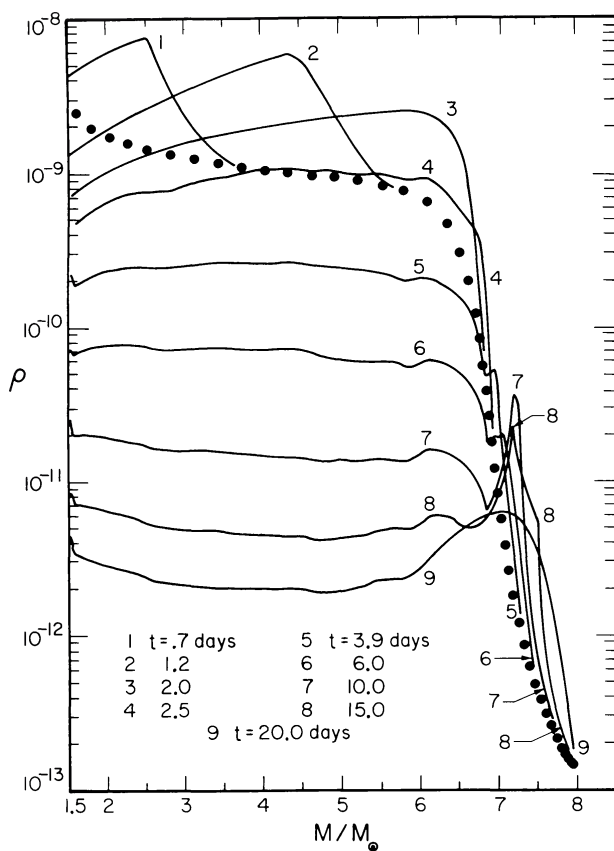


FIG. 17.—Evolution of mass-coordinate density profiles at various times for model C. The filled circles show the initial density configuration for the model. The development of a density inversion is evident by $t = 3.9$ days (curve 5), growing rapidly until $t \approx 10$ days (curve 7), when the method of momentum transport and smoothing outlined in Appendix C was able to smear the inversion out over the outer $2 M_\odot$. This region is considered to have high- and low-density blobs and fingers as a result of a Rayleigh-Taylor fluid instability. For comparison of the effect, an unsmoothed model of similar configuration is shown in Fig. 19.

$t = 10$ days, the inversion is pronounced ($\delta\rho/\rho \gtrsim 6$), with its maximum at $M/M_\odot \approx 7.2$, and involves some $0.5 M_\odot$. In contrast with the cases shown in Figures 18 and 19, which represent the density profile evolution for models D, E, and F, respectively, this inversion spreads out through an increasing amount of mass and simultaneously declines in magnitude. At $t = 15$ days, the inversion is still pronounced and is stationary in mass coordinates, now involving $0.7 M_\odot$ with $\delta\rho/\rho \approx 4.0$. This behavior continues, until by $t = 20$ days the inversion involves some $1.7 M_\odot$ (still approximately stationary in mass coordinates) and has $\delta\rho/\rho \approx 3.0$. Figure 20 shows density versus radius for this same example.

The onset of the inversion is coincident in time and mass coordinate with the development (in the gradient) of a “diffusion wave.” This is shown in Figure 21, which is a plot of $\beta \equiv P_{\text{rad}}/P_{\text{tot}}$ as a function of time. The position of the pseudoviscous shock is also indicated. Until $t \approx 2$ days the shock is well defined;

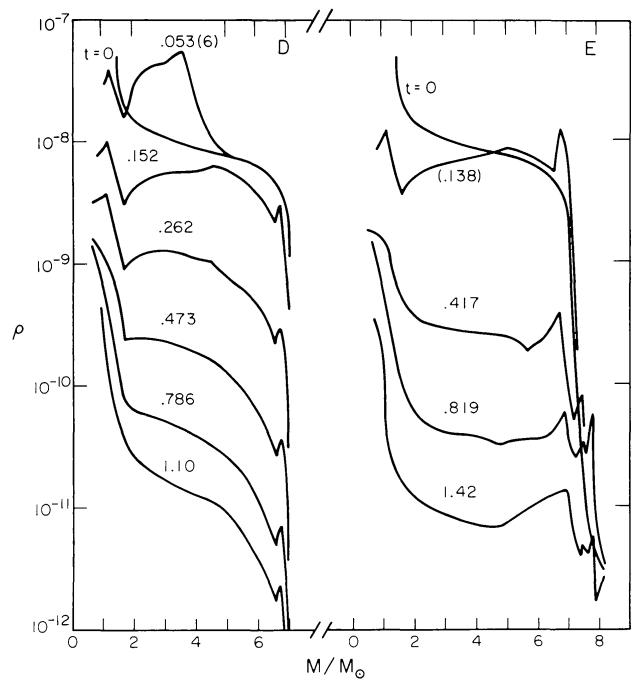


FIG. 18.—Density profiles for models D and E show the development of density inversions as the shock compression encounters the steep outer density gradient. As was the case for model A, the expansion of the compact model D is quasi-homologous, and results in the preservation of an approximately constant postshock profile. In contrast, the expansion of semiextended model E results in a complex structure of density inversions in the outer mass layers. Times shown are in units of $t_6 \equiv t/10^6$ s.

outside the shock front $\beta \lesssim 0.4$, with slightly higher values to the outside resulting from the initial outward density decrease; behind the shock $\beta \approx 1$. This simply reflects the result that in a strongly shocked tenuous gas the energy density is dominated by the radiation field.

However, by $t \approx 3.8$ days the material ahead of the pseudoviscous shock has already shown some heating, and β has increased markedly in this region ($M/M_\odot \approx 7.2$). This process continues, until by $t \approx 6$ days β is everywhere greater than 0.9, even though the pseudoviscous shock front lies at $M/M_\odot \approx 7.35$. The pseudoviscous shock gives way to a diffusion wave when the front reaches densities low enough that the radiative diffusion time scales are much shorter than typical Courant times. This transition is similar to the “heat tongue” reported by Grasberg, Imsheenik, and Nadyozhin (1971), but is a much more pronounced effect than seen in their models. Figure 22 shows plots of $T(r)$ at selected times, illustrating the magnitude of this effect.

ii) Fluid Instability

The net result of this transition is to degrade the pseudoviscous shock. The development of the local compression is enhanced by the radiative energy leakage across the shock front. As this compression grows due to the presence of high-velocity material interior to the affected region, the matter is heated and

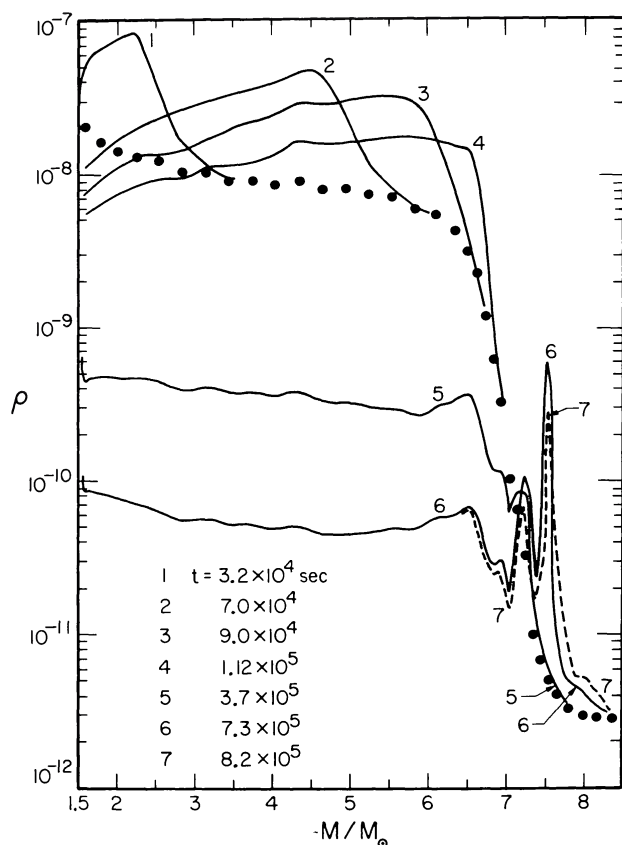


FIG. 19.—Density profiles for the extended model F clearly show the development of multi-inversion density structure in the low-density ($\rho \lesssim 2-3 \times 10^{-11} \text{ g cm}^{-3}$) portions of the density gradient and shell. Some pseudoviscous smoothing has been introduced, in order to prevent density contrasts of order 10^3 or larger. This smoothing is, however, nowhere near as great as produced by the computational method of Appendix C (cf. Fig. 17 for contrast), and clearly does not eliminate the complexities of the postshock structure typical of extended, unsmoothed models. As before, the solid circles show the density profile at $t = 0$.

in turn can radiate a sizable fraction of its energy. The gas pressure does not increase rapidly enough to offset the compressional effects of the expanding interior matter, and $\delta\rho/\rho$ can increase to large values (up to $\sim 10^4$). This matter is then, however, subject to the fluid Rayleigh-Taylor instability. The density inversion is unstable with respect to the interpenetration of the two density phases. Such an instability is transient, growing for as long as the conditions requisite for growth are present.

The inability of the gas to overcome the compressional density inversion by exerting sufficient mechanical pressure suggested the appropriateness of estimating the kinetic momentum transfer and turbulent pressure. Two ad hoc procedures were employed to treat the behavior of the inversion. First, a method for estimating the momentum transfer at a given mass plate was employed (and is discussed fully in Appendix C). It conserves total energy and provides a crude estimate of the energy lost from the bulk flow due to the presence of "turbulence." From this

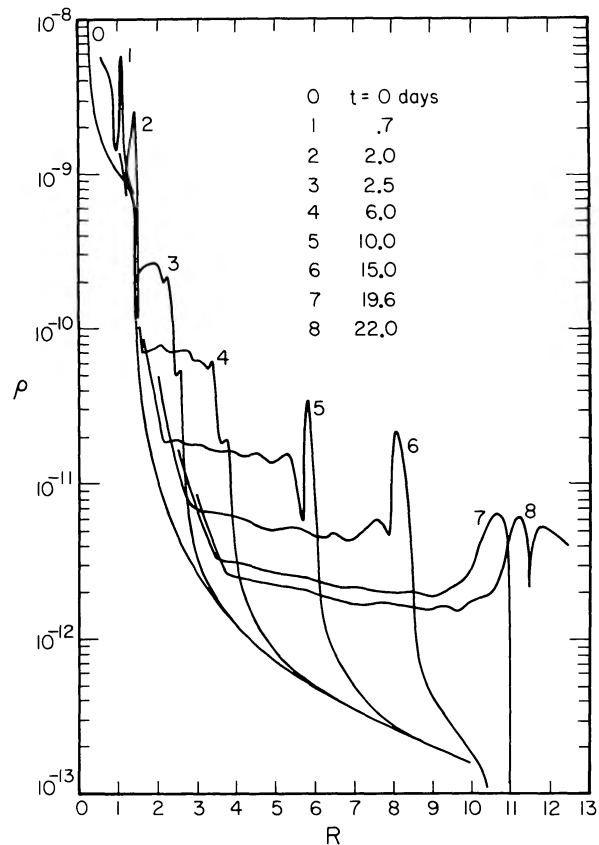


FIG. 20.—Density profiles for model C as a function of radial coordinate clearly show the development of thin shell-like density inversions during the peak epoch. Some smoothing is apparent by $t = 10$ days (curve 5). The spreading in mass and radius of the inversion continues but is insufficient to disperse the dominant shell structure, which by time ~ 20 days has extent $\Delta r \approx 10^{14} \text{ cm}$ and involves almost $2 M_\odot$ (cf. Fig. 17). The formation of such a configuration is apparently a signature of extended models, even assuming a relatively efficient smoothing/mixing treatment.

estimate, values for the random velocities due to this (assumed isotropic) turbulence may be calculated. Second, a method for combining mass zones in the region of the inversion was incorporated, under the constraint of conserving momentum and kinetic energy of the mass plates involved (at zone boundaries) and the internal energy (including radiation) of the zones involved. Such an approach is justified by recognition of the probable mixing of mass due to any large-scale turbulence. The combination of these two treatments is responsible for smoothing the density inversion (Fig. 17), and prevents it from reaching the proportions reported by Grasberg, Imshennik, and Nadyozhin (1971) and FA (similar to that shown in Fig. 19). The smoothing is a computational necessity; a "smoothed" zone is considered to contain both high- and low-density phases. Such an instability tends to preclude the formation of thin shell-like structures in the outer regions of the envelope, as suggested by Grasberg, Imshennik, and Nadyozhin. We would expect "blobs" and "filaments" instead.

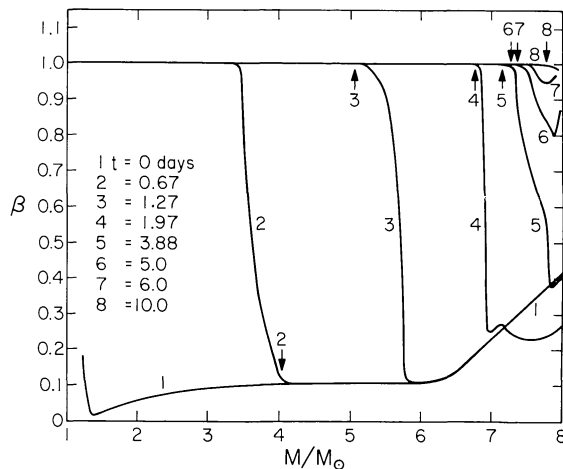


FIG. 21.—Radiation factor $\beta \equiv P_{\text{rad}}/P_{\text{tot}}$ as a function of mass for model C at various times. The position of the pseudoviscous shock front is marked by vertical arrows for each time. As the shock propagates into low-density material ($\rho \leq 2-3 \times 10^{-11} \text{ g cm}^{-3}$), radiation diffuses well out ahead of the pseudoviscous shock and provides the dominant momentum transfer in the outer mass layers.

iii) Light Peak

The light curve for this model is depicted in Figure 23; the solid line is the total (bolometric) luminosity. The radiation front reaches the surface at $t \approx 7$ days, causing rapid heating and the subsequent rise to peak luminosity ($L_{\text{bol}} = 3.3 \times 10^{44} \text{ ergs s}^{-1}$) at $t \approx 14$ days. The decline from peak is gradual, due to the relatively low shell velocities, declining to $L_{\text{bol}} \approx 3 \times 10^{43} \text{ ergs s}^{-1}$ (2.5 magnitudes) in about 12 days. Total bolometric luminosity in the peak is $\int L_b(t) dt \approx 2 \times 10^{50} \text{ ergs}$. The “visual” light curve declines only 1 magnitude in this same period, in part reflecting the low material velocities in the relatively massive gradient and shell;

TABLE 10
MODEL C*

t (days)	T_e (K)	λ_{max}	$U - B$	$B - V$
1.27.....	1.37 (3)	2.1 (4)
5.0.....	4.17	6950	+0.26	+1.07
6.0.....	5.63	5150	-0.16	+0.68
7.0.....	7.24	4000	-0.44	+0.43
8.1.....	1.15 (4)	2520	-0.79	+0.11
9.0.....	1.55	1870	-0.95	-0.03
10.0.....	1.93	1500	-1.03	-0.11
11.0.....	2.21	1310	-1.08	-0.16
13.5.....	2.56	1130	-1.12	-0.19
14.2.....	2.565	1130	-1.12+	-0.19+
15.5.....	2.487	1165	-1.11	-0.19
17.0.....	2.26	1280	-1.08	-0.16
19.0.....	1.86	1560	-1.02	-0.10
21.0.....	1.57	1845	-0.95	-0.04
21.6.....	1.48	1960	-0.92	-0.015

* Values of the wavelength λ_{max} (in angstroms) corresponding to the peak intensities for a blackbody radiating at temperature T_e . Times are given in days, and the values of T_e listed are the effective temperatures for the extended Model C. Values of $U - B$ and $B - V$ are only approximate; they are derived on the assumption of blackbody radiation at temperature T_e (cf. Appendix D).

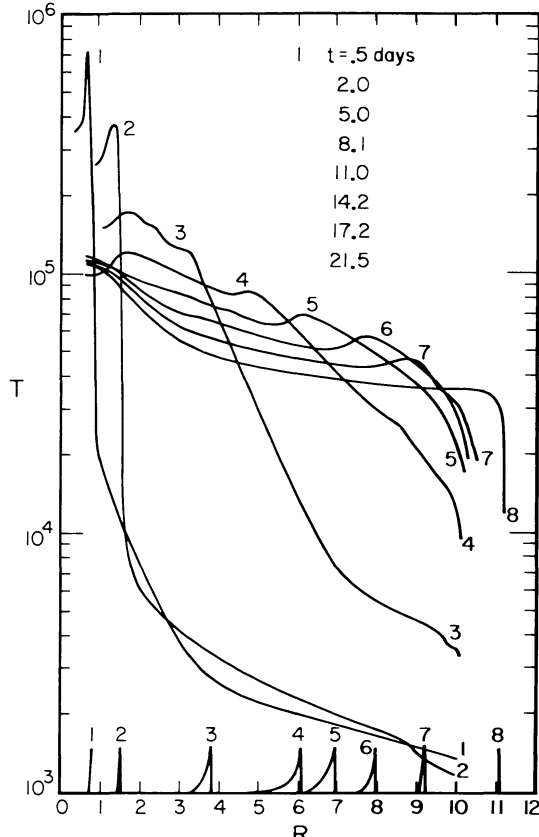


FIG. 22.—Material temperature structures $T(r)$ at selected times for model C. The position and approximate sharpness of the pseudoviscous shock is also shown at each time for reference to the temperature curves. The eight times shown correspond to the eight numbered profile curves. Notice that by $t \approx 5$ days (curve 3) significant radiative heating has taken place well ahead of the pseudoviscous shock front; the effect continues as the transition from shock wave to diffusion wave continues in the low-density medium. By $t \approx 17$ days (curve 7) the preshock heating has raised the local sound speed sufficiently for the shock front to begin to catch up with the diffusion heating; by $t \approx 21.5$ days (curve 8) they are approximately coincident (i.e., both are near the outer mass boundary).

lower masses would yield higher velocities, enhancing adiabatic cooling and increasing the sharpness and magnitude of the postpeak luminosity decline. It is not likely, as Bodenheimer and Ostriker (1974) suggest, that grain material present in the shell would have a large effect upon the light curve, since any such material is likely to be radiatively evaporated during the onset of light maximum (Falk and Scalo 1975).

Shown also in Figure 23 are the numerically calculated “frequency bin” luminosities. The light peak is clearly dominated by radiation shortward of the “visual” band, which falls off more rapidly after peak light than do the two bands to the longward. The relative magnitudes of these frequency bin luminosities give a rough indication of the reddening effects of envelope expansion and cooling. Table 10 gives values of the effective temperature T_e and the wavelength λ_{max} for which Wein’s law predicts the maximum blackbody intensity. The effective temperature reaches

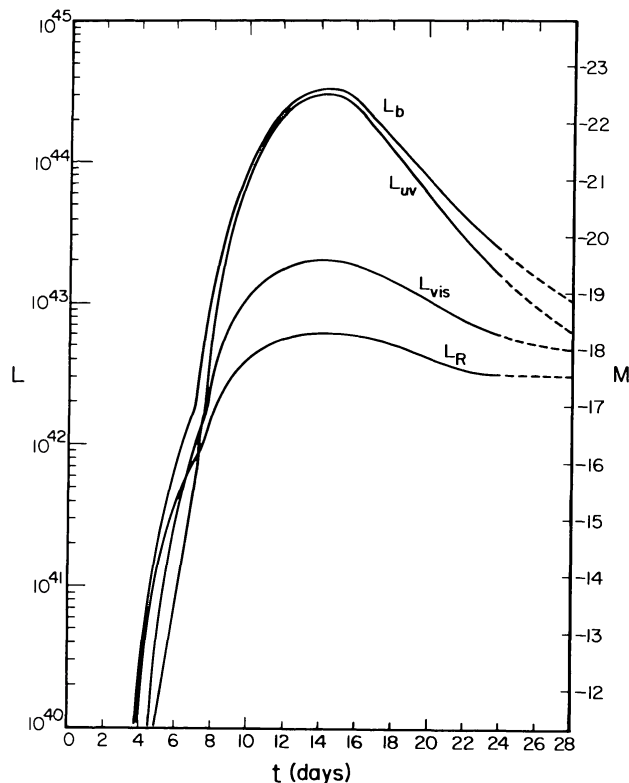


FIG. 23.—Luminosity curves for the peak epoch Model C. The bolometric light curve is labeled L_b , and exhibits the broad peak characteristic of extended models, here with $\Delta t_{\text{peak}} \gtrsim 16$ days. The curves labeled L_{uv} , L_{vis} , and L_R are the calculated continuum luminosities for energy bands with wavelengths $\lambda < 4000 \text{ \AA}$, $4000 \leq \lambda \leq 7000 \text{ \AA}$, and $\lambda > 7000 \text{ \AA}$, respectively. The peak epoch is clearly dominated by (near) ultraviolet frequencies, giving way to “visual” frequencies as reddening increases in the expanding and cooling matter. The luminosity is in ergs s^{-1} ; an absolute magnitude scale is given on the right. The calculation was halted at $t \approx 24$ days; the broken lines are extrapolations of the various curves to emphasize reddening effects.

a peak $T_e \approx 2.56 \times 10^4 \text{ K}$ at $t \approx 14$ days and declines to $T_e \approx 1.3 \times 10^4 \text{ K}$ 10 days later.

iv) Material Kinetics

Figure 24 shows the matter velocity versus mass coordinate at selected times. The acceleration of the outer 0.2 to $0.5 M_\odot$ region is affected chiefly by radiation pressure, at least in the early epoch of the light curve, and takes place on a time scale of order $t_{\text{acc}}^{-1} \approx (\partial \ln \rho / \partial t) \approx L_b(4\pi r^2 v c)^{-1} \approx (4.3 \text{ days})^{-1}$. The early velocities in these outer layers (chiefly the low-density shell) are moderate ($v \approx 4500 \text{ km s}^{-1}$), and are relatively constant throughout the outer mass layers. The kinetic energy of the envelope alone (i.e., to $M/M_\odot \approx 6.5$) accounts for almost 75% of the total initial energy by $t = 22$ days. The outer layers thus represent only a small fraction of the total energy of the expanding envelope. The bulk of the envelope expands homologously with a very nearly constant velocity profile. Smaller masses and a steeper slope in the higher density portions of the gradient would

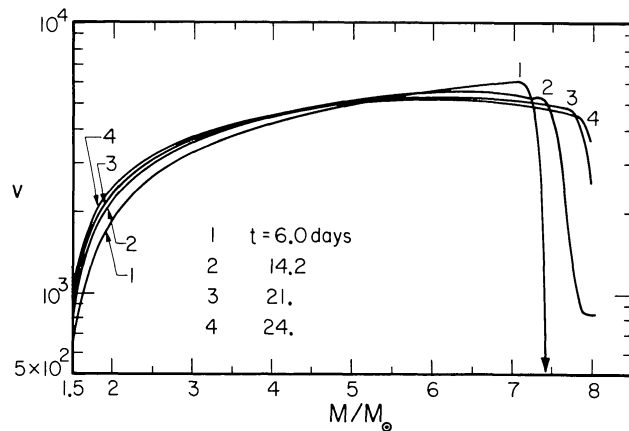


FIG. 24.—Model C velocity profiles at various times. Velocities (km s^{-1}) as functions of mass coordinate are shown at prepeak ($t = 6$ days), peak ($t = 14.2$ days), and postpeak times. The resulting profiles are flat in the outer mass zones, a result typical of extended configurations where low densities result in diffusion-wave behavior and acceleration by increasingly diluted radiation pressures. Notice the decrease of material velocities at later times for $M \gtrsim 6$ or so.

be in better agreement with envelope integrations and would provide for higher velocities in these regions. Correspondingly smaller masses invested in the low-density region would also result in smaller (inertial) back pressure on the expanding matter interior to it, and the final velocity profile might therefore be expected to reach higher maximum velocities.

Tables 11 and 12 summarize the behavior of the principal quantities of interest for model C. Table 11 gives the evolution of various velocities, radii, and energies, while Table 12 details the development of the luminosity peak and associated energetics.

e) Discussion

It has been indicated previously that there seems to be no hard evidence for Type II supernovae having the initial luminosity peak (lasting 10–20 days) which is characteristic of Type I supernovae. If not, the shock wave model merely requires “ordinary” red supergiant envelopes ($R \approx 3 \times 10^{13}\text{--}10^{14} \text{ cm}$) to satisfactorily fit the observations (see Arnett and Falk 1976). If such visual peaks do exist for some SN II, our calculations suggest that the bolometric light curve should have a similar shape. This seems to require the presence of an extended circumstellar shell ($R \approx 10^{15} \text{ cm}$). In the absence of an answer to this observational question we have examined both possibilities.

i) Shell Parameters and Mass Loss

The essential feature of the extended models is the circumstellar shell. There is a general trend for massive stars to evolve to configurations (red supergiants) in which mass loss is observed. Mass-loss processes are not well understood, and there seem to be no convincing arguments against the existence of such shells. In fact in some cases (Gehrz and Woolf 1971; Low *et al.*

TABLE 11
MODEL C PHYSICAL EVOLUTION*

t_6	R	R_{ph}	v_{ph}	v_m	v_{max}	K	TE	$v_{t,max}$	R_{sh}	$v_{m,sh}$
0.....	1.0042	0.892	1.50 (4)	1.667
0.064.....	6.33 (3)	0.928	0.09	1.4 (3)
0.170.....	4.82	0.710	0.144	3.3
0.336.....	1.0043	6. (-4)	6.22	1.027	8.3 (43)	9.3 (0)	0.274	3.4
0.390.....	5. (-3)	6.20	1.079	1.7 (44)	1.1 (1)	0.312	3.6
0.444.....	1.8 (-2)	6.17	1.117	1.7	1.1	0.354	3.6
0.484.....	3.8	6.14	1.140	1.7	1.1	0.392	3.6
0.529.....	8.3	6.10	1.160	1.7	1.1	0.41	3.5
0.562.....	...	0.91982	5.0 (2)	1.7 (-1)	6.07	1.173	9.4	3.1	0.44	3.4
0.609.....	...	0.95816	8.2 (3)	3.6	6.00	1.189	9.4 (45)	1.2 (2)	0.49	2.6
0.682.....	...	0.99216	4.7	2.7 (0)	5.94	1.208	2.1 (46)	1.6	0.54	2.5
0.756.....	1.0044	0.99118	-1.3 (2)	1.7 (1)	5.88	1.223	4.1	1.8	0.59	2.4
0.916.....	1.0056	0.99143	1.7 (1)	1.4 (2)	5.79	1.244	1.3 (47)	2.6	0.70	2.1
1.031.....	1.0083	0.99401	2.2 (2)	3.4	5.71	1.254	1.6	2.8	0.77	2.0
1.122.....	1.0124	0.99804	4.4 (1)	5.7	5.67	1.259	1.6	2.8	0.82	2.0
1.228.....	1.0201	1.0055	7.0 (2)	8.8	5.63	1.264	2.1	2.3	0.87	2.0
1.300.....	1.0271	1.0125	9.7	1.1 (3)	5.59	1.267	2.7	1.6	0.91	2.0
1.392.....	1.0368	1.0221	1.0 (3)	1.3	5.55	1.270	3.6	2.0	0.96	2.0
1.470.....	1.0489	1.0343	1.59	1.5	5.53	1.272	4.6	2.4	1.01	2.0
1.566.....	1.0636	1.0495	1.60	1.7	5.49	1.275	6.9	2.7	1.04	2.1
1.641.....	1.0760	1.0630	1.8	1.9	5.44	1.277	9.4	2.1	1.06	2.2
1.735.....	1.0919	1.0829	2.1	2.5	5.37	1.279	1.24 (48)	1.9	1.09	2.4
1.812.....	1.1067	1.1045	2.8	3.2	5.35	1.281	1.37	3.7	~1.10	3.0
1.869.....	1.1251	1.1247	3.5	3.9	5.34	1.283	1.49	5.2	~1.12	4.0

* Notation is consistent with that of previous tables, with the addition of values of estimated "turbulent" energies (TE) and velocities v_t . R_{sh} is the pseudoviscous shock position, and $v_{m,sh}$ is the value of material velocity (in units of 10^3 km s^{-1}) immediately behind the shock front. The radii are given in units of $R_{15} \equiv R/10^{15} \text{ cm}$, velocities in km s^{-1} , temperatures in units of 10^4 K , energies in ergs (K in units of 10^{51} ergs). Numbers in parentheses denote powers of 10. The average photospheric velocity v_{ph} does not behave smoothly initially because of the increase and subsequent decrease in the opacity as the material is heated to temperatures $\gtrsim 10^4 \text{ K}$, and because of interpolation errors resulting from the transition of R_{ph} from one finite-difference mass zone to another. The values v_{max} correspond, not to the velocity of the outer mass point, but to the maximum velocity for all mass points.

TABLE 12
MODEL C LUMINOSITY EVOLUTION*

t_6	L_{bol}	M_{bol}	T_e	L_{uv}	L_{vis}	L_{IR}	$\int L dt$	M_{vis}
0.....	2.29 (40)	-12.20	0.238	2.8 (36)	1.8 (38)	2.3 (40)	3.75 (44)	...
0.064.....	3.10 (39)	-10.03	0.147
0.170.....	2.80	-9.92	0.140	3.04 (35)	2.83 (36)	2.80 (39)	6.56	...
0.336.....	1.57 (40)	-11.79	0.216	1.05 (37)	4.26 (38)	1.53 (40)	1.36 (45)	...
0.390.....	9.28	-13.72	0.337	1.12 (39)	1.35 (40)	7.82	3.92	...
0.444.....	2.71 (41)	-14.88	0.441	1.40 (40)	7.23	1.85 (41)	1.33 (46)	-13.45
0.484.....	4.69	-15.48	0.505	4.13	1.50 (41)	2.77	2.76	-14.24
0.529.....	7.92	-16.05	0.576	1.09 (41)	2.84	3.99	5.57	-14.93
0.562.....	1.20 (42)	-16.50	0.640	2.13	4.54	5.38	8.89	-15.44
0.609.....	2.08	-17.10	0.734	5.23	8.02	7.55	1.63 (47)	-16.06
0.682.....	8.61	-18.64	1.046	4.42 (42)	2.67 (42)	1.52 (42)	4.81	-17.37
0.756.....	3.08 (43)	-20.02	1.439	2.20 (43)	6.19	2.66	1.83 (48)	-18.30
0.916.....	1.41 (44)	-21.67	2.102	1.22 (44)	1.37 (43)	4.71	1.46 (49)	-19.14
1.031.....	2.40	-22.25	2.400	2.17	1.74	5.65	3.64	-19.40
1.122.....	2.98	-22.49	2.526	2.72	1.91	6.10	6.11	-19.50
1.228.....	3.21	-22.57	2.565	2.95	1.99	6.32	9.43	-19.55
1.300.....	3.07	-22.52	2.529	2.81	1.97	6.30	1.17 (50)	-19.54
1.382.....	2.67	-22.37	2.429	2.42	1.88	6.11	1.41	-19.49
1.470.....	2.03	-22.07	2.257	1.81	1.70	5.68	1.62	-19.38
1.566.....	1.36	-21.64	2.028	1.17	1.44	5.06	1.78	-19.19
1.641.....	9.94 (43)	-21.29	1.863	8.28 (43)	1.22	4.45	1.87	-19.02
1.735.....	6.91	-20.90	1.689	5.48	1.03	3.98	1.94	-18.83
1.812.....	5.40	-20.63	1.577	4.12	9.13 (42)	3.68	1.99	-18.70
1.869.....	4.33	-20.39	1.480	3.14	8.32	3.51	2.02	-18.60

* Quantities tabulated include bolometric luminosity L_{bol} (ergs s^{-1}), and the corresponding absolute magnitude M_{bol} , effective temperature T_e (10^4 K), and calculated band luminosities L_{uv} ($\lambda < 4000 \text{ \AA}$), L_{vis} ($4000 \leq \lambda \leq 7000 \text{ \AA}$), and L_{IR} ($\lambda > 7000 \text{ \AA}$). The magnitude M_{vis} results from the "visual" band luminosity L_{vis} . The eighth column lists the total integrated luminosity, $\int L_{bol} dt$.

1970; Wilson, Barrett, and Moran 1970) there is evidence for shells of the type required.

Assuming that electron scattering opacities dominate the peak epoch, electron scattering optical depths of order $\tau \approx 100$ are implied by observed luminosity peak widths of 10–20 days, for shell radii $R_s \approx \Delta R_s \approx 10^{15}$ cm, where ΔR_s is the characteristic extent of the shell. For a given density distribution, this relation ($t_p \approx t_{a,\text{shell}}$) effectively sets a mass requirement on the shell. If we consider presupernova mass loss at a constant rate and velocity, a $\rho \propto r^{-2}$ distribution results. In this case, envelope radii in the supergiant range, $R_e \approx 5 \times 10^{13}$ to 1×10^{14} cm, imply

$$\rho_e \approx \tau_s/\kappa_{es} R_e \approx 3\text{--}6 \times 10^{-12} \text{ g cm}^{-3}.$$

A constant-density distribution suggests only slightly smaller values:

$$\rho_e \approx \tau_s/\kappa_{es} R_s \approx 1.5\text{--}6.0 \times 10^{-13} \text{ g cm}^{-3}$$

for the shell. Typical shell masses for these cases are

$$M_s(\rho \propto r^{-2}) \approx 4\pi R_e^2 \rho_e \Delta R_s \approx 0.04\text{--}0.2 M_\odot$$

and

$$M_s(\rho \approx \text{const}) \approx \frac{4\pi}{3} R_s^3 \rho_e \approx 0.15\text{--}0.31 M_\odot.$$

If we consider mass flow velocities of the order of those inferred for M supergiants, $v \approx 10\text{--}100 \text{ km s}^{-1}$, then shell radii of order 10^{15} cm imply effective presupernova mass loss over a period $0.3\text{--}1.0 \times 10^9 \text{ s} \approx 30 \text{ yr}$ at rates

$$\dot{M} \approx 4\pi R_e^2 \rho_e v_e \approx 0.02 M_\odot \text{ yr}.$$

These rates are high in comparison with observed rates $\dot{M} \lesssim 10^{-5} M_\odot \text{ yr}^{-1}$ and suggest that the extended models require a considerably larger mass-loss rate immediately prior to explosion. Alternatively, some mechanism may operate which serves to pile up material very near to the presupernova star. In this context it is worth pointing out that while the rates

of mass loss prior to disruption would have to be high, the total mass in the presupernova shell is not overly large; mass loss at observed rates over giant lifetimes of order $10^{4\text{--}5}$ yr imply similar masses. The situation is not necessarily this extreme in any case, since the matter in the outer density gradient between envelope and shell contributes to the formation of the light peak (cf. model E).

ii) Energetics

Initial explosion energies E_0 were chosen to yield interesting cases. Adequate energies lie typically in the range $3 \times 10^{50} \lesssim E_0 \lesssim 3 \times 10^{51}$ ergs, as in FA. Subsequent energy partition into radiation (reflected in part by the magnitude of $\int L dt$) or kinetic energy of expansion K depends upon the particular pre-explosion model assumed. Table 13 summarizes values of $\int L dt/E_0$ and K/E_0 for the models considered here. The extended models are significantly more efficient than the compact configurations in producing radiation, differing predominantly in the peak epoch. Extended model radiative efficiencies are typically 10–30%, compared with only 1–2% for compact models like model A.

Energy requirements for these models are modest: in the case of model B, for example, some 3×10^{50} ergs are necessary. This is roughly equivalent to burning about $0.3 M_\odot$ of ^{12}C or ^{16}O to ^{56}Ni . Model C is more energetic, $E_0 \lesssim 2 \times 10^{51}$ ergs, comparable to about $2 M_\odot$ of ^{12}C or ^{16}O burning. (While it is not yet adequately tested, it appears that the total radiative output is proportional to the explosion energy [Arnett and Falk 1976].) It is interesting to note that the gravitational binding energy of a $1.4 M_\odot$ neutron star is of order 2×10^{53} ergs; a collapse to such a configuration in the presence of a suitable coupling to the stellar envelope (e.g., magnetic field, neutrino transport) is a potential source of great energy (cf. Ostriker and Gunn 1971; Colgate and White 1966). In this context it is appropriate to emphasize that there is no need to invoke a source of continuous energy for the expanding envelope, as supposed by Ostriker and Gunn (1971) and by Bodenheimer and Ostriker (1974).

TABLE 13
SUMMARY OF MODEL ENERGETICS*

Model	E_0	ΔL_p^*	ΔL^*	K	L_{\max}	Δt_{peak}	v_{\max}
A.....	0.937	1.32	5.58	8.79	$\gtrsim 7.3$ (43)	0.2	5.22
A1.....	0.937	2.44	(3.18)	8.13	5.4 (44)	0.25	6.26
B.....	0.352	10.6	13.0	2.01	1.08 (44)	1.7	2.20
C.....	1.67	2.02	..	12.8	3.21 (44)	~ 1.3	~ 3.9
D.....	0.998	0.446	1.95	9.64	$\gtrsim 2.1$ (43)	0.13	8.18
E.....	0.998	7.32	7.94	9.02	1.5 (44)	0.9	5.29
F.....	0.998	11.9	12.5	8.59	2.2 (44)	1.3	4.51
F1.....	0.998	11.4	12.5	8.83	2.1 (44)	1.3	4.73

* Shows initial shock energies $E_0 \equiv E/10^{51}$ ergs, total integrated peak luminosity $\Delta L_p^* \equiv \int_{\text{peak}} L_{\text{bol}}(t) dt / 10^{49}$ ergs, integrated total luminosity over the calculated epoch $\Delta L^* \equiv \int_0^{\Delta t_{\text{peak}}} L_{\text{bol}}(t) dt / 10^{49}$ ergs, final kinetic energy of expansion $K_f \equiv K/10^{50}$ ergs, maximum peak luminosity L_p (ergs s^{-1}), approximate peak width $\Delta t_p \equiv \Delta t/10^6 \text{ s}$, and the maximum material velocity of outer layers for each model, $v_{\max} \equiv v/10^3 \text{ km s}^{-1}$. Notice the higher radiative efficiencies of the extended models (B, C, E, F, F1) relative to the compact models (A, A1, D), with resultingly smaller kinetic energies.

Neither is the presence of large amounts of radioactive nuclei needed to account for any quasi-exponential character in the postpeak plateaus of SN II.

Bolometric corrections, especially in the light peaks of extended models, are expected to be large, $\Delta M_{\text{bc}} \approx 2.0$ to 2.5 mag. Similar values occur for compact models. This means that the "unobserved" energy from supernovae in the first 100 days or so is a factor of from 3 to 10 larger than typically observed values, exclusive of the kinetic energy. Total bolometric radiation from the extended models considered is of order of 8×10^{49} ergs (model E) to about 1.3×10^{50} ergs (models B and F). The compact models, A and D, radiate only about 3.0×10^{49} ergs and 2×10^{49} ergs in roughly corresponding times. Postpeak reddening is predicted by both types of model, and can be simply interpreted as monotonic cooling of the emitting medium.

Model C indicates a luminosity of almost 2×10^{50} ergs shortward of the visual wavelengths, with much of this energy radiated in the region $1000 \leq \lambda \leq 2000 \text{ \AA}$ (cf. Table 10). This is smaller by almost two orders of magnitude than the ultraviolet flux required by the model of Morrison and Sartori (1969a, b). In addition, effects of reddening due to nonconservative scattering and a nongray atmosphere have been neglected. Models B, E, and F show a similar behavior in $T_e(t)$, though maximum luminosities and temperatures are somewhat smaller than those for model C. It therefore seems likely that their original SN I model is too energetically inefficient to comprise a satisfactory explanation for supernova light curves.

Due to the low density of the circumstellar shell and the tendency for the pseudoviscous shock to become a diffusion wave as it nears the photosphere, it seems likely that these models are not prolific sources of X-rays. Material temperatures remain too low ($T \lesssim 3 \times 10^4 \text{ K}$) to account for appreciable flux in the range $0.1 \leq \lambda \leq 100 \text{ \AA}$; temperatures of order $3 \times 10^8 \geq T \geq 3 \times 10^5 \text{ K}$ are required for significant fluxes at these energies. It is possible for higher temperatures to occur in more compact models, but the duration of any resulting pulse is very short, and in general $T_e \leq 10^5 \text{ K}$, so that the current calculations suggest only an intense burst of ultraviolet radiation with $\int L dt \lesssim 6 \times 10^{48} \text{ ergs}$. It is possible that at later times, however, in the postpeak evolution of the expansion, the outer layers of the circumstellar shell (or any penetrating high-velocity Rayleigh-Taylor blobs) might show appreciable heating as they interact with the ambient interstellar medium. Temperatures in excess of 10^7 K are likely. Consider the conversion of kinetic energy to thermal energy in such an interaction: approximately

$$\Delta(\frac{1}{2}v^2) \approx \Delta(PV + E) \approx \Delta(\gamma \mathcal{R}T),$$

so that for an ideal gas, $T \approx v^2/2\mathcal{R}\gamma$ and velocities of expansion in excess of 5000 km s^{-1} imply temperatures of some 10^9 K .

iii) Character of the Light Curve

It is a feature of the extended model that the "visual" light curve parallels the bolometric. The peak epoch is dominated by near-ultraviolet radiation (cf. Model C, Fig. 23), and in general the bolometric correction is minimized *after* peak light. On the contrary, in compact models the "visual" peak (if present) comes after the bolometric "spike" and is purely a temperature effect, due to the occurrence of a bolometric correction minimum occurring as the effective temperature passes through $T_e \approx 10^4 \text{ K}$. It may or may not occur in coincidence with the slight rise in the bolometric light curve after the luminosity spike. Presupernova envelopes with small masses ($M_{\text{env}} \lesssim 2-3 M_\odot$) and steep (e.g., exponential) density distributions may accentuate this feature (cf. Chevalier 1976). The assumption of massive red-giant-like presupernova configurations tends to minimize this bolometric bump, which is a result of initially rapid photospheric expansion; it is enhanced by high exterior velocities. The general flatness of the giant or supergiant envelope density profile tends to de-emphasize this feature, which is enhanced by the acceleration of a shock in a steep density gradient. Suppose the shock energy is characteristic of the collapse in the core regions and is therefore fixed. A reduction in envelope mass will then result in higher mean velocities, while any large convective density inversion in the outer layers of the presupernova envelope will tend to hold down these values. In the case of extended presupernova configurations, the resulting light peak may camouflage this bump entirely. This portion of the light curve, in both extended and compact models, is therefore a qualitative indicator of presupernova envelope structure and mass.

The success of a simple diffusion picture for the postpeak (or postspike) evolution of the light curve suggests that it may be possible to crudely estimate the mass of expanding matter by fitting well-observed light curves with expressions of the form of equation (24). A rough extrapolation backward in time of inferred values for R_{ph} would suffice to give the $\exp(-R_0 t)$ term, and mean values of expansion velocity inferred from line spectra would provide a specification of the $\exp(-v^2 t/2)$ term. An approximate determination of $k \approx 3K/4\pi c$ would provide reasonable estimates of the mass involved.

iv) Velocities

Shell densities so low that acceleration is primarily due to a diffusion wave are typical of the extended models. Mean shell velocities will then be of the order

$$\langle v_s \rangle \lesssim \frac{1}{4\pi R_s^2} \frac{\bar{\kappa}}{c} \int_0^t L_{\text{bol}} dt, \quad (26)$$

which is essentially *independent of the mass of the shell*. The parameters of model B give an expected value $\langle v_s \rangle \lesssim 2.7 \times 10^3 \text{ km s}^{-1}$, for an assumed 30% radiation efficiency in the peak epoch (cf. Table 6). Other models are less efficient. The calculated values for

model B are somewhat lower, but represent fair agreement with this estimate. In addition, "back pressure" by the inertia of the slowly expanding shell will slow the pseudoviscous shock and tend to reduce velocities. We note that the extended models presented here all have relatively massive gradient and shell configurations, which must contribute to the low velocities, especially extreme in the case of model B ($v \approx 2000 \text{ km s}^{-1}$).

Grain material is not likely to survive the large luminosities of the peak epoch (Falk and Scalo 1975), so that no obvious recourse to high opacity sources in the shell matter is available to boost shell velocities. Assuming fixed total energy $E_0 \approx 10^{51} \text{ ergs}$ and an approximately constant radiative efficiency, two obvious possibilities exist for increasing $\langle v_s \rangle$ to observed maximum values. The first is to reduce the mean radius of the shell region, since $\langle v_s \rangle \propto R^{-2}$. But this reduction in scale involves a corresponding reduction in the expected values for the peak width t_p , since the diffusion time is $t_d \propto R^2$. In addition, as is evident from a comparison of the models presented here, a decrease in radiative efficiency accompanies a decrease in this length scale. The necessary factor of from 2 to 5 (or more) increase in $\langle v_s \rangle$ inferred from models F and B therefore suggests a decrease of from 2 to 5 in peak width, respectively. The lower factor is perhaps not unreasonable in view of the fact that observational data on the peaks of Type II events are at best sketchy, especially with regard to prepeak observations. The higher factor is, however, too large to give 10–20 day peak widths.

A second possibility for increasing the mean shell velocity is suggested by observing that

$$\langle v_s \rangle \propto t_p R^{-2} \propto \bar{\rho}, \quad (\Delta R)^2 \approx R^2.$$

An increase in mean shell density will tend to increase t_d . Used in conjunction with a small decrease in R for the shell, it might be possible to maintain satisfactory peak widths while increasing the velocity of the shell. Models C, E, and F show the effects of this compromise when compared with model B. The velocities in these cases are a factor of from 2 to 3 larger than for model B, and each has "acceptable" peak widths; even so, $\langle v_s \rangle$ remains too small to explain adequately the observed maximum velocities.

The possibility exists that the exterior shell velocities are not responsible for the velocity maxima, which are inferred from line spectra, usually from two to three weeks postmaximum. If the behavior of the shell was such that it became significantly transparent by this time, material at the exterior of the envelope proper would become visible. This material, especially that in the higher density range of the steep density gradient, could reasonably be expected to attain the velocities necessary to explain the observations. The likelihood of significant cooling and recombination in the shell during this epoch, however, is small, both because of the low expansion rate (adiabatic losses are too small) and the continuous illumination by the

interior regions, with enough radiation shortward of the Lyman limit to maintain a high ionization level.

Our suggestion in the context of these extended models is that the high material velocities inferred from line shape represent the emergence of fast-moving clumps of hot, dense matter from the exterior envelope which move through the overlying and partially swept-up shell material. This matter is expected to produce a Rayleigh-Taylor unstable interface upon its initial expansion into the shell matter. It then penetrates this overlying, tenuous matter in times of order 1 to $2 \times 10^6 \text{ s}$. If $v_{\text{blob}} \approx 10^4 \text{ km s}^{-1}$, then the penetrating matter moves a distance $\Delta r \approx 10^{15} \text{ cm}$ in the first 10^6 s after the shock wave traverses the upper part of the density gradient, which actually precedes the occurrence of peak luminosity. There is ample time for some envelope matter at even lower velocities (say $v \approx 5000 \text{ km s}^{-1}$) to penetrate the shell by some $2 \times 10^6 \text{ s}$ (~ 3 weeks) postpeak. The line wings will then be dominated by the presence of this material, and the shell components, while they are still optically thick, will contribute only to the dominant, low-velocity part of the P Cygni line profiles observed.

We remark in the general context of this part of the discussion that the velocities calculated for the outermost material zones depend strongly on the finite difference zoning used. To illustrate this point, a model (A1) very similar to model A was calculated; the difference in zoning is reflected in Figure 2, which shows the (dashed line) outer solar mass or so of $\rho(m)$ assumed for this case. Twenty-six zones are utilized in the outer $2.0 M_\odot$ partial gradient shown, in place of the seven such zones used in model A. The light curve for this model closely followed that of model A, except that the bolometric luminosity spike was more energetic ($L_{\text{max}} \lesssim 5 \times 10^{44} \text{ ergs s}^{-1}$) and slightly delayed in time (by $\Delta t \leq 5 \times 10^4 \text{ s}$) relative to that of model A. Peak widths were very nearly identical, with that of model A1 very slightly the larger. The most noticeable difference was in the velocities of the outer gradient zones, which showed maximum values (immediately postpeak) of $v \approx 6.26 \times 10^3 \text{ km s}^{-1}$, an increase of almost 30% over those of model A at a corresponding time ($v_{\text{max}} \approx 4.8 \times 10^3 \text{ km s}^{-1}$). Much of this increase can be attributed to the presence of a density gradient and the consequent speed-up of the shock wave in this region, but the velocity structure of the outer $2 M_\odot$ region (including nongradient zones) showed systematic increases of from 10 to 15% over corresponding values obtained for model A. Further examination of such zoning sensitivity is presently underway.

v) Turbulent Velocities

Turbulent velocities estimated by the ad hoc numerical procedures described in Appendix C are found to be of order $100\text{--}500 \text{ km s}^{-1}$, with total energies $3 \times 10^{-4} E_0$ to $3 \times 10^{-3} E_0$ in the extended models, where the higher values occur in those cases with initially steeper outer density gradients. The presence of turbulent motions in these models therefore has a negligible qualitative effect upon either the light curve

TABLE 14
TURBULENT OUTER REGIONS ($M > 5 M_{\odot}$) IN
MODEL C AT VARIOUS TIMES*

t_6	M_t	v_t	Δm_t	N
0.609	7.06	0.11–1.2	0.19	3
0.682	7.13	1.0–1.5	0.15	3
0.756	7.13	0.8–1.8	0.15	3
0.916	7.11	0.6–2.6	0.38	6
1.031	7.11	0.9–2.8	0.38	6
1.122	7.18	1.2–1.8	0.15	3
1.228	7.00	0.8–2.1	0.31	4
1.300	7.08	0.5–1.5	0.75	4
1.392	7.12	1.0–2.1	0.81	5
1.470	7.03	1.1–1.5	0.84	5
1.566	6.78	0.8–2.7	0.65	4
1.641	6.46	0.5–1.2	1.7	3
1.735	6.46	0.9–1.9	1.7	3
1.812	6.96	1.1–3.7	1.9	11
1.869	6.96	0.7–5.2	1.9	11

* M_t is approximate mass coordinate of the center of a given region of turbulence, Δm_t is the mass involved in the turbulence, and N is the number of mass zones involved. All masses are given in units of M_{\odot} ; times are given in units of $t_6 \equiv t/10^6$ s. The quantity v_t is the mean turbulent velocity predicted for the given region (or range of values) in units of 10^2 km s $^{-1}$. These values result from a treatment of density inversions outlined in Appendix C. Zones with $v_t < 50$ km s $^{-1}$ have not been included.

or overall expansion hydrodynamics. Because these motions are localized in mass coordinates, they can represent small but not insignificant fractions of local kinetic energies. In model C, for example, the turbulent energy is estimated to be of order $K_t(t_6 \approx 1.9) \approx 7 \times 10^{47}$ ergs, which is almost 0.025 of the 2.7×10^{49} ergs of the local kinetic energy of bulk expansion for these same layers. These values are at best only crude

TABLE 15
TURBULENT REGIONS IN MODEL B AT SELECTED TIMES*

t_6	M_t	v_t	Δm_t	N
0.301	1.44	2.4	0.2	1
0.402	1.44	3.7	0.2	1
0.502	1.44	3.4	0.2	1
0.981	2.71	2.4	0.2	1
1.08	2.91	1.4	0.2	1
1.79	3.67	2.2	0.4	2
1.94	3.87	2.5, 2.3	0.4	2
2.03	3.77	2.4	0.2	1
2.34	3.77	2.7, 2.4	0.8	4
2.74	3.95	2.7, 2.4	0.8	4
3.24	3.90	2.9, 2.5	1.2	6
4.01	4.10	3.0, 2.7	1.0	5
4.51	4.3	3.0, 2.7	0.8+	4+

* M_t is approximate mass coordinate of the center of a given region of turbulence, Δm_t is the mass involved in the turbulence, and N is the number of mass zones involved. All masses are given in units of M_{\odot} ; times are given in units of $t_6 \equiv t/10^6$ s. The quantity v_t is the mean turbulent velocity predicted for the given region (or range of values) in units of 10^2 km s $^{-1}$. The values result from the introduction of a second pseudoviscous pressure ("isotropic turbulence") in density inversion regions, not from the treatment of Appendix C. This pressure is proportional to the density contrast $\Delta\rho/\rho$ between adjacent mass zones.

TABLE 16
TURBULENT REGIONS FOR MODEL E*

t_6	M_t	v_t	ΔM_t	N
0.238	7.17	1.6	0.1	1
0.316	7.37	3.3	0.1	1
0.417	6.27	2.3	0.3	1
	7.42	3.6	0.2	2
0.819	5.91	2.7, 0.9	1.9	7
1.02	6.01	2.5, 1.1	2.1	9
1.22	5.51	2.2, 0.9	2.4	8
	8.02	3.2	0.2	1†
1.32	5.66	2.2, 1.3	1.5	5
	8.02	4.9	0.2	1†
1.42	5.51	2.4, 1.4	1.2	4
	8.02	4.77	0.2	1†
1.52	5.21	2.5, 1.3	2.1	7
	8.02	5.0	0.2	1†
1.62	5.51	2.5, 1.3	1.2	4
2.02	4.46	1.2, 0.3	1.5	5
2.67	4.46	1.7, 0.4	1.5	5
2.87	4.61	1.8, 0.3	1.8	6
3.07	4.61	1.8, 0.3	1.8	6
3.53	4.61	1.7, 0.4	1.8	6
3.70	4.61	1.7, 0.4	1.8	6

* Notation as in Table 14. Values result from a pseudoviscous turbulent pressure, as in Model B.

† Indicates a zone in the region of the photosphere.

estimates, but the suggestion of large-scale turbulence with random velocities of order 100 pm s $^{-1}$ is definite throughout much of the exterior regions of the expanding envelope (see Tables 14–17). Higher values are likely in the density inversion itself, in the range 200 – 500 km s $^{-1}$. We emphasize that the ad hoc technique

TABLE 17
TURBULENCE IN MODEL F*

t_6	M_t	v_t	ΔM_t	N
0.535	7.47	5.3, 0.5	0.6	7
0.638	6.27	1.6, 0.3	1.1	4
	7.47	5.4, 0.9	0.6	7
0.736	5.96	..	1.8	7
	7.47	4.4, 2.3	0.6	7
0.836	6.01	2.0, 1.0	1.9	8
	7.47	3.5, 0.1	0.6	7
1.04	6.01	3.1, 1.5	1.9	8
	7.56	2.9, 1.0	0.6	6
	8.12	2.8	0.2	1†
1.14	5.76	2.9, 1.6	2.6	11
	7.61	2.5, 1.0	0.7	7
	8.12	3.5	0.2	1†
1.72	5.06	3.2, 0.2	1.8	6
	8.59	2.5	0.2	1‡
2.56	4.61	3.0, 1.1	2.7	9
3.35	4.61	2.6, 1.2	1.5	5
3.82	4.61	3.0, 1.2	1.5	5
4.33	4.30	2.4, 0.7	1.5	5
4.70	4.30	2.4, 0.9	1.5	4

* Notation as in Table 14. Here also values result from the introduction of a turbulence pseudoviscous pressure similar to that of Model B.

† Indicates a zone in the region of the photosphere.

‡ Denotes a zone immediately interior of the photospheric mass zone.

used to smear out these regions in mass coordinates probably represents a maximization of this effect. Especially in the outermost inversion regions, significant interpenetration of the two density phases may occur *before* adequate momentum transfer can occur in the mean between the swept-up shell medium and the rapidly penetrating low-density (envelope) blobs.

These motions will certainly contribute to spectral line broadening in the postpeak spectra. Their effect may, however, be obscured by the large velocity gradient sampled by even the strongest (and most optically thick) lines. Additionally, if interpenetrating fingers and blobs do not dissipate on time scales short compared with the increase of transparency, then Doppler broadening from these slow- and fast-moving phases coexisting at a given locale may also dominate any large-scale turbulent structure.

vi) Photospheric Recession

The single most sensitive piece of input physics in these calculations is the assumed form of the opacity. As discussed for model A, these calculations assume a Population I composition and an artificially high level of opacity at the lower temperatures. At late times when recombination has been significant, an overestimation of κ for $T \leq 6000$ K will lead to a slower recession of the photosphere than would otherwise be the case. Observational inference of substantial ionization levels at late times (40–100 days postpeak; see Kirshner and Kwan 1975) tends to support the view that significant electron scattering optical depths exist between the outer radius and the recombination wave. A decrease by a factor of 10, however, in the assumed level of κ would suffice to reduce the photospheric radius at late times (e.g., $t_6 \approx 4.0$) to a value not very different from that of the recombination wave, whose position as a function of time is also plotted in Figure 6 and which represents a “surface” of essentially constant temperature $T_{\text{re}} \approx 5000$ K. We remark that other uncertainties complicate the late-time behavior of the regions external to R_{ph} , notably the breakdown of the diffusion approximation for small optical depths, and the fact that recombination times may be long in comparison with characteristic changes in density in the high-velocity expansion.

The need for an accurate nonequilibrium (i.e., $\int \kappa J d\nu = \int \kappa B d\nu$ not assumed) transport treatment of the transparent regions is evident, both as regards an accurate determination of the detailed opacities, and as regards theoretically modeling the gross spectral features, which depends upon being able to specify the radiation field as well as material temperatures. Future treatments of the postpeak epoch will certainly include this form of calculation. In this regard, we reiterate the observation that in general at the low postpeak densities characteristic of these expanding envelopes, the recombination wave should not contribute markedly to the energy budget of the envelope. However, the postpeak *level* of the light curve does depend upon the details of a temperature-dependent opacity which varies from a constant electron scattering value. The light curve of model F1 (shown in

Fig. 15b) reflects this behavior. Models F and F1 were identical except that $\kappa = \kappa_{\text{es}} = \text{constant}$ was used in the calculation of F1. The postpeak level of the light curve dropped below that calculated for model F at $t_6 \approx 3.4$, notably because of a more rapid growth of transparency in the case which included recombination effects on the opacity.

vii) Exposure of the Core and Mantle

If the original star were not too massive, most of the core mass might be expected to form a collapsed remnant ($M_c \lesssim 1.4 M_\odot$). In particular, if supernovae of Type II are to be associated with pulsars (Ostriker and Gunn 1971; Bodenheimer and Ostriker 1974), then the pulsar radiation should become directly observable after times of order 10^7 s. The presence of a luminous pulsar with slowdown times τ_i typically of order 10^8 s (cf. Bodenheimer and Ostriker 1974) would certainly have significant effects upon the energy budget (and expansion rate, ionization levels, etc.) of even massive envelope models at times of order several times 10^6 s. In particular we examine the relations used by Bodenheimer and Ostriker for the pulsar luminosity:

$$L(t) \approx L_i(1 + 2t/\tau_i)^{-2} \text{ ergs s}^{-1}, \quad (27)$$

where

$$L_i \equiv \frac{2B^2 a^6 \Omega_i^4}{3c^3} \approx 7.4 \times 10^{28} B_{12}^2 \Omega_i^4 \text{ ergs s}^{-1}, \quad (28)$$

$$\tau_i \equiv \frac{3c^3 I}{2B^2 a^6 \Omega_i^2} \approx 1.9 \times 10^6 \Omega_i^{-2} B_{12}^{-2} \text{ s}, \quad (29)$$

and $B_{12} \equiv B/10^{12}$ gauss is the surface strength of the (dipole) magnetic field; a is the pulsar radius, taken to be 1.2×10^6 cm, and I is the pulsar moment of inertia, with a value $I \approx 1.4 \times 10^{45}$ g cm² (Ostriker and Gunn 1969, 1971). For the Crab pulsar NP 0537, $B_{12} \approx 2.6$ and $\Omega_i \approx 10^4$, suggesting $L_i \approx 5 \times 10^{45}$ ergs s⁻¹ with magnetic decay constant $\tau_i \approx 2.8 \times 10^7$ s ≈ 1.17 yr. In the case of such a rapidly rotating pulsar, equation (27) gives $L(t_6 \approx 10) \approx 1.7 \times 10^{45}$ ergs s⁻¹, a value well in excess of the output luminosity of even the most massive models presented here and certainly large enough to affect the light curve profoundly. Even for values of L_i of the order supposed by Bodenheimer and Ostriker ($L_i \gtrsim 4 \times 10^{43}$ ergs s⁻¹), the pulsar would provide some 3×10^{42} ergs s⁻¹ to the expanding system by $t_6 \approx 10$, of the order or greater than the later postpeak values of luminosity attributed to the models presented above. As transparency of the expanding matter increases, by about $t_6 = 10$, then, the presence of a pulsar would tend to raise the level of the light curve at late times, and also provide a generally high level of radiative ionization. Transparency would ensue chiefly as a result of the continuing density decrease, and the photosphere would increase to large values ($R_{\text{ph}} \approx 5 \times 10^{15}$ to 10^{16} cm). That such behavior is not inferred from observed SN II is suggestive of the *disassociation* of (at least

fast pulsar formation with typical Type II events. If we take $B_{12} \approx 1$ as representative of most pulsars (cf. Gunn and Ostriker 1970), relation (27) yields

$$\begin{aligned} L(t) &\approx 7.4 \times 10^{28} \Omega_i^4 (1 + 10^{-16} \Omega_i^2 t)^{-2} \\ &\approx 7.4 \times 10^{28} \Omega_i^4 \end{aligned}$$

for $t_6 \lesssim 100$ and $\Omega_i \lesssim 3 \times 10^3$, say. Our models suggest that an embedded pulsar cannot contribute more than about 10^{42} ergs s⁻¹ at times $t_6 \approx 10$ without significantly affecting both the light curve and possibly the overall kinetics. This in turn implies that values of Ω_i greater than about $\Omega_i \approx 2000$ s⁻¹ are not likely for ordinary SN II. Indeed, the upper limit of 10^{42} ergs s⁻¹ imposed is probably generous; it is likely that values of $L_{\text{pulsar}} \gtrsim 0.2$ to 0.3 or so of $L_{\text{SN}}(t_6 \approx 10) \approx 10^{42}$ would be sufficient to affect the light-curve shape and time scales noticeably. It is also likely that the visual magnitudes of our models are too high in comparison with the "typical" value of -17.6 mag (Tammann 1974). In this case, then, it is possible that a reasonable upper limit on permissible values of Ω_i might be even smaller by factors of from 3 to 5 or more, i.e., $\Omega_i \lesssim 500$ –1000 s⁻¹. Detailed light-curve models for events with embedded energy sources are being calculated in order to examine such an upper limit.

The onset of envelope transparency will also serve to expose the underlying core or mantle material, which in general consists of material which has undergone at least some static burning stages past helium burning and may, in more massive stars, include material which represents end products of explosive nucleosynthesis. The presence of large amounts of radioactive material (notably ^{56}Co , $t_{1/2} \approx 77$ days) would almost certainly be evidenced directly by γ -ray lines by $t_6 \approx 10$ –12 in envelopes of low to moderate mass ($\lesssim 10 M_\odot$), but the intensity of these lines is expected to remain near or below observable limits unless the material is present in quantities which could significantly affect the observed light curves. That SN II do not appear to require such energy sources suggests that inordinately large amounts of such material are not present. Because transparency does not in general occur until $t_6 \geq 4$ even in low-mass models, lines of shorter-lived radioactivities (e.g., $^{56}\text{Ni} \rightarrow ^{56}\text{Co}$, $t_{1/2} \approx 6$ d) would not be expected to be observably intense except in nearby galactic supernovae.

A strong shock wave which originated in the mantle/core region would serve to accelerate this material to high velocities, where it would expand, acting as a hot piston, into the overlying envelope. Resulting contact discontinuities might result in turbulent mixing of the exterior mantle material with the interior envelope material. As in the case of the outer envelope density gradient, such turbulence might be expected to form interpenetrating fingers (envelope) and blobs (mantle) of high relative velocity. The problem of deducing compositional exposure would then be complex, and might consist of a more gradual exposure of processed material as transparency developed. The presence of

enhanced metal abundance would affect the opacities characteristic of this interior mass, and would serve to lower the effective recombination temperature if enough such material were admixed into the envelope. The detailed structure of such regions might have implications for subsequent cosmic-ray acceleration.

f) Summary and Conclusions

The shock wave model presented here can provide a reasonable explanation of the overall morphology of SN II light curves. Quantitative agreement with observed mean velocities of expansion and temperature histories is good, and natural explanations emerge from the models themselves for many of the detailed observations of these events (see Arnett and Falk 1976).

Schematics for the bolometric light curves of the two model types (i.e., with and without presupernova mass-loss "shells") are given in Figure 25. In the two cases, the post-(bolometric) peak behavior of the light curves is similar. An initial phase of expansion and cooling occurs, during which time the growth of the photosphere is rapid, and the light curves flatten (with L_{bol} perhaps increasing slightly) on time scales of order 3 – 4×10^6 s. Characteristic temperatures drop to values of order 1×10^4 K or less during this time, and this phase can be associated with a minimum bolometric correction. For the compact models, any visual peak light is associated with this correction minimum, while for extended models visual peak light is associated with a well-defined bolometric peak of duration 10–20 days. As temperatures fall, recombination sets in, the photospheric mass coordinate decreases (radii grow), and the light curve is characterized by falling diffusive time scales; the light curve turns concave downward. As recombination becomes complete throughout the bulk of the expanding envelope material, the light curve turns quasi-exponentially downward. Interior regions will be exposed, therefore, on time scales of order 5×10^6 to 1×10^7 s, with the more massive envelopes requiring longer times. This relation, with assistance from an adequate parameter study of the theoretical light curves, may provide a method for estimating the initial envelope masses involved from observational data of particular cases.

The light-curve models presented here currently provide the best self-consistent explanation of the three major features of SN II light curves: a history of effective temperature and velocity, a postpeak plateau, and a final turndown on reasonable time scales, without any need to invoke energy sources or special features which do not occur naturally in the context of the simple shock model. The presupernova mass loss required for extended models is not out of line with evolutionary development of massive stars, and the models which use "natural" (i.e., red-giant-like) presupernova structures provide the best overall agreement with observational evidence. The observed variation in SN II light curves can be explained in terms of an acceptable mass range for SN II.

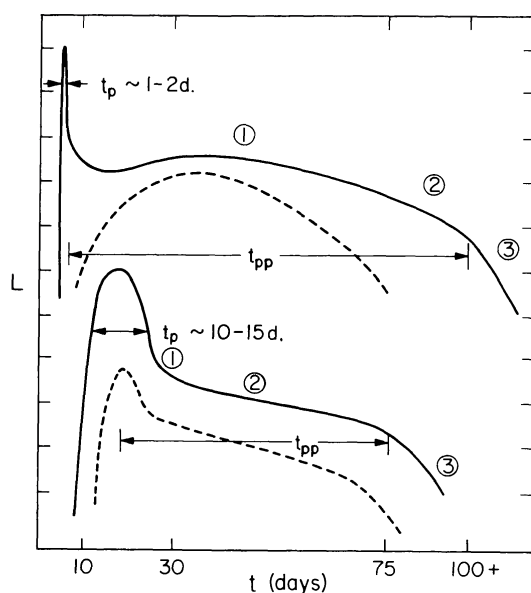


FIG. 25.—Schematic light curves. Schematic light curves are shown for typical compact models (upper solid curve) and extended models (lower solid curve). Also shown are qualitative “visual band” light curves for both model types. The compact model consists of three distinct phases following the peak pulse of width $t_p \approx 1-2$ days (characteristic of shock emergence at the photosphere and subsequent rapid adiabatic cooling of the outer optically thick regions). Phase 1 corresponds to a period of rapid growth in the effective radiating surface, $L \propto R_{ph}^2$, before recombination results in a rapid increase in material transparency. Phase 2 corresponds to the onset and progress of recombination in the expanding envelope, with the photosphere receding in mass coordinate. The light curve turns concave downward, until recombination is essentially completed; phase 3 is the resulting sharp turndown in the light curve which results from the decrease in opacity in the now cool ($T \lesssim 5000$ K) central regions of the envelope ejecta. These same stages are present in the extended models as well, although phase 1 is less distinct because of the wide light peak. In this case $t_p \approx 10-15$ days is a result of diffusion of radiation ahead of the shock front in low-density circumstellar shell matter. For this class of models, the visual light curves may be expected to mirror the shape of the bolometric, also having a well-defined peak structure. In both cases the time t_{pp} (with a knowledge of material velocities) is a crude measure of envelope mass. These curves are intended to be suggestive of typical light-curve morphology, and do not correspond to specific models. The luminosity scale is arbitrary and the time coordinates are not necessarily drawn to scale.

The success of this approach for Type II events suggests that these model ideas be extended to the much more (observationally) regular Type I events. Recent calculations, notably by Lasher (1975), support the idea that shock wave models can explain at least some features of SN I light curves, though the details may be quite different than for SN II. In particular, Lasher's model for a Type I light-curve peak results from a strong shock wave traversing an idealized giant envelope ($R \approx 10^{14}$ cm, $\rho \approx 10^{-8}$ g cm $^{-3}$ = constant) of some $2 M_\odot$. This is easily seen to be a low-mass case of the bare envelope scenario presented above. The envelope, to be sure, is assumed to have a dominantly helium composition, but the assumption of complete ionization results in opacities dominated

by electron scattering, as is true for the high-temperature ($T \gtrsim 10^4$ K) phases of the models with normal (solar) abundances presented here. The effect of assuming a small envelope mass is to temporally compress the duration of the postpeak plateau to the desired 20 days typical of observed SN I peak epochs. Well-observed light peaks are approximately Planckian (Kirshner *et al.* 1973), so it seems reasonable to speculate that at least this phase of Type I events qualitatively resembles the postbolometric spike phase which results from low-mass bare envelope configurations. The situation is confused somewhat by the observational data for SN 1975a (Type I) in NGC 2207, which imply a prepeak radius of order 10^{15} cm (Kirshner, Arp, and Dunlap 1976), and which may be suggestive of the preexplosion conditions supposed for our extended models. It is interesting to note that evolutionary calculations and observations of the Crab Nebula (Arnett 1975) imply that He stars become red giants with low-mass helium envelopes.

No attempt has been made to include effects due to line transfer in the models discussed here. We expect the overall dynamical behavior of the ejected envelope to be largely unaffected by line contributions. Shock temperatures are high enough to insure that electron scattering dominates the opacity during the peak (spike) epoch when virtually all acceleration of the ejecta occurs. (Because the temperatures which characterize helium ionization are substantially higher than those corresponding to hydrogen ionization, the presence of He bound-bound and bound-free opacities which may be significantly “Doppler-enhanced” by the presence of a large material velocity gradient could have a pronounced effect upon the early dynamical acceleration of supposedly He-rich SN I envelope material [Karp *et al.* 1976]. It is possible that such an effect may be in part responsible for higher maximum expansion velocities in SN I than in SN II.)

Line effects on the spectra of both types can be qualitatively understood in terms of these models. The velocity gradient in the expanding material will result in Doppler-broadened lines and characteristic P Cygni line profiles. Velocities derived from observations of such features show good agreement with predicted behavior in the theoretical models (e.g., Arnett and Falk 1976). As the material expands and cools, line optical depths decrease continually as material densities fall and recombination progresses. Strong emission lines will then show a redward drift with time as lower-velocity layers are exposed. Weaker lines, formed over a larger mass fraction, will show a less pronounced drift, which may manifest itself as only a change in the line profile itself, de-emphasizing highly blueshifted components.

The gross effect of any large-scale fluid instabilities (e.g., Rayleigh-Taylor) is to provide another mechanism for line-broadening. Effects of any asymmetry in the expanding material (nonspherical, presence of blobs, etc.) are difficult to anticipate in the context of the simple spherical model employed here. The continued reduction of the optical thickness of the

ejecta will also result in exposure of layers with a more highly processed composition. The emergence or enhancement of lines of these elements and their subsequent increase in strength relative to those elements which characterize the outlying material (e.g., possible CNO nuclei, He, H) is also a natural consequence of the simple models. Rayleigh-Taylor mixing, or significant presupernova convection, would greatly complicate this picture, modifying both the observed velocity field and compositional layering.

The effects of line transfer on the character of observed light curves are less clear. In both types, lines become increasingly strong relative to the continuum after peak light, but are effective in the transport of radiation only in SN I (Kirshner *et al.* 1973). These authors suggest that SN II spectra remain generally Planckian, with superposed lines, over most of the early light curve ($t \lesssim 100$ days); this suggests that the transformation from theoretical (bolometric) to observational curves (e.g., B -band) is, in principle, straightforward. The situation for postpeak SN I epochs is, contrarily, complicated by the presence of emission lines which apparently dominate the transfer of visible radiation (see, however, Mustel 1976). Because of uncertainties in the initial composition (SN I may be hydrogen-depleted) and in subsequent compositional exposure, and questions of mixing via fluid instabilities, the problem of comparing theoretical curves with observed data is rendered complex. A detailed, nongray, nonequilibrium calculation, using carefully constructed opacities, is called for, apparently in even the simplest of SN I models. The explicit inclusion of such effects is conceptually straightforward

in an approach which averages important line contributions across suitably chosen (broad) frequency bands. The frequency-dependent nonequilibrium Eddington factor method outlined above may be suited to such studies.

Much work remains to be done. A parameter study which systematically examines the dependence of velocities and light curves upon envelope and shell masses and configurations, compositions, and shock energies is required. To this end, detailed opacities and an accurate transport method of calculation are necessary for examination of the radiative character of these objects. Such a study has begun, and is expected to supply information sufficient to allow reasonable model-fitting to particular light curves. In this way, it may be possible to use SN II as distance indicators (cf. Arnett and Falk 1976), despite their morphological irregularity. We feel confident that the shock-wave explanation for supernova light curves is indeed qualitatively and quantitatively correct, and that our understanding of these catastrophic events is rapidly improving.

We would like to thank Drs. Richard Epstein and John Scalo for many helpful conversations during the course of this research. Much of this work was performed while one of us (S. W. F.) was a graduate student at the University of Texas at Austin; the support and encouragement of the Department of Astronomy is gratefully acknowledged. Special appreciation is expressed for the unsung and patient typing of the seemingly endless drafts and tables by Kellogg's Jan Rasmussen.

APPENDIX A THE DIFFERENCE EQUATIONS

I. HYDRODYNAMICS

The model "star" is represented by concentric spherical shells of (zone) mass $\Delta m_{k+1/2}$ which form a Lagrangian coordinate system. The hydrodynamic calculations are performed in boundary masses $\Delta m_k \equiv 0.5(\Delta m_{k-1/2} + \Delta m_{k+1/2})$ as if they were mass "plates." (Hereafter, subscripts k and $k + \frac{1}{2}$ refer to quantities evaluated at zone boundaries and zone centers, respectively.) The calculational procedure is to take known radii and velocities at time n (denoted by superscript n : t^n) and determine the new values $v_k^{n+1/2}$, r_k^{n+1} for all values of k , according to the relations

$$v_k^{n+1/2} = v_k^{n-1/2} - 4\pi(R^{n+\lambda})^2[P_{k+1/2}^{n+\lambda} - P_{k-1/2}^{n+\lambda} - Q_{k+1/2}^{n-1/2} + Q_{k-1/2}^{n-1/2}] \frac{\Delta t^n}{\Delta m_k} - \frac{GM_k}{(R^{n+\lambda})^2} \Delta t^n + Z_k^{n+\lambda} \Delta t^n, \quad (A1)$$

$$R_k^{n+1} = R_k^n + v_k^{n+1/2} \Delta t^{n+1/2}, \quad (A2)$$

where

$$M_{k+1} \equiv M_k + \Delta m_{k+1/2} = \sum_{x=0}^k \Delta m_{x+1/2} \quad (A3)$$

is the total mass interior to boundary $k + 1$; the time step $\Delta t^{n+1/2}$ is chosen subject to limitations of stability and accuracy of the particular scheme chosen (e.g., see remarks in Appendix B) and represents the time interval $(t^{n+1} - t^n)$, where also $\Delta t^n \equiv 0.5(\Delta t^{n+1/2} + \Delta t^{n-1/2})$. Z^n is the gradient of the radiation pressure, given by

$$\begin{aligned} Z_k^n &= -A_k \frac{\partial P_r}{\partial m} \Big|_k^n = -A_k \frac{\partial}{\partial m} \left(\frac{a}{3} T^4 \right), \quad \tau \gg 1 \\ &= \frac{1}{c\rho_k^n} \int_0^\infty k_k^n(v) F_k^n(v) dv, \quad \tau \lesssim 1 \end{aligned} \quad (A4)$$

where ρ is the matter density, $F(\nu)$ is the monochromatic flux, and $k(\nu)$ is the total monochromatic volume extinction (scattering + absorption), at time n at boundary k . P and Q are the gas and pseudoviscous pressures, respectively. The terms Q , after von Neumann and Richtmyer (see Richtmyer and Morton 1967), are numerical devices for the treatment of shock waves without numerical discontinuities. A common choice for this pressure (Arnett 1966a) is adopted:

$$Q_{k+1/2}^{n+1/2} = 2(v_{k+1}^{n+1/2} - v_k^{n+1/2})^2 \rho_{k+1/2}^{n+1/2}, \quad \begin{cases} V_{k+1/2}^{n+1} < V_{k+1/2}^n \\ v_{k+1}^{n+1/2} < v_k^{n+1/2} \end{cases} \\ = 0, \quad \text{otherwise} \quad (\text{A5})$$

where the specific volume (and density) are given by

$$V_{k+1/2}^{n+1} \equiv (\rho_{k+1/2}^{n+1})^{-1} = \frac{4\pi}{3} [(R_{k+1}^{n+1})^3 - (R_k^{n+1})^3] \frac{1}{\Delta m_{k+1/2}}. \quad (\text{A6})$$

The pseudoviscosity Q must also be included in the energy equations, since it is a pressure term and can do work on the fluid. In the case of variable time increments, the velocity equation (1) must be written "centered" in time, not arithmetically, but geometrically as

$$\begin{aligned} R^{n+\lambda} &\equiv R[t^{n+\lambda}] = 0.5(t^{n+1/2} + t^{n-1/2}) = t^n + 0.25(\Delta t^{n+1/2} - \Delta t^{n-1/2}) \\ &= R^n \left(\frac{3}{4} + \frac{1}{4} \frac{\Delta t^{n+1/2}}{\Delta t^{n-1/2}} \right) + R^{n+1} \left(\frac{1}{4} - \frac{1}{4} \frac{\Delta t^{n+1/2}}{\Delta t^{n-1/2}} \right) \end{aligned} \quad (\text{A7})$$

after Talbot (1968). This scheme is implicit, as opposed to the explicit (fully forward-differenced) scheme which results for $\lambda = 0$, and must be iterated on R_x^{n+1} , P^{n+1} , and Z^{n+1} to achieve high accuracy. If, however, the energy and radiation equations are to be solved by an iterative procedure (see below), it is convenient to solve equation (1) explicitly, by use of an approximation of the form

$$R_k^{n+\lambda} \approx R_k^n + \frac{1}{4} v_k^{n-1/2} (\Delta t^{n+1/2} - \Delta t^{n-1/2}). \quad (\text{A8})$$

The outer layer is presumed to be in contact with a zero pressure medium.

b) Radiation in the Diffusion Approximation

In order to extend the time integration to the equilibrium diffusion energy equation, the zone temperatures at time t^{n+1} are given suitably extrapolated values $\tilde{T}_{k+1/2}^{n+1}$; the energy equations are linearized in corrections $\delta T_{k+1/2}$ to $\tilde{T}_{k+1/2}^{n+1}$, and evaluated at t^{n+1} . The resulting corrections modify the initial guesses, and the evaluation is repeated until the desired accuracy is obtained. To this end, spatial zone neighbors are coupled implicitly and the tridiagonal method of solution is employed; this method solves a system of equations of the form

$$\mathcal{A}_{k+1/2} X_{k+3/2} + \mathcal{B}_{k+1/2} X_{k+1/2} + \mathcal{C}_{k+1/2} X_{k-1/2} = \mathcal{D}_{k+1/2} \quad (\text{A9})$$

for the quantities $X_{k+1/2}$. A complete explanation of this method of solution is to be found in Richtmyer and Morton (1967).

The energy equation in the diffusion limit (§ III, eq. [4]) is written in partially backward difference form (space-centered):

$$\begin{aligned} (E_{k+1/2}^{n+1} - E_{k+1/2}^n) \frac{1}{\Delta t^{n+1/2}} + \frac{1}{2}(P_{k+1/2}^{n+1} + P_{k+1/2}^n + 2Q_{k+1/2}^{n-1/2}) \frac{1}{\Delta t^{n+1/2}} (V_{k+1/2}^{n+1} - V_{k+1/2}^n) \\ = -[\theta(L_{k+1}^{n+1} - L_k^{n+1}) + (1 - \theta)(L_{k+1}^n - L_k^n)] \frac{1}{\Delta m_{k+1/2}}, \end{aligned} \quad (\text{A10})$$

where

$$L_k^n = -[4\pi(R_k^n)^2]^2 \frac{ac}{3} \frac{1}{\bar{\kappa}} \frac{(T_{k+1/2}^n)^4 - (T_{k-1/2}^n)^4}{\Delta m_k} \quad (\text{A11})$$

and θ is a parameter which reflects the time-centering: $\theta = 1$ for fully backward differencing, $\theta = \frac{1}{2}$ for time-centering, and $\theta = 0$ for fully forward differencing.

Use is made of the relations

$$\begin{aligned} \dot{E} &= \frac{dE}{dT} \dot{T} + \frac{\partial E}{\partial V} \dot{V}, \\ \dot{P} &= \frac{\partial P}{\partial T} \dot{T} + \frac{\partial P}{\partial V} \dot{V}, \end{aligned} \quad (\text{A12})$$

to linearize the system (10), (11) in corrections $\delta T_{k+1/2}$ to the zone temperatures. The tridiagonal system is solved for the δT , the zone temperatures corrected, and the process repeated as necessary. This now-standard technique is discussed fully in Christy (1964) and Arnett (1966a).

c) Nongray Transport of Radiation

The procedure in the case of the radiation transport equations is similar to that outlined above for the diffusion equation, except that the first moment equation (12) is already linear in $E^v = (4\pi/c)J^v$ so that the inversion of the tridiagonal matrix constitutes the complete solution of the system of M (total number of spatial zones) linear equations for the $(E^v)^{n+1}$. The fluxes $(F^v)^{n+1} = (4\pi H^v)^{n+1}$ are then calculated at each boundary by use of the second moment equation (13). These equations are written in fully backward-differenced form in the Eddington approximation ($K^v = \frac{1}{3}J^v$, $\chi = \sqrt{3}$) as (superscript v suppressed):

$$\begin{aligned} \frac{1}{\Delta t^{n+1/2}} (E_{k+1/2}^{n+1} - E_{k+1/2}^n) + \rho_{k+1/2}^{n+1} \frac{1}{\Delta m_{k+1/2}} (A_{k+1}^{n+1} F_{k+1}^{n+1} - A_k^{n+1} F_k^{n+1}) \\ + \frac{4}{3} E_{k+1/2}^{n+1} \frac{1}{\Delta t^{n+1/2}} (\ln \rho_{k+1/2}^{n+1} - \ln \rho_{k+1/2}^n) + c \omega_{k+1/2}^{n+1} E_{k+1/2}^{n+1} \\ = 4\pi \omega_{k+1/2}^{n+1} b(T_g)_{k+1/2}^{n+1} \quad (A13) \end{aligned}$$

and

$$\frac{(F_k^{n+1} - F_k^n)}{c \Delta t^{n+1/2}} + \frac{c}{3} A_k^{n+1} \langle \rho \rangle_k^{n+1} \frac{1}{\Delta m_k} (E_{k+1/2}^{n+1} - E_{k-1/2}^{n+1}) = -k_k^{n+1} F_k^{n+1}, \quad (A14)$$

where $A_k^{n+1} \equiv 4\pi(R_k^{n+1})^2$ is the area of the spherical surface at radius R_k^{n+1} , $\omega_{k+1/2}^{n+1} \equiv (k_{\text{abs}})_{k+1/2}^{n+1}$ is the absorption coefficient for zone $k + \frac{1}{2}$, and

$$\omega^v b^v(T_g) = k_{\text{abs}}^v [1 - \exp(-h\nu/kT_g)] B^v(T_g) \quad (A15)$$

incorporates corrections due to induced emission.

Equation (A14) may be put into the form (superscript $n + 1$ hereafter assumed unless otherwise indicated):

$$F_k = \mu_k \left[\delta_k F_k^n - \frac{c}{3} (E_{k+1/2} - E_{k-1/2}) \right], \quad (A16)$$

where

$$\begin{aligned} \mu_k &\equiv (\delta_k + \Delta\tau_k)^{-1}, \\ \delta_k &\equiv \frac{\Delta R_k}{c \Delta t^{n+1/2}} = \frac{\tilde{R}_{k+1/2} - \tilde{R}_{k-1/2}}{c \Delta t^{n+1/2}}, \\ \Delta\tau_k &\equiv \kappa_k \langle \rho \rangle_k \Delta R_k = k_k \Delta R_k, \\ \tilde{R}_{k+1/2} &\equiv [\frac{1}{2}(R_{k+1}^3 + R_k^3)]^{1/3}. \end{aligned} \quad (A17)$$

Mass-weighted averages are denoted by subscripted brackets:

$$\langle y \rangle_k \equiv \frac{1}{2}(\Delta m_{k+1/2} y_{k+1/2} + \Delta m_{k-1/2} y_{k-1/2}) / \Delta m_k, \quad (A18)$$

with the exception of k_k , which is understood to be such an average.

d) Radiation Boundary Conditions

It is necessary to consider two classes of interior boundary conditions. The first and simplest occurs whenever the interior finite-difference boundary R_1 corresponds to $r = 0$ in the spherical system. In this case the interior boundary "separates" two mass zones which are identical by symmetry, having identical physical properties. In this case the energy density and flux derivatives vanish at $r = 0$:

$$\frac{\partial E^v}{\partial r} = 0 = \frac{\partial F^v}{\partial r}.$$

This has the effect of setting \mathcal{C} for the first spatial zone (interior) to zero in equation (9), and leads to modifications in the \mathcal{B} and \mathcal{D} coefficients which derive from the flux derivation at $r = 0$. These considerations apply to both the diffusion and transport schemes.

The application of the EDA scheme to the interior regions allows specification of a *net* flux F_{NF} at the interface between the two schemes. This fixes the value of the term $A^{n+1}F^{n+1}$ in equation (13) for $k = \text{NF}$ (see § III, eq. [4] and discussion following). Again, the result is to set $\mathcal{C} = 0$ and modify both \mathcal{B} and \mathcal{D} at zone NF + $\frac{1}{2}$.

Unlike the situation which obtains in ordinary model stellar atmosphere calculations, the emergent flux is not known *a priori*. Instead, this boundary must be “closed” by specifying F_{jj}^{n+1} (where subscript jj denotes the outer finite difference boundary) in terms of known boundary quantities, and quantities interior. In particular, the spatial derivative in equation (17) (§ III) must be determined self-consistently in terms of interior quantities.

The radiation energy density away from the boundary is determined by a second-order Taylor expansion,

$$E_{jj-1/2} = E_{jj} + (-\Delta m_{jj}) \frac{\partial E}{\partial m} \Big|_{jj} + \frac{1}{2}(\Delta m_{jj})^2 \frac{\partial^2 E}{\partial m^2} \Big|_{jj}. \quad (\text{A19})$$

The higher-order derivative may be specified in several ways; the choice essentially involves picking between a form explicit in the interior quantities or one which involves $(\partial E / \partial m)_{jj}$ itself. This latter “implicit” form is the more consistent with the choice of a backward-differenced tridiagonal formulation, and the approximation is made that near the boundary (i.e., at small r):

$$\frac{\partial^2 E}{\partial m^2} \Big|_{jj} \approx \frac{\partial^2 E}{\partial m^2} \Big|_{jj-1/2} \equiv \frac{1}{\Delta m_{jj-1/2}} \left(\frac{\partial E}{\partial m} \Big|_{jj} - \frac{\partial E}{\partial m} \Big|_{jj-1} \right) = \frac{1}{\Delta m_{jj-1/2}} \left[\frac{\partial E}{\partial m} \Big|_{jj} - \frac{1}{\Delta m_{jj-1}} (E_{jj-1/2} - E_{jj-3/2}) \right]. \quad (\text{A20})$$

Relation (18) is used to specify E_{jj}^{n+1} in terms of F_{jj}^{n+1} , and equation (19) gives a value for the spatial derivative in the first moment equation at the boundary

$$\frac{\partial E}{\partial m} \Big|_{jj} \approx \left(\frac{\chi F_{jj}}{c} - (1 + \beta)E_{jj-1/2} + \beta E_{jj-3/2} \right) \frac{2}{\Delta m_{jj}}, \quad (\text{A21})$$

where $\beta \equiv \Delta m_{jj}/2\Delta m_{jj-1}$ and the boundary mass $\Delta m_{jj} \equiv \frac{1}{2}\Delta m_{jj-1/2}$. Relation (21) may now be employed to cast equation (13) into difference form, with $f = 1/3$. The resulting difference equation may be solved for F_{jj}^{n+1} , yielding a form similar to equation (16),

$$F_{jj}^{n+1} = \mu_{jj} \left\{ \delta_{jj} F_{jj}^n + \frac{2c}{3} [(1 + \beta)E_{jj-1/2} - \beta E_{jj-3/2}] \right\}, \quad (\text{A22})$$

where δ_{jj} is defined by the second of relations (17), and

$$\mu_{jj} \equiv (\delta_{jj} + \Delta \tau_{jj} + \frac{2}{3}\chi_{jj})^{-1}, \quad (\text{A23})$$

where now

$$\begin{aligned} \Delta R_{jj} &= R_{jj} - \tilde{R}_{jj-1/2} = R_{jj} - \left(\frac{R_{jj}^3 - R_{jj-1}^3}{2} \right)^{1/3}, \\ \Delta \tau_{jj} &= k_{jj} \Delta R_{jj} \equiv \kappa_{jj} \rho_{jj-1/2} \Delta R_{jj}. \end{aligned} \quad (\text{A24})$$

The value of χ_{jj} which is consistent with the Eddington approximation is $\chi_{jj} = 2$ (see Mihalas 1970, p. 42).

The outer boundary condition for the linearized diffusion formulation corresponds to fixing a temperature at the boundary. This may be accomplished in the Eddington approximation by requiring

$$L_{jj} = \frac{ac}{3} A_{jj} T_{jj-1/2}^4 (\Delta \tau_{jj} + \frac{2}{3})^{-1}, \quad (\text{A25})$$

where

$$\Delta \tau_{jj} \approx \kappa_{jj} \Delta m_{jj} / A_{jj}. \quad (\text{A26})$$

For purposes of inverting the resulting tridiagonal matrix, the condition

$$T_{jj+1/2} \text{ (all } t\text{)} \equiv 0 \quad (\text{A27})$$

must be imposed in the “imaginary” zone outside R_{jj} . For both schemes, this “closure” at the outer boundary results in the tridiagonal coefficient $\mathcal{A}_{jj-1/2} = 0$, and modifies, in the EDA scheme, \mathcal{B} and \mathcal{D} for this outer zone; in the TDEA scheme, the coefficient $\mathcal{C}_{jj-1/2}$ is also modified.

e) *Matter-Radiation Coupling in the Transport Scheme*

The energy equation of the matter is given by a relation of the form (19) (in § III) where in general energy losses and gains by ionization, recombination, and other collisional processes must be included. For the purposes of the supernova light curves problem, this relation is adequately represented in the backward-differenced form

$$\left[\frac{\partial}{\partial t} E_g(T_g) \right]_{k+1/2}^{n+1/2} + (P + Q)_{k+1/2}^{n+1/2} \left(\frac{\partial}{\partial t} V \right)_{k+1/2}^{n+1/2} = \frac{1}{\rho_{k+1/2}^{n+1}} \sum_{l=1}^{n_y} [cE_l - 4\pi \tilde{B}_l(T_g)]_{k+1/2}^{n+1} [\omega_l(T_g)]_{k+1/2}^{n+1}. \quad (\text{A28})$$

A Newton-Raphson or other suitable iterative scheme is used to determine $(T_g)_{k+1/2}^{n+1}$ to within a specified tolerance. For a gray atmosphere use may be made of the fact that

$$\int_0^\infty j_\nu d\nu = \frac{4\pi}{c} \int_0^\infty B^\nu(T) d\nu = aT^4 \quad (\text{A29})$$

to define $\tilde{B}(T_g)$ in equation (28) as

$$\tilde{B}_l(T_g) = g_l(T_g) \frac{\sigma}{\pi} T_g^4, \quad (\text{A30})$$

where

$$g_l(T) \equiv \frac{\int_{v(l)}^{v(l+1)} B^\nu(T) d\nu}{\int_0^\infty B^\nu(T) d\nu} = \pi \int_{v(l)}^{v(l+1)} B^\nu(T) d\nu / \sigma T^4 \quad (\text{A31})$$

may be tabulated and stored in core for table lookup and interpolation rather than requiring calculation of the numerator in equation (A31) at each temperature iteration.

f) *Doppler Terms*

Terms which would ordinarily arise from frequency-derivative terms in the moment equations are treated in the limit $\Delta\nu_{\text{Doppler}} \ll \Delta\nu_{\text{bin}}$ by an ad hoc procedure of adding and/or subtracting energy from the appropriate energy groups, zone by zone, spatially. The values of E^ν determined by the tridiagonal scheme represent total energy in the particular frequency group, and the assumption is made that a mean value given by $(E^\nu/\Delta\nu)$ characterizes the energy distribution over frequency within the energy group. Then the Doppler "corrections" for zone k are taken to be $\delta\nu/\bar{\nu} \approx \delta\nu/\bar{\nu} = (v_{k-1/2} - v_{k+1/2})/c = \Delta v_k/c$, where $\bar{\nu}$ is the mean value of ν in the particular group considered. This implies an effective transfer of energy from one energy group to the next of order $\Delta E_D^i = \Delta t(\delta\nu_i/\Delta\nu_i)F_k^i = F_k^i \Delta t(\Delta v_k \bar{\nu}_i/c \Delta\nu_i)$. If the velocity increases outward, then zone $(k + \frac{1}{2})$ receives an additional amount ΔE_D^i in group $(i - 1)$ at the expense of group (i) , where increasing index i implies higher values of $\bar{\nu}$. In practice, for large values of $\Delta \log \nu$ in a given group, such corrections have only small effects on the energy distribution in the "ν-space."

g) *Choice of Interface Position*

The choice of mass coordinate (boundary R_{NF}) at which the EDS scheme is to be terminated and the TDEA scheme applied involves only the specification of an optical depth $\tau_{\text{NF}} \approx 3$ to 5. The run of τ^ν from $r = R_{jj}$ for the various frequency groups is determined at each R_k interior, and the interface boundary is established at the first (i.e., outermost) zone boundary R_k for which all energy groups have an optical depth of at least τ_{NF} . Because the expansion and temperature evolution of the model affects the run of the τ^ν , it is necessary to periodically relocate this boundary coordinate. In order to minimize the "noise" and error involved with such relocations, these changes in R_{NF} are limited to one zone, i.e., to R_{k-1} or R_{k+1} from R_k , and are further restricted to occurring no more frequently than some arbitrary number of time steps (10 seems to work reasonably in practice).

APPENDIX B

CENTERING CONSIDERATIONS, TIME STEPS, AND ACCURACY

Richtmyer and Morton (1967) give a complete analysis and discussion of the various difference schemes and their relative applicability, accuracy, and stability, especially in their chapter 8. Generally it may be concluded that accuracy is best with time-centered schemes, but backward-differenced schemes have the advantage of being most stable mathematically. It is important to note also that nonlinearities and particular boundary conditions may adversely affect either stability or accuracy.

The explicit hydrodynamic scheme requires, for stability, that the time step Δt be chosen so as not to violate the minimum of the various zones' Courant conditions; i.e., that $\Delta t \leq 0.8 \Delta R/c_s$, where c_s is the local sound speed, given by

$$c_s \approx (P_g/\rho)^{1/2}, \quad (B1)$$

and ΔR is the zone width $\Delta R = R_{k+1} - R_k$, and the numerical factor (0.8) is less than unity for an extra margin of safety (cf. Colgate and White 1966). In general, even in implicit schemes, accuracy places similar restrictions on choice of time step: the minimum of the various applicable physical time scales over all zones must not be exceeded by some factor usually determined by trial and usually less than unity. For example, the diffusion scheme picks the all-zone minima of the zone photon diffusion time [$\kappa\rho(\Delta R)^2/c$] and the zone Kelvin time [$E\Delta m/(L_{in} - L_{out})$]; it is found that the hydrodynamics and coupled energy transport have the desired accuracy if the all-zone minimum of the expansion time scale (R/v) is included. In addition, due to the possible presence of shocks and/or the large value of energy time derivatives, the changes over a time step of zone temperatures, densities, and fluxes are limited to 3%, 2%, and 5%, respectively. The transport scheme picks minima of Kelvin times and monitors absorption and emission times; the change in E^v is limited to roughly 3%, changes in F^v to 5%. These proportions have all been found to yield reasonable accuracy in practice.

Several tests have been run to determine the accuracy of these schemes. The hydrodynamic scheme is well documented (Christy 1964; Arnett 1966a, Colgate and White 1966); it gives the Sedov solution for strong shocks, and yields satisfactory accuracy for adiabatic Newtonian free-fall conditions. The diffusion scheme relaxes temperatures to the spherical Bessel function solution for a static, constant-temperature central source and satisfies conditions of adiabatic relaxation for a slow expansion. The transport scheme is more difficult to calibrate because of a notable lack of analytic tests to which calculations may be compared. Computational tests include requiring flux constancy (more correctly, luminosity constancy in the spherical case) at low optical depths in static cases, or favorable comparison of slab penetration calculations with, for instance, Monte Carlo calculations of the same case (cf. Campbell and Nelson 1964). It is also noteworthy that the scheme reproduces a Planck-like spectrum at large optical depths, and also at small depths in the case of gray opacities.

Several periodic checks are performed to keep track of energy conservation by the schemes as the calculation proceeds. The first is that of the total energy, given by equation (3) (§ III). Similar relations check the efficiency of the transport scheme. The emission absorption balance of individual zones is monitored by a relation of the form of equation (A28):

$$\rho\Delta_t[E_g + (P + Q)V] = \sum_l k_l c \left(E_l - \frac{4\pi}{c} B_l \right). \quad (B2)$$

When all time step criteria are adhered to, the average total energy error for 50 zones over 10,000 time steps is typically less than 2% of the initial total energy, a large part of which is involved in "starting" the shock wave as a high-velocity mass plate which acts as a cold piston at the center of the spherical envelope. Such an effect is illustrated in Arnett (1966b), and a discussion of the error is given in Fromm (1961). A more complete discussion of errors in the pseudoviscous shock method and the diffusion scheme may be found in Arnett (1966b), Christy (1964), and Richtmyer and Morton (1967), for example. For a discussion of errors due to the diffusion and transport equations, refer to Campbell and Nelson (1964) and Campbell (1965); their studies show clearly both the need for a transport calculation at low optical depths, and the good agreement of these transport methods with Monte Carlo transport calculations, even at early times.

As mentioned in the text, it is computationally desirable to limit the number of zones to which the transport approach is applied, yet accuracy considerations imply the need for a large optical depth treated in this way. In practice, the EDA scheme is applied to depths $\tau \geq 3$ to 5. The rationale for this choice is the identification of the diffusion process with a random walk of photons. This requires a large number of scattering events per photon over the distance of interest, i.e., a small mean-free path in comparison with characteristic fluid dimensions. The mean-square radial displacement in a random walk of N steps of constant mean free path λ is

$$\langle x^2 \rangle = \frac{2}{3}N\langle \lambda^2 \rangle = \frac{2}{3}N\langle (\kappa\rho)^{-2} \rangle.$$

If the root-mean-square displacement is identified with radial distance Δr_s to the surface $\tau = 0$, then

$$\begin{aligned} N &\approx \frac{3}{2}\langle x^2 \rangle \langle (\rho\kappa)^2 \rangle \\ &= \frac{3}{2}(\Delta R \rho \kappa)^2 \\ &\approx \frac{3}{2}\tau^2, \end{aligned}$$

and N is seen to increase as the square of optical depth τ . The error involved in the use of the diffusion approximation must decrease as τ^2 . Another way of viewing this limit is to notice that the probability for a photon to escape without scattering from depth τ is proportional to $e^{-\tau}$. This value must be sufficiently low as to limit the anisotropic

component of the intensity to values small in comparison with the isotropic component. In practice, the "errors" involved in picking $\tau_{\text{NF}} \lesssim 5$ do reflect this behavior, relative to the choice of $\tau_{\text{NF}} = 25$, say. The choice of $3 \leq \tau_{\text{NF}} \leq 5$ therefore results from a compromise between accuracy requirements and the need to minimize the number of TDEA zones.

It is worthwhile to point out that the choice of τ_{NF} affects the partition of energy into the various frequency bins at the scheme interface. Total energy is conserved, but the extent to which the problem is nongray and the sensitivity of the photon transport (in terms of departures from the diffusion approximation) near the outer boundary dictate a careful choice of τ_{NF} .

APPENDIX C

COMPUTATIONAL TREATMENT OF DENSITY INVERSIONS

The Rayleigh-Taylor instability may be expected to occur (in spherical symmetry) if, for two adjacent mass zones, $\rho_1 < \rho_2$ and $(v_1/R_1) > (v_2/R_2)$, where subscripts 1 and 2 refer to the inner and outer zones of the pair, respectively. The less dense, faster moving matter will penetrate the slower, denser material outside it, leading to mixing of two density phases in the region of the interface. Net momentum transport across a Lagrangian mass coordinate will result; blobs of matter of density ρ_1 will penetrate matter of density ρ_2 at a relative velocity $\Delta v \approx v_1 - v_2$, carrying moments $\rho_1 \Delta v$ per unit of mass penetrating this interface. Random (isotropic) turbulent motions may be expected to develop, to complete the mixing and account for the difference in bulk kinetic energy between the pre- and postmixing conditions.

This penetration and momentum transport must here be treated in a one-dimensional, spherically symmetric finite-difference scheme using Lagrangian mass coordinates. Consider two adjacent zones: the three boundary mass "plates" involved have velocities $v_{i-1} > v_i > v_{i+1}$ at positions $R_{i-1} < R_i < R_{i+1}$ and define two adjacent mass zones of density $\rho_{i-1/2}$ and $\rho_{i+1/2}$ having masses $\Delta m_{i-1/2}$ and $\Delta m_{i+1/2}$. The plate masses are given by $\delta m_i \equiv 0.5(\Delta m_{i-1/2} + \Delta m_{i+1/2})$. Net transport of internal (i.e., thermal) energy is neglected, based on the assumption that the material behind the shock front is, in general, nearly isothermal, and that the energy transport is radiation-dominated. At boundary R_i matter from zone $i - \frac{1}{2}$ will penetrate the fluid ahead of it in zone $i + \frac{1}{2}$. An explicit scheme, conserving momentum and transporting it across boundary R_i , is desired.

The matter at the interface experiences an acceleration in the comoving frame of order

$$a_i \approx v_i \Delta v_i \frac{\Delta \rho_i}{\rho_i} l^{-1}, \quad (C1)$$

where

$$\begin{aligned} \Delta v_i &= v_i - v_{i+1}, \\ \Delta \rho_i &= \rho_{i+1/2} - \rho_{i-1/2}, \end{aligned} \quad (C2)$$

and l is the characteristic length of penetration and/or mixing. For the difference scheme, $l \approx \Delta R_{i+1/2} \equiv R_{i+1} - R_i$, i.e., the length of interest is assumed to be the order of a zone size. The simplifying assumption is made that, at the interface, the average velocity of the penetrating mass which gives rise to the acceleration is v_i , and not some combination of v_i, v_{i-1} which might more accurately specify the mean velocity of all the mass in zone $i - \frac{1}{2}$.

Euler's equation is

$$\ddot{r}_i = -4\pi r_i^2 \frac{\partial(P + Q)}{\partial m} \Big|_i - g_i. \quad (C3)$$

The mass plate at R_i will experience a different acceleration due to the net "loss" of momentum from zone $i - \frac{1}{2}$ to zone $i + \frac{1}{2}$. This difference is expressed by

$$\delta m_i^{-1} p_i = -a_i = -\zeta v_i \Delta v_i \frac{\Delta \rho_i}{\rho_i} \Delta R_i^{-1}. \quad (C4)$$

To conserve momentum, plates must be considered in pairs, and equal and opposite moments added to these plates. It is simplest to consider the single pair of plates at R_i and R_{i+1} ; the momentum equation for plate $i + 1$ is also modified, and finally

$$\begin{aligned} \ddot{r}_i &= -4\pi r_i^2 \frac{\partial(P + Q)}{\partial m} \Big|_{i+1} - g_{i+1} - a_i, \\ \ddot{r}_{i+1} &= -4\pi r_{i+1}^2 \frac{\partial(P + Q)}{\partial m} \Big|_{i+1} - g_{i+1} + a_i \frac{\delta m_i}{\delta m_{i+1}}, \end{aligned} \quad (C5)$$

where the mass ratio in the second equation is necessary in the event of unequal plate masses, and the choice of signs has the effect of giving a rearward impulse to the Lagrangian plate i and a forward impulse to plate $i + 1$.

Momentum is conserved by relations (C5) but, in general, kinetic energy of the bulk flow is not. Physically it would be converted in part into turbulent kinetic energy. To determine the amount of bulk flow kinetic energy "lost" in this way, K_t , the quantities v_i^{n+1} and v_{i+1}^{n+1} are calculated from both relations (C5) and (C3) separately. The difference in total plate-pair kinetic energy implied by these two sets of velocities, ΔK_t , is attributed to turbulent energy in zone $i + \frac{1}{2}$. If small, it may be regarded as an error term in a suitable energy-conservation check. In general, it is necessary to describe $K_{t,i}^{n+1}$ by a relation of the form

$$K_{t,i}^{n+1} = K_{t,i}^n + \Delta K_{t,i}^{n+1/2} - \frac{K_{t,i}^{n+1/2}}{\tau_i^{n+1/2}} - Q_{t,i}^{n+1/2} \dot{V}_i^{n+1/2}. \quad (\text{C6})$$

The third term on the right represents a viscous dissipation (if $\tau_i^{n+1/2}$ is understood to be a characteristic e -fold time for the dissipation processes), and has been neglected for the purposes of these calculations. The last term on the right is the PdV work done by the turbulent pressure (in an ideal gas), where Q_t is taken in the isotropic case to be

$$Q_t = \frac{1}{3} \rho v_t \Delta v,$$

where v_t is obtained from

$$K_t = \frac{1}{2} \Delta m v_t^2$$

and represents an average turbulent velocity, assuming the turbulent energy K_t is spread uniformly over the zone mass Δm .

The presence of nonnegligible turbulent pressure must in turn be included in both momentum and energy transport equations, so equation (C3) becomes

$$\ddot{r}_i = -4\pi r_i^2 \frac{\partial(P + Q + Q_t)}{\partial m} \Big|_i - g_i$$

and equations (C5) are similarly modified. The energy equation is then

$$\dot{E} + (P + Q + Q_t) \dot{V} = -\frac{\partial L}{\partial m} + \frac{K_t}{\tau_t},$$

where the last term on the right is necessary to represent the viscous dissipation of K_t as a thermal source term, but has been neglected in the present calculations.

APPENDIX D

COLOR MAGNITUDES

Arp (1961a) gives the following relation for the absolute monochromatic magnitude of a blackbody radiator (radius R) at temperature T :

$$M_\lambda = C_\lambda - 5 \log(R/R_\odot) + \frac{1.561}{\lambda T} + X(T, \lambda), \quad (\text{D1})$$

where λ is specified in cm. The constant C_λ depends in general upon the color system used and individual instrument response in a band about some effective wavelength for the band. The function $X(\lambda, T)$ is (Aller 1963)

$$X(\lambda, T) = 2.5 \log(1 - e^{-hc/\lambda kT}). \quad (\text{D2})$$

We employ the following standard effective UBV wavelengths (centroid of area under response curves [Arp 1961a]) given in angstroms:

$$\begin{aligned} \lambda_U &= 3590, \\ \lambda_B &= 4425, \\ \lambda_V &= 5500. \end{aligned} \quad (\text{D3})$$

If, following Arp, we apply the resulting set of relations (D1) to the Sun, we find (for $M_{V\odot} = 4.84$ and $T_\odot \approx 5784$ K)

$$C_V = -0.055. \quad (\text{D4})$$

Application of equation (D1) allows the following color relations to be derived, assuming (Arp 1961a) that $U - B = -0.26$, $B - V = 0.61$ for a $T = 6000$ K blackbody:

$$B - V \approx -0.548 + \frac{6895}{T} + X_B(T) - X_V(T), \quad (\text{D5})$$

$$U - B \approx -1.63 + \frac{8205}{T} + X_U(T) - X_B(T), \quad (\text{D6})$$

where $X_i(T) \equiv X(\lambda_i, T)$. The implied values of C_U and C_B are

$$\begin{aligned} C_U &= -2.23, \\ C_B &= -0.603, \end{aligned} \quad (\text{D7})$$

which, together with equations (D1) and (D4) yield

$$M_U \approx -2.234 + \frac{4.348}{T_4} + X_U(T) - 5 \log(R/R_\odot), \quad (\text{D8})$$

$$M_B \approx -0.603 + \frac{3.528}{T_4} + X_B(T) - 5 \log(R/R_\odot), \quad (\text{D9})$$

$$M_V \approx -0.055 + \frac{2.838}{T_4} + X_V(T) - 5 \log(R/R_\odot), \quad (\text{D10})$$

where $T_4 \equiv T/10^4$ K. This procedure does not include effects of departures from strict blackbody radiance (especially line effects) which are certainly important in the postpeak epoch of the supernova event. The approximation of a Planck continuum is probably reasonable near peak light and for short times thereafter, however (Kirshner *et al.* 1973), so it is nonetheless useful to examine the accuracy of the relations given above. Different calibrations for relationships of this type may be necessary to account for variations in the actual color system employed and to account for the spectral character of individual supernovae. For example, Kirshner and Kwan (1974) employ the following relations for SN 1969I in NGC 1058 and SN 1970g in M101, respectively,

$$(B - V)_{1969I} \approx -0.30 + \frac{6290}{T}, \quad (\text{D11})$$

$$(B - V)_{1970g} \approx -0.73 + \frac{8264}{T}, \quad (\text{D12})$$

and give an excellent fit to the tabulated blackbody values of Matthews and Sandage (1963), equivalent to

$$(B - V)_{\text{MS}} = -0.44 + \frac{6290}{T}. \quad (\text{D13})$$

Table 18 provides a comparison of the relative accuracies of the blackbody relations with the numerically calculated values reported by Arp (1961a) and by Matthews and Sandage (1963). These tabulated values are listed in the columns labeled $(B - V)_A^T$ and $(B - V)_{\text{MS}}^T$, respectively. Values arising from the application of relation (D5), after Arp, and relation (D13), after the Kirshner and Kwan fit to the tabulated values of Matthews and Sandage, are given in the columns $(B - V)_A$ and $(B - V)_{\text{KK}}$, respectively. Relations (D11) and (D12) provide the values in the columns labeled $(B - V)_{1969I}$ and $(B - V)_{1970g}$. The remaining column $(B - V)_A^*$, gives those values which result from neglecting the correction $[X_B(T) - X_V(T)]$ in relation (D5). The agreement between the tabulated values and the three blackbody equations (i.e., not the recalibrated supernova relations) is good at low temperatures ($T \lesssim 10,000$ K) but worsens at higher temperatures. The correction $X_B - X_V$ is of decreasing importance as temperatures decline, but cannot be neglected for $T \approx 6000$ – $10,000$ K or so if relation (D5) is to be applied.

A reasonable fit to the tabulated Matthews and Sandage blackbody $(U - B)$ values is

$$(U - B)_{\text{FA}} \approx -1.39 + \frac{6897}{T}. \quad (\text{D14})$$

Table 19 provides a comparison of the values predicted by this equation with the tabulated values of Arp, $(U - B)_A^T$, and those of Matthews and Sandage, $(U - B)_{\text{MS}}^T$. Also shown are the values which result from application of relations (D6) with and without the $(X_U - X_B)$ correction term, $(U - B)_A$ and $(U - B)_A^*$, respectively. We obtain good agreement between the tabulated values and $(U - B)_{\text{FA}}$ at intermediate temperatures ($4000 \lesssim T \lesssim 25,000$ K),

TABLE 18
COMPARISON OF $(B - V)$ VALUES FOR VARIOUS COLOR EQUATIONS

T (K)	$(B - V)_A^T$	$(B - V)_{MS}^T$	$(B - V)_{MS}$	$(B - V)_A$	$(B - V)_A^*$	$(B - V)_{19691}$	$(B - V)_{1970g}$
∞	-0.46	-0.44	-0.44	-0.33	-0.55	-0.30	-0.73
25,000	-0.23	-0.21	-0.188	-0.048	-0.274	-0.048	-0.399
20,000	-0.17	-0.15	-0.126	-0.019	-0.205	+0.015	-0.317
12,000	+0.04	+0.05	+0.084	+0.116	+0.025	+0.224	-0.041
8000	+0.34	+0.35	+0.346	+0.347	+0.312	+0.486	+0.303
6000	+0.61	+0.63	+0.608	+0.612	+0.599	+0.748	+0.647
5000	+0.78	+0.79	+0.818	+0.834	+0.829	+0.958	+0.923
4000	+1.12	+1.13	+1.133	+1.179	+1.174	+1.273	+1.336
3300	+1.44	+1.44	+1.466	+1.540	+1.539	+1.606	+1.774
3000	+1.66	+1.67	+1.657	+1.748	+1.748	+1.800	+2.025

and a relatively poorer agreement at $T = \infty$ and $T < 4000$ K. However, since T_e for the peak and early postpeak epoch lies predominantly in the range of the intermediate temperatures, relation (D14) will suffice for the purposes of the models presented in this paper. No attempt has been made to apply corrections for individual supernova character. As the examples of SN 19691 and SN 1970g show, "typical" SN II corrections may be in either direction from blackbody values.

The fitted forms of $U - B$, $B - V$ do not admit of a consistent specification of individual color-magnitude functions M_λ of the form of relation (D1); in light of the approximate agreement of $(U - B)_{FA}$ and $(U - B)_A$, and $(B - V)_{MS}$ and $(B - V)_A$, it will be sufficient for our purposes to employ relations (D8)–(D10) to elicit the qualitative features of model light curves in terms of $T_e(t)$ and $R_{ph}(t)$. In particular, relation (D9) has been employed to provide $M_B(t)$ for models A and B.

Figures 26 and 27 show $U - B$ and $B - V$, respectively, as functions of time for the models of this paper, with comparison curves for several SN I and SN II. In principle the observed shape of the prepeak to postpeak transition in either color curve could differentiate between the relatively abrupt transitions which result for compact models (e.g., A and D) and the more gradual and smooth transitions resulting for extended models (C, E, F). There is the additional suggestion of a slope change in both color curves during the prepeak stage. This is most apparent in the case of model C (at $t_6 \approx 0.6$), and can be interpreted as the arrival of the diffusion wave at the photospheric surface in the circumstellar shell material (see text). For all the (blackbody) model color curves shown, the portpeak epoch is characterized by a continuous reddening, with $d/dt[(U - B) \text{ or } (B - V)] \leq 0$ until a time t_+ which is not well correlated with any simple physical transition in the models, but occurs for $T_e \lesssim 6000\text{--}7000$ K. After t_+ (most apparent in models A and F at $t_6 \gtrsim 4$), the color curves apparently have $d/dt[(U - B), (B - V)] \geq 0$. This effect may not be real, depending as it does upon the details of opacity relations used in the calculations and the application of the diffusion equation at later model times. It is likely that any such effect, if real, would be overshadowed by the color effects of the dominant recombination lines as the photosphere receded significantly in mass. Such line contributions are almost certainly responsible for the abrupt cessation of postpeak reddening in the $(U - B)$, $(B - V)$ colors of observed supernovae [e.g., the $(U - B)$ curves for the SN II in NGC 7331 and SN 1972 in NGC 5253 shown in Fig. 27]. It is perhaps worth pointing out that the observed $(B - V)$ colors of the SN II in NGC 7331 suggest a peak epoch shape characteristic of extended models, even though the $(U - B)$ curve shows no such behavior. It would be useful in this context to have definitive early prepeak and peak color information and relative magnitudes. A convincing theoretical interpretation of observed color curves will require the calculation of nongray, nondiffusive hydrodynamic models for light curves which properly include effects of the dominant (e.g., hydrogen) continua as well as the principal line contributions to, for instance, the UBV bands.

TABLE 19
COMPARISON OF $(U - B)$ VALUES FOR VARIOUS COLOR EQUATIONS

T (K)	$(U - B)_A^T$	$(U - B)_{MS}^T$	$(U - B)_{FA}$	$(U - B)_A$	$(U - B)_A^*$
∞	-1.33	-1.28	-1.39	-1.39	-1.63
25,000	-1.17	-1.13	-1.114	-1.302	-1.302
20,000	-1.09	-1.06	-1.045	-1.220	-1.220
12,000	-0.84	-0.83	-0.815	-0.946	-0.946
8000	-0.52	-0.53	-0.528	-0.605	-0.604
6000	-0.22	-0.26	-0.241	-0.263	-0.263
5000	-0.05	-0.10	-0.011	+0.011	+0.011
4000	+0.37	+0.36	+0.334	+0.421	+0.421
3300	+0.23	+0.78	+0.700	+0.856	+0.856
3000	+1.14	+1.07	+0.909	+1.105	+1.105

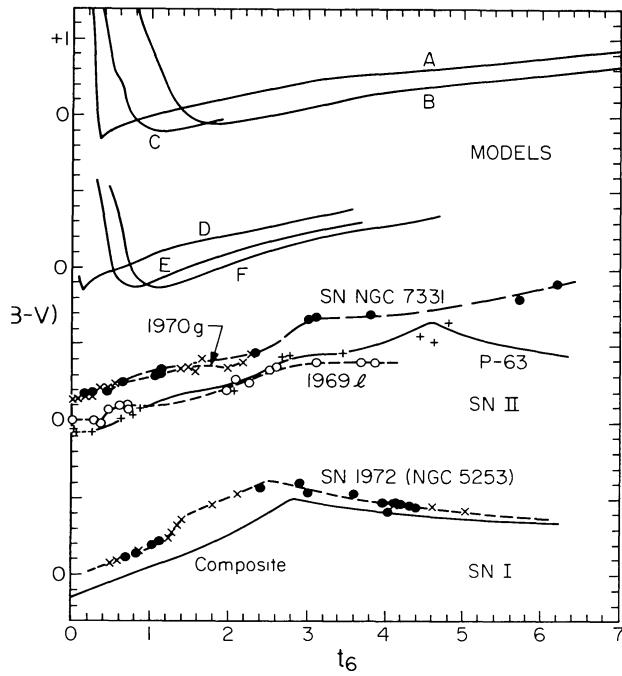


FIG. 26

FIG. 26.—($B - V$) as a function of time for the models and selected supernovae. The curve labeled 1969l is for the supernova in NGC 1058; photometric data taken from Kirshner and Kwan (1974). Data for SN 1970g in M101 is from Winzer (1974), that for the SN in NGC 7331 from Arp (1961b). The curve labeled P-63 refers to the supernova labeled number 63 in Pskovskii (1968). The composite curve for SN I is from this same source. Data for SN 1972 in NGC 5253 are from Lee, Wamsteker, and Wisniewski (1972). In each observational curve, the data points are as reported by the various authors, while the connecting lines are only meant to be suggestive.

FIG. 27.—($U - B$) as a function of time for the models and selected supernovae. Data sources for individual supernovae of Type II are the same as for Fig. 26. Two reasonable composite curves (labeled X and Y) were reported by Pskovskii (1968) for SN I and are shown. ($U - B$) data for SN 1972 in NGC 5253 are taken from Ardeberg and de Groot (1973).

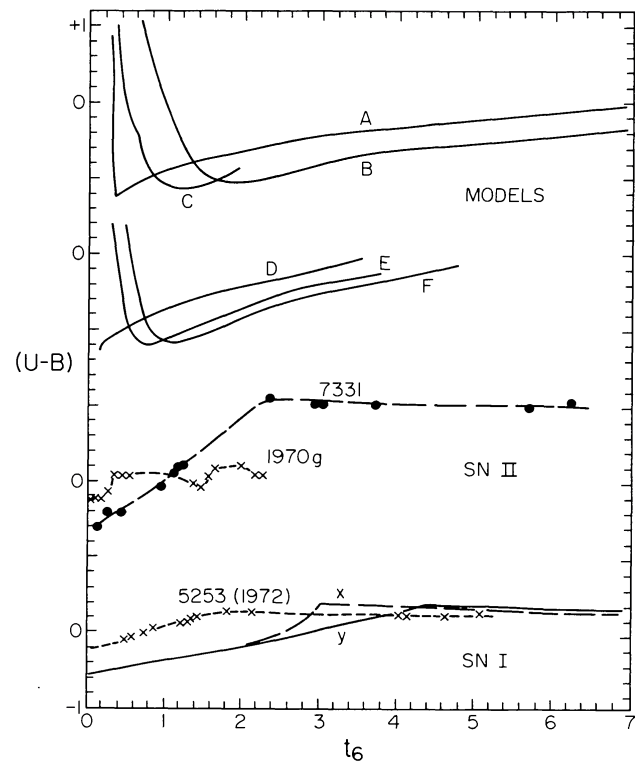


FIG. 27

- Aller, L. H. 1963, *Astrophysics: The Atmospheres of the Sun and Stars* (2d ed.; New York: Ronald).
- Ardeberg, A., and de Groot, M. 1973, *Astr. Ap.*, **28**, 295.
- Arnett, W. D. 1966a, *Canadian J. Phys.*, **44**, 2553.
- . 1966b, Ph.D. thesis, Yale University.
- . 1975, *Ap. J.*, **195**, 727.
- Arnett, W. D., and Falk, S. W. 1976, *Ap. J.*, **210**, 733.
- Arp, H. 1961a, *Ap. J.*, **133**, 874.
- . 1961b, *Ap. J.*, **133**, 883.
- Auer, L. 1967, *Ap. J. (Letters)*, **150**, L53.
- Bodenheimer, P., and Ostriker, J. P. 1974, *Ap. J.*, **191**, 465.
- Böhm, K.-H. 1973, in *IAU Symposium No. 51, Extended Atmospheres and Circumstellar Matter in Spectroscopic Binary Systems*, ed. A. H. Batten (Dordrecht: Reidel), p. 148.
- Campbell, P. M. 1965, *Univ. California Lawrence Livermore Radiation Lab. Rept.* UCRL-12411.
- Campbell, P. M., and Nelson, R. G. 1964, *Univ. California Lawrence Livermore Radiation Lab. Rept.* UCRL-7838.
- Castor, J. I. 1972, *Ap. J.*, **178**, 779.
- Chapman, R. D. 1966, *Ap. J.*, **143**, 61.
- Chevalier, R. 1976, *Ap. J.*, **207**, 872.
- Christy, R. F. 1964, *Rev. Mod. Phys.*, **36**, 555.
- Ciatti, F., Rosino, L., and Bertola, F. 1971, *Mem. Soc. Astr. Italiana*, **42**, 163.
- Clayton, D. D. 1968, *Principles of Stellar Evolution and Nucleosynthesis* (New York: McGraw-Hill).
- Colgate, S. A., and McKee, C. 1969, *Ap. J.*, **157**, 623.
- Colgate, S. A., and White, R. N. 1966, *Ap. J.*, **143**, 626.

REFERENCES

- Cox, A. N., and Stewart, J. N. 1965, *Ap. J. Suppl.* (No. 94), **11**, 22.
- Cox, J. P., and Giuli, R. T. 1968, *Principles of Stellar Structure*, vol. 1, *Physical Principles* (New York: Gordon and Breach).
- Falk, S. W. 1974, Ph.D. thesis, University of Texas at Austin.
- Falk, S. W., and Arnett, W. D. 1973, *Ap. J. (Letters)*, **180**, L65.
- Falk, S. W., and Scalo, J. M. 1975, *Ap. J.*, **202**, 690.
- Frank-Kamenetskii, D. A. 1962, *Physical Processes in Stellar Interniors* (Jerusalem: Israel Program for Scientific Translations).
- Fromm, J. E. 1961, "Lagrangian Difference Approximations for Fluid Dynamics," Univ. California Los Alamos Scientific Lab. Rept. LA-2535.
- Gehrz, R. D., and Woolf, N. J. 1971, *Ap. J.*, **165**, 285.
- Grasberg, E. K., Imshennik, V. S., and Nadyozhin, D. K. 1971, *Ap. Space Sci.*, **10**, 28.
- Gunn, J. E., and Ostriker, J. P. 1970, *Ap. J.*, **160**, 979.
- Hummer, D. G., and Rybicki, G. B. 1970, *M.N.R.A.S.*, **152**, 1.
- Imshennik, V. A., and Morozov, Y. I. 1969, *Astr. Zh.*, **46**, 800.
- Karp, A. H., Lasher, G., Chan, K. L., and Salpeter, E. E. 1976, preprint.
- Kirshner, R. P., Arp, H. C., and Dunlap, J. R. 1976, *Ap. J.*, **207**, 44.
- Kirshner, R. P., and Kwan, J. 1974, *Ap. J.*, **193**, 27.
- . 1975, *Ap. J.*, **197**, 415.
- Kirshner, R. P., Oke, J. B., Penston, M., and Searle, L. 1973, *Ap. J.*, **185**, 303.
- Lasher, G. 1975, *Ap. J.*, **201**, 194.

- Lee, T. A., Wamsteker, W., and Wisniewski, W. Z. 1972, *Ap. J. (Letters)*, **177**, L59.
- Low, F. J., Johnson, H. L., Kleinman, D. E., Latham, A. S., and Geisel, S. L. 1970, *Ap. J.*, **160**, 531.
- Matthews, T. A., and Sandage, A. R. 1963, *Ap. J.*, **138**, 30.
- Mihalas, D. 1970, *Stellar Atmospheres* (San Francisco: W. H. Freeman).
- Morrison, P., and Sartori, L. 1969a, *Ap. J.*, **158**, 541.
—. 1969b, in *Supernova and Their Remnants*, ed. P. Brancazio and A. G. W. Cameron (New York: Gordon and Breach), chap. 10.
- Mustel, E. 1976, *Soviet Astr.—AJ*, **19**, 685.
- Ostriker, J. P., and Gunn, J. E. 1969, *Ap. J.*, **157**, 1395.
—. 1971, *Ap. J. (Letters)*, **164**, L95.
- Paczyński, B. 1971, unpublished envelope integrations.
- Pskovskii, Y. P. 1968, *Soviet Astr.—AJ*, **11**, 570.
- Richtmyer, R. D., and Morton, K. W. 1967, *Difference Methods for Initial Value Problems* (2d ed.; New York: Interscience).
- Rose, W. K. 1973, *Astrophysics* (New York: Holt, Rinehart, and Winston).
- Sampson, D. H. 1965, *Radiative Contributions to Energy and Momentum Transfer in Gas* (New York: Interscience Publishers).
- Schmid-Burgk, J. 1973, *Ap. J.*, **181**, 865.
- Talbot, R. J., Jr. 1968, Ph.D. thesis, M.I.T.
- Tammann, G. 1974, in *Supernovae and Supernovae Remnants*, ed. C. B. Cosmovici (Boston: Reidel), part IV, p. 155.
- Trimble, V. 1968, *A.J.*, **73**, 535.
- Ulrich, R., and Scalo, J. M. 1975, unpublished envelope integrations.
- Wilson, W. J., Barrett, A. H., and Moran, J. M. 1970, *Ap. J.*, **160**, 545.
- Winzer, J. E. 1974, *J.R.A.S. Canada*, **68**, 36.
- Woltjer, L. 1972, *Ann. Rev. Astr. Ap.*, **10**, 129.

W. DAVID ARNETT and SYDNEY W. FALK: Enrico Fermi Institute, University of Chicago, Chicago, IL 60637